

**An investigation into plasma
surface interactions, focussing on
surface produced, and surface
assisted, negative ion generation**

James Timothy Ellis

Doctor of Philosophy

University of York

Physics

March 2020

Abstract

The study of negative ions in low temperature, low pressure, radio-frequency plasmas has become increasingly important for a number of applications, including neutral beam injection (NBI). Additionally, as nuclear fusion reactors increase in size, more stringent requirements are placed upon NBIs. Unfortunately, the use of positive ions is infeasible at these higher energies, as their neutralisation efficiency rapidly decreases at higher energies/nucleon; this is not the case for negative ions. However, generating negative ions in sufficient quantities is challenging. Currently, the only feasible method is through using caesiated metallic surfaces. Whilst caesiated metallic surfaces are an acceptable replacement in the short term, an alternative is necessary, due to the inherent problems with using caesium.

This work has measured H^- ion densities through using laser photodetachment above multiple metallic surfaces; these have been shown to have an influence on the volume produced H^- ion densities. It was discovered that tungsten and stainless steel surfaces result in a higher H^- ion density than copper, aluminium, and molybdenum surfaces. This was explained by considering that the recombination of atomic hydrogen at the surface could produce vibrationally excited molecular hydrogen, that in turn undergoes dissociative attachment to form H^- ions. Two-photon absorption laser induced fluorescence and phase resolved optical emission spectroscopy were used to investigate this hypothesis; the results of which are presented within this work.

Finally, for the first time, nitrogen doped diamond samples and a nanoporous $12CaO \cdot 7Al_2O_3$ (C12A7) electride were investigated for their ability to produce H^- ions. Consequently, nitrogen doping was observed to have an influence on the H^- ion yield; this was not observed with previously investigated doped diamond samples. Comparisons to other non-caesiated surfaces therefore suggest that both materials are worthy of further study for their ability to produce a large quantity of negative ions.

Contents

Abstract	2
Contents	3
List of Tables	7
List of Figures	8
Acknowledgements	11
Declaration	13
1 Motivation and Chapter Outlines	14
1.1 Motivation	14
1.2 Chapter Outlines	15
2 Background Theory	17
2.1 Defining a Plasma	17
2.2 Quasi-neutrality	18
2.3 Debye Length	18
2.4 Non-equilibrium Nature	18
2.5 Bounding a Plasma	19
2.6 Radio-Frequency Plasmas	20
2.7 Nuclear Fusion	21
2.7.1 Benefits of Nuclear Fusion	22
2.7.2 External Heating	24
2.7.3 Neutral Beam Injection	24

<i>CONTENTS</i>	4
2.8 Volume Production of Negative Hydrogen Ions H^-	26
2.8.1 Creation of Vibrationally Excited Molecules	27
2.8.2 Destruction of Vibrationally Excited Molecules	28
2.8.3 Destruction of H^- ions	30
2.9 Plasma surface interactions	31
2.9.1 Surface Assisted Excitation	31
2.9.2 Atomic surface interactions	32
2.9.3 Relaxation of Vibrationally Excited Species via Surface Collisions	32
2.9.4 Direct Surface Production of H^- Ions	33
3 Methodology	36
3.1 Gaseous Electronics Conference Reference Cell	36
3.2 Langmuir Probes	38
3.2.1 Regions of an IV Curve	38
3.2.2 Introduction to the Mathematical Formalisation	40
3.3 Photodetachment	41
3.3.1 Background Theory	41
3.3.2 Experimental Procedure	42
3.4 Phase Resolved Optical Emission Spectroscopy	44
3.4.1 Background Theory	44
3.4.2 Experimental Procedure	45
3.5 Collaboration with the Physics of Ionic and Molecular Interactions (PIIM) group in Marseille	46
3.5.1 Description of the Reactor	46
3.5.2 Electron Cyclotron Resonance Plasma	46
3.5.3 Sample Holder	47
3.5.4 EQP Mass Spectrometry	48
3.5.5 Negative Ion Extraction	49
3.5.6 Experimental Procedure	50
3.6 Two Photon Absorption Laser Induced Fluorescence – TALIF	51
3.6.1 Introduction to TALIF	51
3.6.2 Excitation	52
3.6.3 Loss Mechanisms	54

<i>CONTENTS</i>	5
3.6.4	Detection 56
3.6.5	Calibration 57
3.6.6	Experimental Procedure 59
3.6.7	Detection Scheme 61
3.6.8	Effective Lifetime Measurements 62
3.6.9	Total Fluorescence Signal 63
3.6.10	Error Analysis 64
3.7	Confocal Microscopy 65
4	H⁻ Density measurements in the GEC reference cell 67
4.1	Prelude 67
4.2	Experimental Benchmarks 69
4.3	Stainless Steel 304 Surface 72
4.4	Copper Surface 75
4.5	Comparison Between Surfaces 79
4.6	Discussion 83
4.6.1	Comparison to Literature 83
4.6.2	Surface Loss Rates 83
4.6.3	Thermal Properties 84
4.6.4	Interstitial Hydrogen Trapping 84
4.7	Chapter Summary 84
5	H⁻ density measurements on novel surfaces 86
5.1	Prelude 86
5.1.1	Literature Review 87
5.2	Nitrogen Doped Diamond 89
5.3	Electride Results 95
5.4	Discussion 100
5.4.1	Nitrogen Doped Diamond Sample Creation 100
5.4.2	Conductivity of nitrogen doped diamond 101
5.4.3	Comparison of negative ion yields to other surfaces 101
5.5	Chapter Summary 103

<i>CONTENTS</i>	6
6 H Density Measurements in the GEC Reference Cell	104
6.1 Prelude	104
6.2 Power and Pressure Variations	105
6.3 Surface Variations	108
6.4 Discussion	109
6.4.1 Comparison to Literature	109
6.4.2 Surface Loss Coefficients	110
6.5 Chapter Summary	110
7 Conclusions	112
8 Appendix A – The E to H-mode Transition	116
8.1 Results	116
8.2 Discussion	121
8.2.1 Dependency of the Surface on the H-mode Transition	121
8.3 Appendix Summary	122
List of References	123

List of Tables

2.1	Power density for various energy sources	23
-----	--	----

List of Figures

2.1	Schematic of the sheath and presheath	20
2.2	Power density graph	23
2.3	A schematic of a neutral beam injector	25
2.4	Positive and negative ion neutralisation efficiency	26
2.5	Comparison of V-T and V-t cross-sections	29
2.6	Mechanisms of atomic recombination at a surface	33
3.1	Schematic of the GEC reference cell	37
3.2	An example IV curve	39
3.3	Cross-section for the photodetachment of electrons from H^-	43
3.4	A schematic representation of the PHISIS reactor	47
3.5	A schematic representation of the EQP mass spectrometer. Labelled are the internal ioniser, energy analyser, Quadrupole mass filter, and detector.	49
3.6	Schematic of the potential profile. Copyright (2018) The Japan Society of Applied Physics [1]	50
3.7	Three level energy diagram	54
3.8	Excitation scheme for hydrogen TALIF	58
3.9	Annotated beam line for the TALIF measurements	60
3.10	Saturation curve for krypton	61
3.11	Example of the camera acquisition for TALIF	62
3.12	Exponential fit example for the effective lifetime measurements	63
3.13	Gaussian fit example for the spectral and time integrated TALIF signal mea- surements	64
4.1	H^- ion density as a function of applied voltage	69

4.2	H ⁻ ion density as a function of laser energy	70
4.3	H ⁻ ion density as a function of time within the pulse	71
4.4	Repeating the H ⁻ ion densities measured to calculate the standard deviation	72
4.5	Electron density for the steel sample at three different pressures	73
4.6	H ⁻ ion fractions for the steel sample at three different pressures	74
4.7	H ⁻ ion densities for the steel sample at three different pressures	75
4.8	H ⁻ fraction for the copper sample at three different pressures	76
4.9	H ⁻ ion densities for the steel sample at three different pressures	76
4.10	Results from PROES for the steel and copper samples	78
4.11	H ⁻ ion densities for the tungsten sample at three different pressures	79
4.12	H ⁻ ion densities for the steel and tungsten samples at three different pressures	80
4.13	H ⁻ ion densities for the copper and aluminum samples at three different pressures	82
4.14	H ⁻ ion densities for five different samples at 25 Pa	82
5.1	Negative ion yield as a function of time	89
5.2	Negative ion energy distribution functions for 100 ppm NDD at different temperatures	90
5.3	Negative ion yield as a function of temperature for the 100 ppm NDD sample	91
5.4	Negative ion yield as a function of the applied bias for the 100 ppm NDD sample	92
5.5	Recovery of the negative ion yield post surface damage	93
5.6	Negative ion yield as a function of temperature for the 50 and 100 ppm NDD samples	94
5.7	Negative ion yield as a function of temperature for different levels of nitrogen doping	95
5.8	Confocal microscopy images for the different nitrogen doped diamond samples	95
5.9	Comparison of surface bias on the negative ion energy distribution function for the electrified sample. Copyright (2018) The Japan Society of Applied Physics [1]	96
5.10	Negative ion energy distribution function for the molybdenum sample. Copyright (2018) The Japan Society of Applied Physics [1]	97
5.11	Comparison of negative ion energy distribution between a hydrogen and argon plasma for the electrified sample. Copyright (2018) The Japan Society of Applied Physics [1]	99

5.12	Results of baking out adsorbed hydrogen from the electride sample. Copyright (2018) The Japan Society of Applied Physics [1]	100
6.1	Atomic hydrogen density as a function of power for the copper sample, at a pressure of 25 Pa.	106
6.2	Atomic hydrogen density as a function of power for the copper sample, at three pressures: 20, 25, and 30 Pa.	107
6.3	Atomic hydrogen density as a function of power, for the steel sample, at three pressures: 20, 25, and 30 Pa.	108
6.4	Atomic hydrogen density as a function of power for five different surfaces at 25 Pa	109
8.1	The effective lifetime as a function of power for the tungsten surface, at a pressure of 25 Pa	117
8.2	Atomic hydrogen density as a function of power for the tungsten surface, at a pressure of 25 Pa	118
8.3	Low power E-mode excitation structure as measured by PROES	118
8.4	High power E-mode excitation structure as measured by PROES	119
8.5	H-mode excitation structure as measured by PROES	119
8.6	Atomic hydrogen density as a function of power for the tungsten surface, at a pressure of 30 Pa	120
8.7	Atomic hydrogen density as a function of power for the tungsten surface, at a pressure of 15 Pa	121

Acknowledgments

Firstly, I must give thanks to my supervisors Prof. Timo Gans and Prof. Deborah O'Connell for the guidance, encouragement, and patience they have given to me throughout my PhD. Furthermore, for all the help they have given me prior to the PhD, through summer and Christmas projects, and my MPhys dissertation. Hopefully, I now speak at a more acceptable pace! Secondly, my heartfelt thanks goes to Dr. Erik Wagenaars whose wonderfully accommodating nature led to many fruitful discussions. Beyond the PhD work, I couldn't imagine a better line manager for the administrative work; the patience you showed me whilst I got to grips with the role will always be remembered. Finally, to Dr. James Dedrick, whose positive mental attitude never dropped at any stage and who was always happy for a 5 minute conversation, especially if they ended up taking an hour...

Now, the quick fire round! Peter Hill, Nichola Egan, Scott Doyle, Isabella Gapp, may all your rolls be natural 20s. Thank you for being amazing friends throughout this entire experience, and I hope our D&D group continues long into the future! To Dr. Kari Niemi and Richard Armitage, none of this would have been possible without expertise. For all the administrative staff, Ruth Lowman, Kathryn Harvey, Jenni Priestly, Hillary Marshall, and Donna Cook, I mean it when I say our institute would crumble without all of you, thank you! To Damon Farely, Joshua Boothroyd, Martin Blake, Helen Davies, Joe Branson, Michael Mo, David Meehan, Andy West, Jerome Bredin, Andrew Gibson, Sandra Schroeter, Sarah Wilson, Dave Shaw, and all the other members of the YPI thank you all for making our group the welcoming place it has been throughout all these years. Finally, a huge thank you for all the wonderfully diverse discussions with Dr. Istvan Cziegler.

To the entire research group at PIIM, and perhaps most importantly Prof. Gilles Cartry. Your accommodating nature, easy friendship, and incredible technical assistance has been

appreciated more than I could say. I hope we get to work alongside each other again in the future, thank you. To the amazing group at the INP Greifswald led by Dr. Jean-Pierre Van Helden, working alongside all of you was an amazing experience, so much so that I'm coming back!

To my brother, you have always been an inspiration to me, the dedication you put into your work is beyond compare. To my Dad, *Good timber does not grow with ease...*, you will be missed more than I think you knew. To rest of my Ellis and Rodger family, who are too numerous to name, thank you all. To my Mum, the woman who always tried to do the impossible for me, you have made me the man I am today, for better or worse! For Hannah, the love, encouragement, and emotional support you have given me throughout my PhD has been beyond compare. Words cannot express how grateful I am, however, I'll spend my life trying to show you.

Declaration

This thesis has not previously been accepted for any degree and is not being concurrently submitted in candidature for any degree other than Doctor of Philosophy of the University of York. This thesis is the result of my own investigations, except where otherwise stated. All other sources are acknowledged by explicit references.

Chapter 4 contains data collected by another PhD student, J. Branson. However, their contribution is explicitly stated within the chapter itself. Chapter 5 was the result of a collaboration with Gilles Cartry at the Physics of Ionic and Molecular Interactions group at Aix-Marseille University, France. The data presented within Chapter 5, Section 5.3 *Electride Results*, has been previously published by Sasao *et. al.* [1]. The conclusions of Chapter 5, Section 5.2 *Nitrogen Doped Diamond* have been published as a result of a follow-up research visit by my collaborator G. Smith [2]. The data and conclusions of Chapters 4 and 6 have been combined into a paper that has been published by Ellis *et. al.* [3].

Chapter 1

Motivation and Chapter Outlines

1.1 Motivation

Plasma physics has not only shaped the course of human history, from the discovery of fire to the invention of the microchip, throughout its existence, but also the course of the universe. It is estimated that as much as 99.9 % of the observable universe is made of plasma. However, the variation in the types of plasma throughout the universe is as varied as the applications which have arisen from their study. With applications ranging from the sterilisation of surfaces, for both food technology and medical environments, to the growing of diamond. Plasmas have been used to create technologies that instil fear, such as the fusion bomb, but also to mitigate their usage, for example, over-the-horizon radar detection. Importantly, they have also allowed innovations that foster hope, from cancer research to fusion energy. Applications of plasma physics have defined the technologies that underpin the modern era, and through further study will continue to improve countless lives for generations to come.

Our sun, Sol, has been the inspiration for millions and is the easiest observable example of a plasma. It has inspired countless technologies, in particular, nuclear fusion as a source of energy. The necessity for alternative high power density energy sources has become increasingly apparent over the last few decades. Renewable energy sources can, and should, make up part of our future energy mix, however, the huge swathes of land required in order to provide the required power is infeasible for most countries.

Unfortunately, nuclear fusion reactors require substantial external heating before fusion events can begin to take place. This external heating can be supplied in a number of ways, however, the most prevalent of these is currently neutral beam injection. As fusion reactors

increase in size, there is a necessity to use negative ions in order to generate highly energy neutral beams. Currently, these negative ions are generated within a low temperature, low pressure plasma via interactions with a caesiated metallic surface. Whilst this is suitable for current generation devices, caesium is a highly undesirable material to use for commercial fusion reactors and an alternative source of negative ions needs to be found. Currently, no alternatives to caesium exist, and the role of multiple chemical mechanisms on the negative hydrogen ion density is still not fully understood.

Ultimately, the aim of this work is to answer the following question: *How does the negative hydrogen ion density depend on the surface material?* In an attempt to answer this question, different mechanisms for the generation of negative ions will be investigated. Laser photodetachment is used to measure the dependency of the volume produced negative ions on the surface. Mass spectrometry is used to investigate direct surface production of negative ions for possible alternatives to caesium. Finally, two-photon absorption laser induced fluorescence and phase resolved optical emission spectroscopy are used to investigate the role of atomic hydrogen, and the plasma dynamics respectively on the negative hydrogen ion density.

1.2 Chapter Outlines

Below is a brief outline of what each of the following chapters contains.

Chapter 2 — A basic overview of low temperature plasma physics with an emphasis on the relevant plasma surface interactions for the production, and destruction, of negative hydrogen ions.

Chapter 3 — A discussion of the experimental set up used, and an explanation of various diagnostic techniques used within this work including: Langmuir probes, laser photodetachment, phase resolved optical emission spectroscopy (PROES), EQP mass spectrometry, and two-photon absorption laser induced fluorescence (TALIF).

Chapter 4 — An experimental investigation of the influence of surface materials upon the volume production of negative hydrogen ions. This chapter investigates multiple metallic surfaces, including: tungsten, copper, aluminium, molybdenum, and stainless steel 304.

Chapter 5 — An experimental investigation of direct surface production of negative hydrogen ions conducted as part of a collaboration with the PIIM group located in Marseille, France. The surfaces investigated are nitrogen doped diamond, with varying nitrogen doping concentration, and a novel electride material.

Chapter 6 — An experimental investigation of the role of metallic surfaces, as investigated in Chapter 4, on the atomic hydrogen densities.

Chapter 7 — Conclusions of the research presented in this project, and a discussion of their wider impact upon the field of negative ion production in low temperature plasmas.

Chapter 2

Background Theory

This chapter focusses on giving the reader a general introduction to basic plasma physics concepts which are important to understand before moving onto more technical details. It gives an overview of nuclear fusion and touches briefly on why we should be interested in its capabilities as an energy source. The focus of this work is to understand the mechanisms which create negative ions, and investigate surfaces which may be of interest for negative ion generation. A general overview of the mechanisms for negative ion creation and destruction is presented within this chapter; this will be referred to within the main body of this thesis, in order to explain certain trends observed within the acquired data.

2.1 Defining a Plasma

Plasmas are often referred to as the fourth state of matter, and whilst such a definition does little to explain what a plasma is, it hopefully gives some appreciation for how different a plasma is from other forms of matter. Whilst there are numerous ways to generate a plasma, the underlying mechanism is the same; energy is provided to a system which results in the ionisation of neutral molecules, and atoms, to produce a positive ion and an electron. These electrons can in turn cause more ionisation events. However, they can also be involved in numerous other collisions which facilitate the highly desirable reactive chemistry attributed to certain technological plasmas.

2.2 Quasi-neutrality

On a microscopic scale, the plasma is a collection of ions, electrons, and neutral species. On a macroscopic scale, the plasma must be quasi-neutral; this means that the total negative charge, including electrons and negative ions, must balance with the total positive charge. It now becomes necessary to define a length scale for how large the system must be to allow for the screening of charge density perturbations, such that it can appear neutral on the macroscopic scale. This length scale is referred to as the Debye length.

2.3 Debye Length

The Debye length can be investigated by firstly envisaging a positive point charge immersed within the plasma. Within this, the electrons will respond quicker to this charge than the ions, as there is a differential in mobility between the charged species due to their difference in mass. Subsequently, the electrons will effectively screen the positive charge by surrounding it.

The Debye length is the distance an observer must be from the charge perturbation in order to no longer experience the associated Coulomb force [4]. Equation 2.1 gives the mathematical definition of the Debye length, λ_D . The ions are considered to be static, relative to the electrons, and therefore only the electron density (n_e) and electron temperature (T_e) are accounted for. The Boltzmann constant (k_b), electron charge (e), and permittivity of free space (ϵ_0) are as expected. If the electron density is increased, then there are more electrons available for screening charge perturbations, hence a smaller λ_D . Conversely, if the electrons have a higher temperature, then a larger λ_D must be required in order to effectively screen the charge perturbation.

$$\lambda_D = \sqrt{\frac{\epsilon_0 k_b T_e}{n_e e^2}} \quad (2.1)$$

2.4 Non-equilibrium Nature

The majority of this work concerns itself with low temperature, low pressure plasmas. The low pressure part of this name is logical, as the plasmas considered here are operated at pressures many orders of magnitude below atmospheric pressure. However, the name low

temperature plasmas may be slightly misleading, for whilst the neutral and ionic species have relatively low temperatures, the electron temperature is much higher. This is due to the preferential heating of the low mass electrons, compared to the higher mass ions and neutrals. The high electron temperature allows for the production of highly reactive chemical species, which can be used to perform surface modifications. Furthermore, this surface modification can be performed whilst being exposed to a relatively low temperature, which is one of the key advantages of using plasmas to affect a surface.

2.5 Bounding a Plasma

Given the aforementioned advantages of using plasmas for surface treatments, it is now prudent to discuss what happens when a boundary is introduced to the plasma. This can be envisaged as a quasi-neutral plasma confined within a box which is many times larger than λ_D . Even if the electron temperature and ion temperature were the same, the velocity of the electrons would be much larger, due to the difference in mass. Therefore, when a wall is introduced, the electrons are able to leave the bulk plasma faster than the ions. Assuming the wall is grounded, then the plasma will be positively biased with respect to the wall. This potential gradient acts to repel additional electrons back into the bulk plasma and accelerates positive ions towards the surface. This area of the plasma is known as the sheath, and it acts to ensure that the ion current and electron current to the wall are equal, such that there is no net change in the charge of the plasma. Figure 2.1 shows the electron density n_e , positive ion density n_i , and potential ϕ as a function of distance from the wall.

The electron density is much smaller than the ion density within the sheath region, whereas quasi-neutrality holds within the bulk plasma. In order to maintain the continuity of ion flux, leading to an ion velocity at the plasma-sheath interface, a presheath must exist. This presheath region has a slowly varying potential which causes the positive ions to accelerate to allow the breakdown of quasi-neutrality within the sheath region. There are a number of ways to treat this presheath region, and for more information the reader is encouraged to read Chapter 6 of *Principles of Plasma Discharges and Materials Processing* [4].

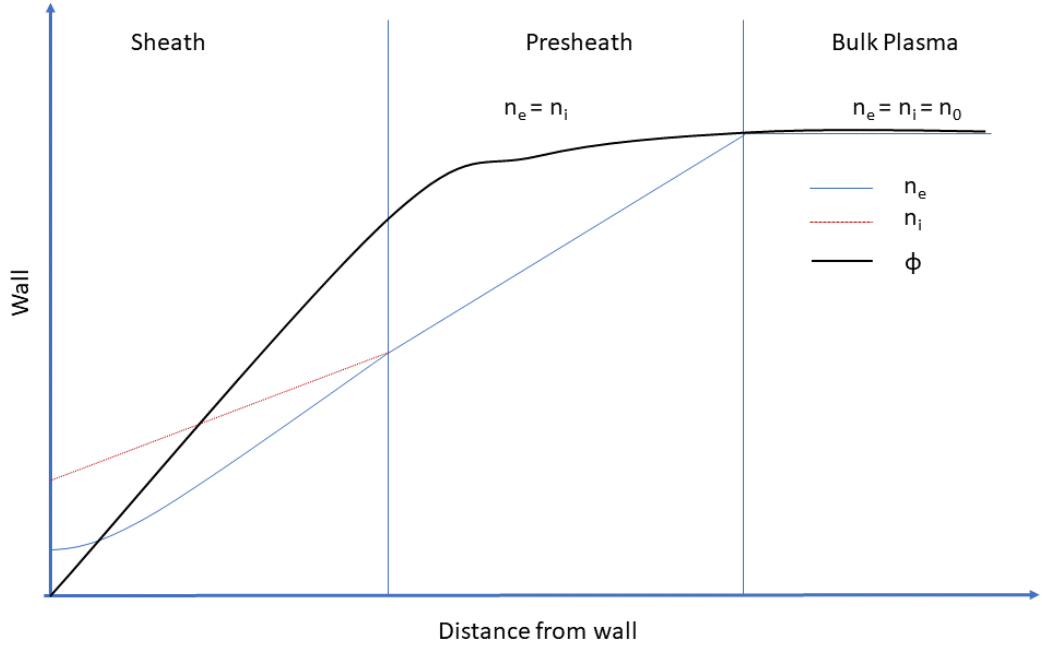


Figure 2.1: Electron density n_e , positive ion density n_i and potential ϕ as a function of distance from the wall.

2.6 Radio-Frequency Plasmas

The plasmas used within this work are either inductively coupled plasmas (ICPs), operated almost exclusively in the electrostatic mode (E-mode), capacitively coupled plasmas (CCPs), and briefly an electron cyclotron resonance (ECR) source. With the exception of the ECR source, which is discussed within Chapter 3, each of these coupling mechanisms will be discussed now.

Radio-Frequency (RF) plasmas operated at 13.56 MHz are a popular choice for low pressure, and atmospheric, plasma sources. A time-varying electric field is applied to one electrode which can selectively act upon the electrons whilst not affecting the ions, as they are too slow to react to the fast time-varying electric field. Conversely, the other electrode is either grounded or left floating.

There are two main mechanisms to couple power into the bulk plasma. The first mechanism is a capacitively coupled plasma in which the electrodes act as capacitor plates with the electric fields running normal between them. This mode has a large observable sheath and can accelerate positive ions to high energies before they are terminated at the grounded electrode; this can be particularly useful for sputtering applications [5]. The second mechanism is an inductively coupled plasma which typically uses a 5-turn copper coil through which the

RF power is applied. This time-varying electric field then induces a time-varying magnetic field below the coil. This goes on to generate an electric field, which oscillates in the same plane as the coil, as described by Faraday's law.

At low plasma densities, inductively coupled plasmas are capacitively driven with the same coupling mechanisms as the parallel plate configuration. As the applied power increases, so does the plasma density, which eventually causes a mode change within the plasma from the capacitive (E-mode) to the inductive (H-mode). This mode change can be observed from the large increase in the luminosity, due to a large increase in the plasma density. Such sources are used heavily within the silicon fabrication industry as they are capable of creating a large plasma density across a large area [6].

2.7 Nuclear Fusion

Nuclear fusion is the process whereby two lighter nuclei are fused together into a heavier one. This process is how our universe was populated by a plethora of increasingly heavy elements, and providing the two elements to be fused are lighter than iron, then energy can be gained from the system. In reality, the lightest elements yield the most energy per nucleon from their fusing. Therefore, the majority of fusion research focusses on the fusion of two isotopes of hydrogen, namely, deuterium (D) and tritium (T). Conversely, our Sun, the most well known fusion reactor, primarily fuses two hydrogen nuclei (p-p) together. However, the cross-section for this reaction is lower than for DT fusion, hence the focus on DT fusion. The products from a DT fusion reaction, as shown by Equation 2.2, are an alpha particle, which due to its positive charge remains confined, and a neutron, which can escape the bulk plasma. The neutron has an energy of 14.1 MeV and will escape the plasma. It will collide with the wall of the chamber and in turn heat the fluid circulating in a cooling blanket. This fluid increases in temperature and turns into an energetic gas, which can in turn rotate a turbine to produce electricity; the same mechanism used for centuries.



This in theory sounds relatively straightforward, however, the energy required to overcome the repulsive force between nuclei is substantial. This requires the plasma to be heated to an extreme temperature, approximately 100 million °C, in order to allow the fusion of

two nuclei. Temperatures this high will melt any solid material that it comes into contact with, therefore, the plasma must be confined by something other than a wall. The Sun achieves this confinement using gravity, however, spatial limitations removes that option on Earth. Therefore, two choices are considered. The first of these is inertial confinement fusion (ICF) which involves the near perfect homogeneous compression of a fuel pellet. This can be achieved in a number of ways, ranging from a conventional fission blast to extremely powerful lasers. Whilst this method has had some success, there are still considerable technical challenges to overcome. The second method of confining the plasma uses magnets; this is known as magnetically confined fusion (MCF). It is worth noting at this stage that due to the incredibly high temperature of fusion relevant plasmas, the ionisation degree is nearly 100 %; this is in stark contrast to the low temperature plasmas that the majority of this thesis considers.

2.7.1 Benefits of Nuclear Fusion

There are a number of clear benefits that nuclear fusion has over currently available energy sources. The advantage it holds over non-renewable, fossil-fuel burning, energy sources should be clear. If I were writing this thesis 20+ years ago, it would have been expected that I discussed the rising levels of CO₂, and consequently the threat of global warming for the future of humanity. The reality is that everyone is very much aware of this threat to our existence, and yet in light of that, not enough is being done to mitigate the enormity of the problem that everyone will soon face. However, there are a number of potential less obvious advantages that nuclear fusion has over its non-fossil fuel competitors. The following points which will be discussed are only a tiny fraction of those worth investigating; for more information, please see *Sustainable Energy - Without the Hot Air* [7].

2.7.1.1 Power Density

One of the key advantages nuclear fusion may have over renewable energy sources is the power density of a reactor. In countries with a large population density, which wish to maintain some semblance of resource and energy independence, relying entirely on renewable energy sources is extremely challenging, if not entirely infeasible. Figure 2.2 helps to illustrate this problem and conveys the need for high power density sources alongside other energy sources. Additionally, Table 2.1 gives some typical power densities for various renewable options and

nuclear fission. Until commercial nuclear fusion is a reality, it is hard to estimate what the power density will be. Nevertheless, a conservative estimate is that the power density of nuclear fusion is comparably to that of nuclear fission [7–9].

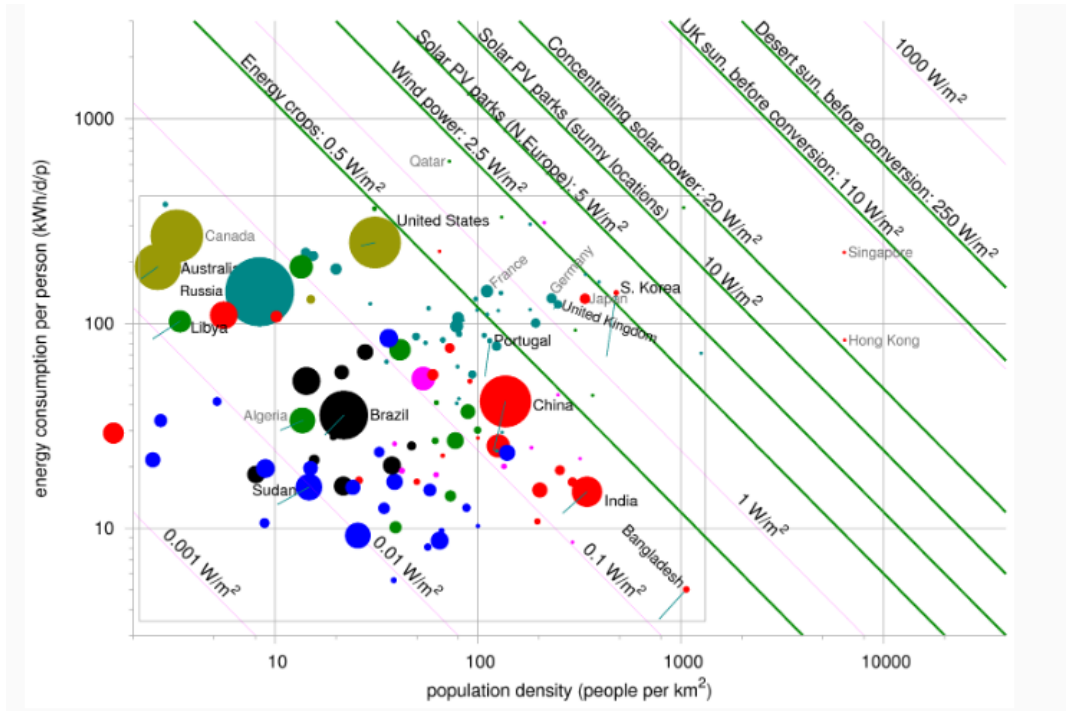


Figure 2.2: A map showing the energy consumption against the population density for various countries around the globe [7].

Source	Power Density (W/m^2)
Nuclear Fission	>100
Solar	10
Wind	2–3*
Biofuel	0.5

Table 2.1: The power density of various energy sources [7]. * depicts a range of the power density from wind in the UK due to discrepancy between onshore and offshore wind.

2.7.1.2 Radioactive Waste

One of the largest problems that nuclear fission suffers from, ignoring the bad publicity from the word nuclear, is the radioactive waste that is generated. For every 2 grams of uranium spent within a reactor, approximately 0.5 grams of waste is produced [7]. In contrast, nuclear fusion reactors produce helium, a by-product which may be useful if it can be extracted without significant cost, and a fast neutron. It is due to these two simple products that

people claim that fusion reactors do not produce any radioactive waste. Unfortunately, this does not take into account the radioactive materials created by high energy neutron bombardment [10,11]; nor does it account for the risks of a significant tritium inventory.

One example of radioactive waste produced in fusion environments is that of the transmutation of tungsten. Tungsten is used heavily in fusion environments due to its high melting point, thermal conductivity, and sputter resistance. However, under high energy neutral bombardment, what was previously pure tungsten will become tungsten-rhenium or tungsten-osmium alloys. Both osmium and rhenium, depending on the isotope, are radioactive and therefore would require proper disposal. This is analogous to current nuclear fission reactors, but without the additional radioactive products being produced in tandem.

2.7.1.3 Resource Distribution Homogeneity

On a broader note, one of the key advantages that nuclear fusion has over other energy sources is the distribution of required reactants. Deuterium can be extracted from seawater, and tritium, whilst incredibly rare, can be bred within the reactor itself from lithium blankets [12]. This is in stark contrast to all other high-power density energy sources. For this, a nation must be fortunate enough to have a large quantity of extractable gas, oil, coal, uranium, plutonium, etc..., in order to have independent control of their nation's energy network.

2.7.2 External Heating

As has been previously discussed, large temperatures are required in order to provide the energy required to overcome the repulsive forces between the nuclei, to create a fusion event. These temperatures can only be achieved through substantial external plasma heating. There are two main types of external heating. Firstly, RF heating, which utilises electromagnetic waves launched into the plasma. The frequency of the waves are chosen so that they resonate with the cyclotron frequency of either the electrons, or the ions, within the bulk plasma [13]. The second option for external heating, which usually provides the majority of the plasma heating, is neutral beam injection.

2.7.3 Neutral Beam Injection

Figure 2.3 shows a schematic representation of a neutral beam injector (NBI) used on the Joint European Torus (JET). The first element to consider is the ion source; conventionally,

these ion sources (labelled as PINI) create a large density of positive ions. The current ion sources are known as DC arc sources and create positive ions via thermionic emission of electrons from heated filaments which are accelerated to the source wall. This causes ionisation of the gas and therefore the ignition of the plasma. Following this, a series of magnetic cusps are used to enhance the density of the plasma and the density of positive ions [14]. The second element to consider, is the accelerator which is essentially a very powerful, >10 MV/m, electrostatic field. Finally, there is the neutraliser which neutralises the energetic positive ions before they reach the port to the torus. Due to large magnetic fields confining the fusion plasma, only neutral species will be able to reach the fusion reactor. Any positive ions that are not neutralised are deflected into an ion dump, as this prevents unnecessary damage to components. The neutral beams have an incredibly high power density, >10 MWm $^{-2}$, that require active cooling, hence the addition of cryopumps around the beam [14, 15].

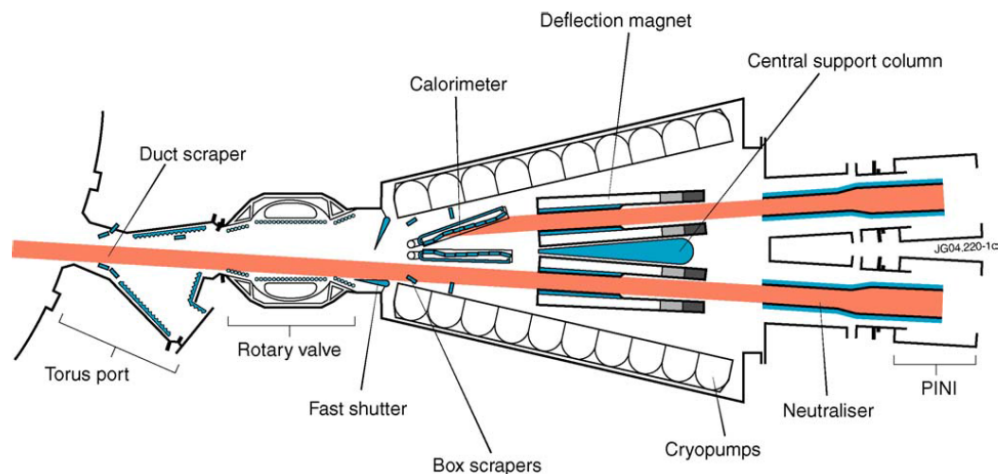


Figure 2.3: A schematic representation of the JET neutral beam injector [16].

2.7.3.1 Negative Ion NBIs

Conventional NBIs use positive ions as the source of ions which are subsequently accelerated and neutralised before heating the core plasma. However, as shown by Figure 2.4 [17], the neutralisation efficiency for positive ions decreases to unacceptably low levels for energies beyond 200 keV/nucleon. In contrast, the neutralisation efficiency for negative ions remains much higher, at approximately 60 %, for energies above 200 keV/nucleon. One of the next

major fusion reactors, ITER, requires 1 MeV/nucleon for up to 1 hour, which is only possible with negative ion NBIs [18].

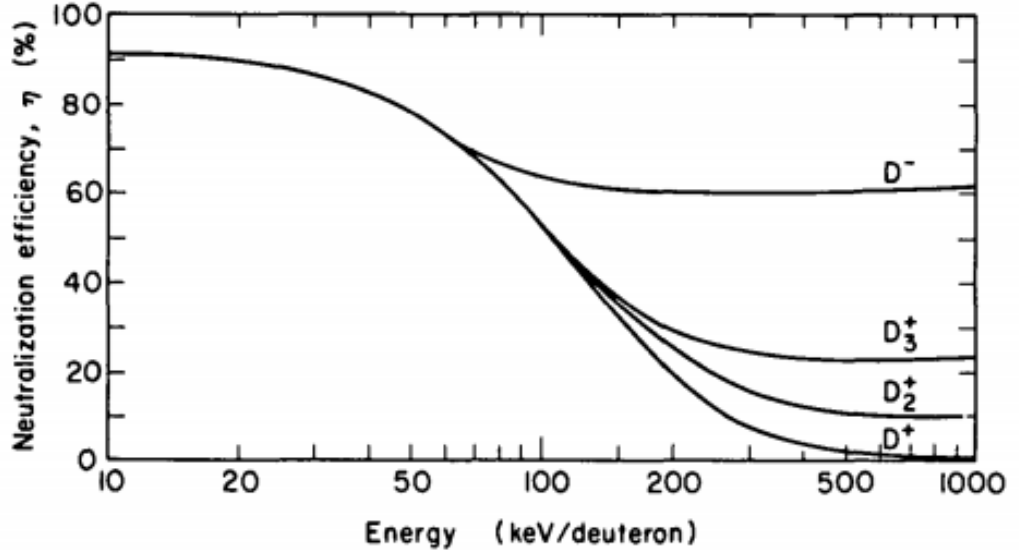


Figure 2.4: Neutralisation efficiency as a function of energy per nucleon, or deuteron. The neutralisation efficiency of negative ions remains high for higher energies [17].

Whilst the solution to the problem facing NBIs is apparent, the solution, to use negative ions in place of positive ions, is not necessarily as straightforward as it may appear; producing large quantities of negative ions is a significant challenge. The requirement for the ITER negative ion source is to achieve 33 mA/cm² of H⁻ [19], with typical extraction rates of negative ions [18] this corresponds to a negative ion density of 2x10¹⁷ m⁻³ [20]. Equally, so is their extraction, especially without co-extracting electrons. Nevertheless, providing a large quantity of negative ions can be created and extracted, then the required external heating for a fusion reactor can be supplied.

2.8 Volume Production of Negative Hydrogen Ions H⁻

Volume produced H⁻ ions are created through a two-step process. Firstly, vibrationally excited molecular hydrogen H₂(v>0) must be created. Secondly, the vibrationally excited hydrogen molecule must collide with a low energy, approximately 1 eV, electron in order generate an atomic hydrogen and a H⁻ ion as denoted by Equation 2.3:



As the density of H^- ions is linked to the density of vibrationally excited hydrogen molecules, it is prudent to discuss the ways in which vibrationally excited molecules of hydrogen can be created, and equally, how they can be destroyed. This section will also focus on the possible ways to destroy H^- ions, once it has been created. All of the processes discussed within this section are only the volume processes, as the following section will discuss the surface effects which are possible [21].

2.8.1 Creation of Vibrationally Excited Molecules

This section will focus only on the creation of vibrationally excited molecules of hydrogen in the volume.

2.8.1.1 Low Energy Electron Excitation

The first possible volume method of creating vibrationally excited molecules is through the collision of low energy, < 5 eV, electrons, as shown by Equation 2.4 [22]. This process is often referred to as e-V excitation with the e in lower case to represent low energy electrons. The electronic state of the initial molecule is conserved, however, the vibrational level is increased by $\Delta v = v_f - v_i$, where v_f and v_i are respectively the final and initial vibrational levels. $\Delta v = 1$ is the most probable change in the vibrational level, with a cross-section of $\langle \sigma v \rangle_{eV} = 2 \times 10^{-15} \text{ m}^3\text{s}^{-1}$. e-V excitation is only responsible for populating the lower vibrational levels, up to $v_f = 4$ [23, 24].



2.8.1.2 High Energy Electron Excitation

In contrast to e-V excitation, high energy electron excitation is often referred to as E-V excitation, and can populate the higher vibrational energy levels $v_f > 4$. E-V excitation is a two step process. Firstly, high energy electrons, > 20 eV, collide with ground state molecular hydrogen and excite it into an upper electronic state. These upper states eventually undergo radiative decay and relax back to the ground state, but they do possess a higher vibrational

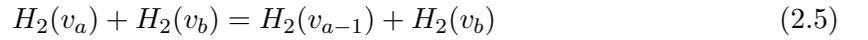
level. The cross-sections for these vibrational excitations can be estimated using the relevant Frank-Condon factors [25]. The cross-section depends on Δv , however, for $v_f = 7$ then $\langle \sigma v \rangle_{EV} = 5 \times 10^{-17} \text{ m}^3\text{s}^{-1}$ [23, 26].

2.8.2 Destruction of Vibrationally Excited Molecules

This section will focus only on the destruction of vibrationally excited molecules of hydrogen within the volume.

2.8.2.1 Vibration-Translation Reactions with Molecules

Vibration-translation interactions can occur between vibrationally excited molecules and either molecules, or atoms, labelled respectively as V-T and V-t. Equation 2.5 outlines this mechanism. The cross-section for the molecular reaction at $a = 7$ is $\langle \sigma v \rangle_{VT} = 1 \times 10^{-18} \text{ m}^3\text{s}^{-1}$ [24]. This pathway is generally not as important as the relaxation pathway between vibrational species and atoms, due to the smaller cross-sections.



2.8.2.2 Vibration-translation Reactions with Atoms

This relaxation pathway is the parallel version of the V-T pathway, with $v_f < v_i$. However, the cross-section for this reaction is much larger, $\langle \sigma v \rangle_{Vt}$ is between 1×10^{-15} and $1 \times 10^{-16} \text{ m}^3\text{s}^{-1}$ [27]. Figure 2.5 shows the comparison of the V-T and V-t relaxation cross-sections; the dashed line shows the V-t pathway, labelled at A-DX [27].



2.8.2.3 Ionisation of Vibrationally Excited Molecules

Vibrationally excited hydrogen can be ionised through an electron impact collision to create a molecular ion and an additional electron, as shown by Equation 2.7. The cross-section for this reaction increases for higher vibrational levels [28], for example, at $v = 0$ $\langle \sigma v \rangle_{Ion} = 9 \times 10^{-16} \text{ m}^3\text{s}^{-1}$ [24].

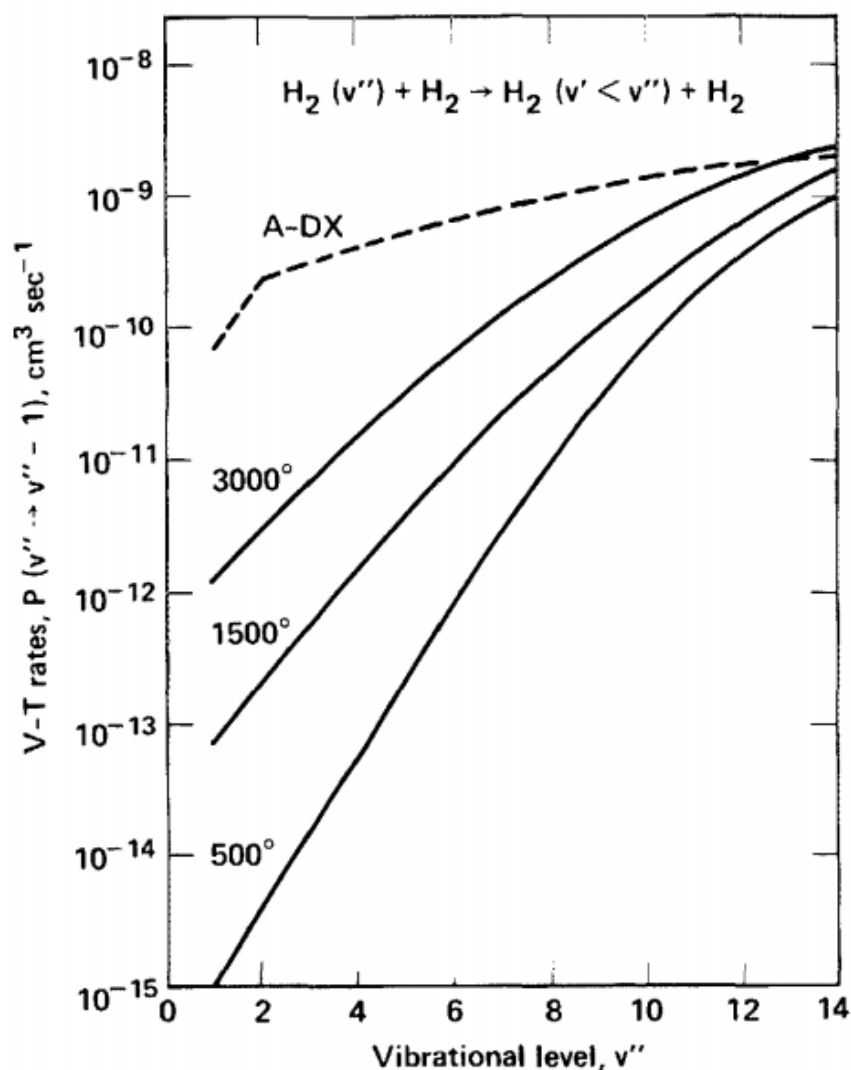


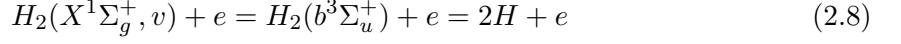
Figure 2.5: A comparison of the cross-sections for V-T and V-t relaxation, with the dashed line depicting the de-excitation from atomic collisions [27].



2.8.2.4 Dissociation of Vibrationally Excited Molecules

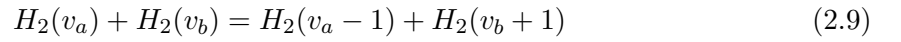
Dissociation of vibrationally excited molecules is a two-step process, as shown by Equation 2.8. Firstly, an electron impinges upon an electronic ground-state, vibrationally excited molecule, causing an electronic excitation to an electronically repulsive state. The electronic states are labelled in this section as they are important to the process at hand. Finally, the

electronic repulsive state dissociates. The cross-section increases with increasing vibrational energy level, for example, an electron temperature of approximately 1 eV for $v = 4$, $\langle \sigma v \rangle_{Dis} = 1 \times 10^{-16} \text{ m}^3\text{s}^{-1}$ [29].



2.8.2.5 Vibrationally Excited Molecule Collisions

Collisions can occur between two vibrationally excited molecules which acts to populate the lower vibrational energy levels whilst simultaneously depopulating the higher vibrational levels. This is often referred to as the V-V process, and is depicted by Equation 2.9. The cross-section for this reaction is dependent on the two vibrational energy levels, for example, at $a = b = 7$, $\langle \sigma v \rangle_{VV} = 1 \times 10^{-17} \text{ m}^3\text{s}^{-1}$ [24].



2.8.3 Destruction of H^- ions

There are three main mechanisms that can destroy the population of H^- ions, each of which will be discussed in turn within this section.

2.8.3.1 Mutual Neutralisation

This process involves the collision of a H^- ions with a positive ion. There are three positive ions that must be considered for a hydrogen plasma, and each of these reactions are presented by Equations 2.10–2.12. The cross-sections $\langle \sigma v \rangle_{MN}$ for these reactions are approximately $9 \times 10^{-14} \text{ m}^3\text{s}^{-1}$ [30].



2.8.3.2 Electron Detachment

The electron in a H^- ion is only loosely bound, with an energy of approximately 0.75 eV [31], which allows even relatively low energy electrons to cause detachment events. The cross-section for this interaction is heavily dependent on the electron temperature, $\langle \sigma v \rangle_{ED_{1.5eV}} = 2 \times 10^{-14} \text{ m}^3\text{s}^{-1}$ [32] and increases with increasing electron temperature [33].



2.8.3.3 Associative Detachment

Associative detachment involves the destruction of H^- ions via atomic collisions. A combination of associative detachment and electron detachment can create a cascading effect as one feeds into the other. The cross-section $\langle \sigma v \rangle_{AD}$ is approximately $1.5 \times 10^{-15} \text{ m}^3\text{s}^{-1}$ [24,30].

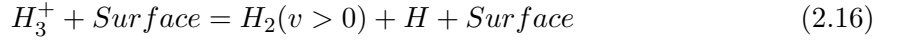
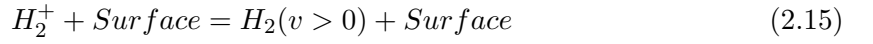


2.9 Plasma surface interactions

The affect that the surface can have on the bulk plasma is substantial. For example, the predominant loss mechanism for atomic species, such as hydrogen, in low pressure RF plasmas is due to the diffusion to the walls [24]. The probability of the atom being lost is dependent on the surface and is typically discussed in terms of surface loss coefficients. The focus of this work is on the generation of H^- ions, for which surfaces are incredibly important. For whilst the H^- ions can be created in the volume, as discussed previously, they can also be created through direct surface production processes. Furthermore, vibrationally excited species can be created or destroyed through interactions with the surface, which must be considered alongside the volume processes.

2.9.1 Surface Assisted Excitation

This mechanism is caused by the interaction of positively charged molecular ions of hydrogen, H_2^+ and H_3^+ , and the surface [34]. It is capable of populating all vibrational states, and it has been observed that H_3^+ ions are more favourable for the generation of negative ions due to the increased population of $H_2(v>5)$ compared to the H_2^+ mechanism [35].



2.9.2 Atomic surface interactions

Atomic species can be lost through various interactions with a wall. Firstly, when an atom impinges upon a surface, it will gain energy due to the interaction of the unbound electron and the surface which forms a chemical bond. Typically, the energy gained is approximately 2.4 eV for hydrogen and metallic surfaces [36]. These adsorbed atoms can then undergo different mechanisms for their release, as depicted by Figure 2.6. The Langmuir-Hinshelwood (LH) [36] recombination process involves two adsorbed atoms recombining to create a molecule. The H-H bond energy is approximately 4.5 eV, making this process endothermic by 0.3 eV. The second mechanism, known as Eley-Rideal (ER) recombination [37, 38], involves an impinging atom reacting directly with a previously adsorbed atom, again creating a molecular species. This process is exothermic by approximately 2 eV, as only one atom is absorbed onto the surface during the recombination process. These two mechanisms are idealised as an impinging atom requires time to reach thermal equilibrium with the surface. This is a third surface recombination process in which the impinging atom is first weakly bound to the surface and is able to move relatively easily across the surface; this allows energy to be transferred to other adsorbed species. This process was first proposed by Harris and Kasemo as the *Hot Atom* (HA) recombination process [39]. Since this paper, multiple studies have given evidence that the ER mechanism alone cannot account for observations [40, 41]; providing indirect support for the existence of the HA process. Both the ER and HA processes can produce vibrationally excited molecules, this was first observed by Hall *et al.* [42].

2.9.3 Relaxation of Vibrationally Excited Species via Surface Collisions

The relaxation of vibrationally excited species through interactions with the wall is one of the most dominant mechanisms for their destruction, assuming a chamber size below 30 cm [43]. Equation 2.17 outlines the process of relaxation in this manner, in this instance, v_i

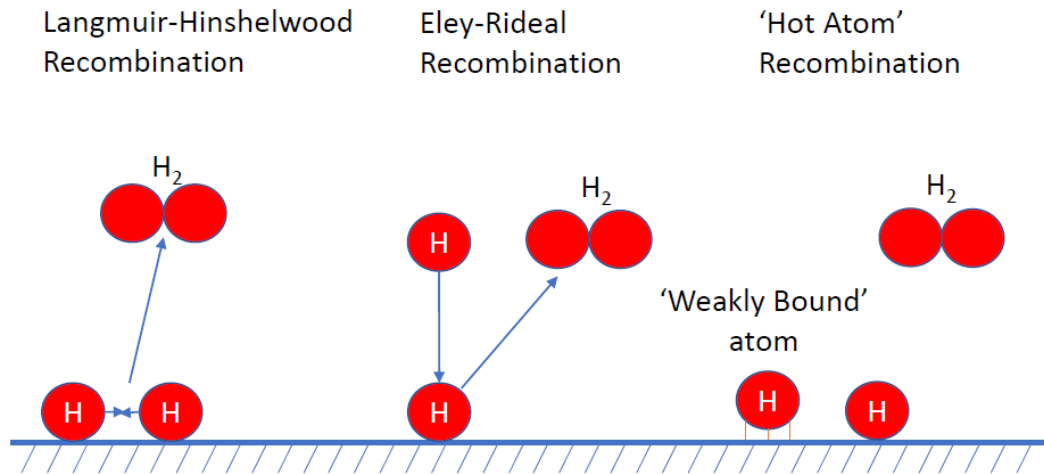


Figure 2.6: Three types of atom-surface interactions. From left to right: Langmuir-Hinshelwood recombination; two absorbed atomic hydrogen particles can recombine producing a molecular hydrogen, Eley-Rideal recombination; an impinging atomic hydrogen directly reacting with an absorbed hydrogen producing a molecular hydrogen, and *Hot Atom* recombination; a weakly bound hydrogen atom reacts with an absorbed atom producing molecular hydrogen.

$> v_f$.



2.9.4 Direct Surface Production of H^- Ions

It has been previously discussed how H^- ions can be produced through dissociative attachment within the bulk plasma, and how surfaces are important for the production and destruction of vibrationally excited molecules. However, the direct production of negative ions from a surface has not yet been discussed. Surface produced negative ions are of significant interest, predominantly due to how easy they are to extract from the plasma, and as previously discussed, for their application in neutral beam injection. There are a number of mechanisms in which they can be produced, each of these will be discussed in turn.

2.9.4.1 Atomic Processes

There are two mechanisms whereby atomic hydrogen can directly produce H^- ions from the surface. Firstly, if an hydrogen atom collides with a surface with an energy larger than the work function of the surface, it can liberate an electron and be reflected as a H^- ion. The

probability of a negative ion being produced under these conditions depends on the surface properties.

$$H_{fast} + Surface = H^- + Surface \quad (2.18)$$

The second mechanism whereby atoms can produce negative ions involves low energy thermal atoms. As previously discussed, in Section 2.9.2, a hydrogen atom can be adsorbed by a surface. Subsequently, it may capture an electron from the surface of the material. This is only possible if the electron affinity of the surface is lower than that of a hydrogen atom, 2.1 eV [44]. Whilst this is a possibility in some circumstances, especially those involving caesiated surface, it becomes increasingly negligible for higher work function materials.

2.9.4.2 Ionic Processes

The fundamental mechanism for the creation of negative ions due to positive ion bombardment of a metallic surface has been well established for a number of years [45–47]. The capture of an electron from a surface is dependent on two key parameters. Firstly, the energy difference between the affinity level of the negative ion and the Fermi level, or valence band, of the surface. Secondly, the overlap of the wave function between these two states, as this governs the exchange rate. Both of these parameters are dependent on the separation between the surface and the particle, as well as the velocity of the particle. As the separation distance is decreased, the affinity level is lowered. This allows a quasi-exponential increase in the electron tunnelling rates between the surface and the particle [48], which occurs in both directions; this is known as resonant charge transfer [49]. At a certain separation between the surface and the species, any information regarding the initial charge state is lost; this is known as the memory loss effect. As the negative ion moves away from the surface, the affinity level increases back to its previous level and may overlap with empty states within the conduction band of the metallic surface. This overlap allows the electron to return to surface, and destroys the negative ion before it can leave. However, if the velocity of the negative ion is large enough, then there is insufficient time for the electron to leave the negative ion and fill empty states within the conduction band. It can now be imagined that there is a critical distance, dependent on velocity, where the transfer rate of electrons becomes negligible. Here, the produced negative ions are not subject to the possibility of electrons returning to the surface. This distance is known as the freezing distance; for a much more

detailed treatment of this phenomenon, please refer to Los *et. al.* [50].

One way of increasing the number of negative ions generated directly through surface processes is through the deposition of caesium onto the surface. For example, the work function of tungsten is 4.55 eV [51], which can be reduced to as low as 1.5 eV if approximately half a monolayer, a monolayer that covers approximately half of the surface, of caesium is deposited onto the surface [52]. By lowering the work function of the surface, the energy barrier, the difference between the affinity level and the valence band, is reduced. This moves the freezing distance into a location where negative ions are more dominant and results in an increase in the extracted density of negative ions.

Insulating materials are also able to produce negative ions, even though the electrons in these are more deeply bound than those in metallic surfaces; a mechanism for their generation has been proposed [53]. This mechanism suggests that the reduction in the affinity level, due to a decrease in the separation between the species and surface, is further amplified by a coulomb interaction between the negative ion and the localised hole. Furthermore, the destruction of the formed negative ions, due to the transfer of electrons back to the surface, is most likely negligible due to a lack of empty states in the band gap of the insulator [53, 54].

Chapter 3

Methodology

This Chapter describes the experimental setup of the plasma sources used within this thesis. The plasma source used for Chapters 4 and 6, located in York, UK, is a Gaseous Electronics Conference (GEC) reference cell [55]. The plasma source used for Chapter 5 is the Plasma Helicon to Irradiate Surfaces In Situ (PHISIS) reactor, situated in Marseille, France. The experimental procedure and relevant background theory of various diagnostics including, laser photodetachment, phase resolved optical emission spectroscopy (PROES), EQP mass spectrometry, and two photon absorption laser induced fluorescence (TALIF), is also discussed.

3.1 Gaseous Electronics Conference Reference Cell

A GEC reference cell was used as the plasma source for both Chapters 4 and 6 of this thesis. The GEC reference cell is able to be capacitively coupled or inductively coupled [56, 57], however, for all the measurements taken in this work, it was operated exclusively in the inductively coupled setup. Within this, the inductive power is coupled through a 5-turn copper coil positioned at the top of the GEC reference cell. The coil is water cooled through a central cooling channel, located in the middle of the hollow coil; this has an internal diameter of 4.76 mm (3/16"). As explained previously, in Section 2.6, the inductive coupling has two distinctive modes, E-mode (Capacitive) and H-mode (Inductive).

Figure 3.1 shows a schematic representation of the GEC reference cell, whilst a number of aspects are identical to the classical design, such as: electrode diameter, flange sizes, a symmetric pumping manifold, and gas flow there are a number of deviations from this design [58]. These changes include: a non-showerhead top electrode, an inductive coil loop,

a partially variable electrode spacing, and an elongated connection to the turbo pump. The plasma is driven by a 13.56 MHz Advanced Energy, Cesar 1310 Radio-frequency generator. This is followed by an Advanced Energy, RF Navio automatic matching box before being coupled into a 5-turn copper coil situated on the top electrode. The copper coil is separated from the electrode spacing via a quartz window, which in turn is surrounded by a stainless steel electrode. The lower electrode is grounded in all instances of this work, however, it can be powered, or floating, if the application required it. This electrode is surrounded by a grounded guard ring and is water cooled through channels beneath the electrode to a constant temperature of $20 \pm 0.1^\circ\text{C}$. The separation of the two electrodes has been measured to be 42 mm.

The pressure of the chamber is reduced through the use of a Pfeiffer Vacuum, Duo 20MC rotary-slide-vane pump (labelled as a floor pump). The lowest pressure that can be achieved through this pump alone is 1×10^{-2} Pa. However, the pressure can be further reduced, if required, by an Oerlikon, Turbovac MAG W 600iP turbo molecular pump. The gas flow is regulated by a number of MKS mass flow controllers, depending on the admixtures of gases required, with the pressure being regulated via a MKS 253A butterfly valve.

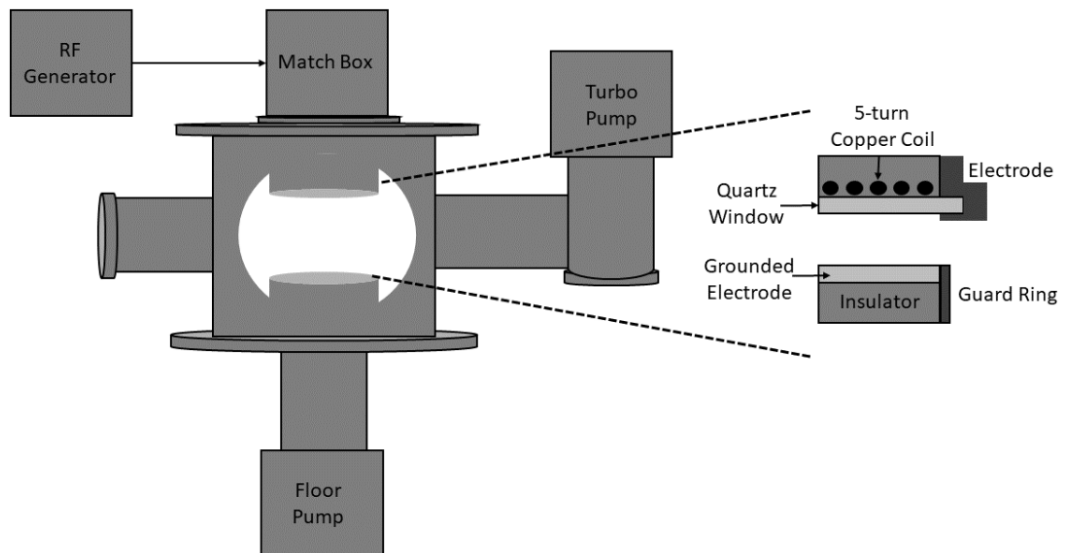


Figure 3.1: A schematic representation of the GEC reference cell. A zoomed in view of the electrodes is also shown.

3.2 Langmuir Probes

Of all the ways to diagnose a plasma, the Langmuir probe is almost certainly the simplest, as it only consists of inserting a metallic wire into the plasma, varying the applied voltage, and measuring the current drawn. However, this diagnostic method has significant drawbacks, including: complex mathematical derivations; due to the nature of interpreting IV (current voltage) curves, engineering complications; to ensure that the wire can withstand the conditions within the plasma bulk, and technical challenges; to ensure the wire does not dramatically perturb the plasma, which would result in inaccuracies in the measurements. Even with these challenges, Langmuir probes still prove to be incredibly useful at diagnosing plasmas [59–61].

3.2.1 Regions of an IV Curve

Figure 3.2 shows an example of an IV curve taken within the GEC reference cell. Initially, a large negative bias is applied to the probe tip, the electrons are repelled from this negative bias, and a positive sheath potential is created. Due to the differential in mass between the ions and the electrons, the ions cannot respond as quickly to this potential change. This results in a limited current drawn, regardless of the size of the negative potential applied. This portion of the IV curve is known as the ion saturation region, and is depicted by I_{sat} ; this region of the IV curve can be used to find the positive ion density n_i . Assuming that the electron temperature T_e is much larger than the ion temperature, which is true in many low temperature plasmas, then the ion current is not given by the ion thermal speed, but by the Bohm ion current. The reason for this is that both the electron density and positive ion density must decrease as the particles approach the negatively biased probe tip. However, in order to create a positive potential, the ion density must exceed the electron density at the sheath edge, and decrease in density more slowly than electrons towards the probe tip. To achieve this, the ions must have a larger velocity than the Bohm velocity. Equation 3.1 outlines the current drawn under such conditions, which, assuming knowledge of the electron temperature, surface area of the probe, and dominant ion mass, can be trivially rearranged to find the positive ion density [62].

$$I_{sat} = I_{Bohm} = 0.6en_i\sqrt{\frac{kT_e}{m_i}}A_{probe} \quad (3.1)$$

Increasing the bias allows electrons with higher energies to reach the surface, as the bias continues to increase (positively), the number of electrons that can reach the surface increases. Eventually, the number of electrons that can reach the surface is equal to the number of positive ions, assuming singularly charged positive ions in this instance, which results in a net current of zero. This is called the floating potential, and is depicted as V_f in Figure 3.2.

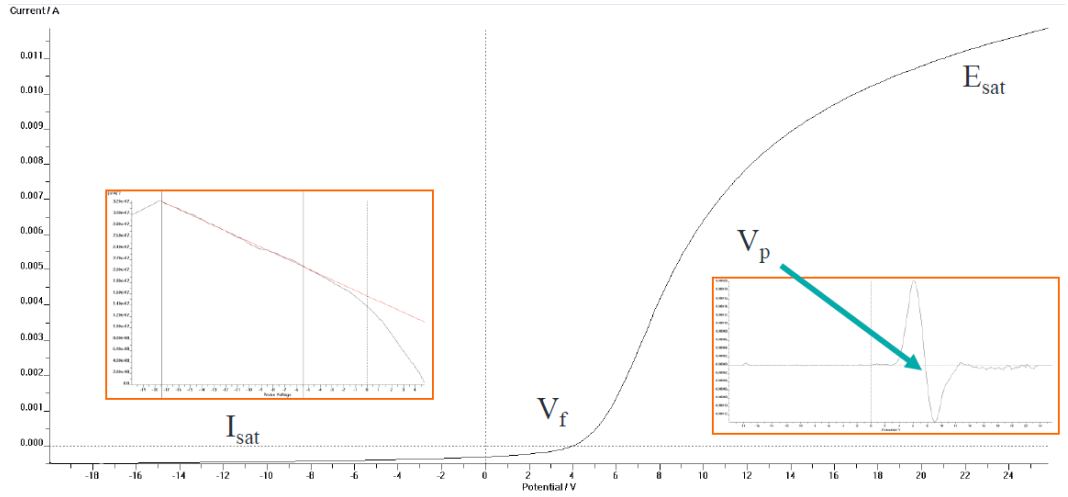


Figure 3.2: An example IV curve for the GEC reference cell.

As the voltage continues to increase, the positive ions are repelled from the surface and the electrons continue to be attracted to this potential; this is known as the transition region. Here, the ion current is assumed to be negligible, and providing that the electrons have a Maxwellian distribution, an exponential increase of the current with voltage can be observed. As the potential continues to increase, the curve deviates from this exponential because the repulsed electrons begin shielding the probe from the bulk plasma. This deviation can be used to calculate the plasma potential V_p in a number of ways. However, in this work, it has been defined as the crossing point of the second differential of the current, with respect to voltage. Equally, assuming that the electron distribution is Maxwellian, the electron temperature can be found from this portion of the IV curve. This is done by plotting the IV curve semi-logarithmically against the probe voltage. The inverse of the slope of the curve ($\ln(I) - V_p$) yields the electron temperature in eV [63]. This is a necessary step towards calculating the positive ion density.

Increasing the applied voltage beyond V_p denotes the beginning of the electron saturation regime, labelled as E_{sat} in Figure 3.2. The measured current increases with voltage only

because the sheath thickens. It is possible to use this section of the IV curve to measure the electron density n_e , however, this is only true if the mean free path of the electrons is very large. Ultimately, it is easier, and creates far less technical challenges, to measure n_e by assuming quasi-neutrality, and measuring the ion density from the ion saturation portion of the IV curve as previously discussed.

3.2.2 Introduction to the Mathematical Formalisation

There are a number of possible mathematical formalisations that can be used to determine the current drawn by a Langmuir probe. These are dependent on the shape of probe and the assumed distribution of the species of interest. The simplest of these is that of Allen-Boyd-Reynolds which describes the motion of charged particles with very low energy. This theory describes the motion of ions from an infinitely long radial position, where the potential is assumed to be zero, before being radially drawn to the probe. Whilst this formalisation can prove useful in some circumstances, it neglects the orbital motion of charged particles around the surface of the probe. The theory that is used within this thesis, first proposed by Mott-Smith and Langmuir [63], is orbital motion limited (OML) theory. This theory assumes that quasi-neutrality is perfect beyond the sheath region and that there is no boundary between the bulk plasma and the sheath, i.e. there is no presheath.

A simple description of OML theory is presented here, however, for more information, please refer to Allen et. al. [64]. Firstly, a cylindrical probe is considered. Here, it is assumed that the length of the probe (l) is much larger than the radius of the probe tip (r_p). By considering the conservation of energy (Equation 3.2) and angular momentum (Equation 3.3), it becomes possible to define an impact parameter (p), as shown by Equation 3.4. Here, m is defined as the mass of the charged species, v_0 is defined as the initial velocity, v_p is defined as the velocity at the probe's surface, V_p is defined as the potential at the probe's surface, and p is defined as the impact parameter.

$$\frac{1}{2}mv_0^2 = \frac{1}{2}mv_p^2 + eV_p = -eV_0 \quad (3.2)$$

$$mv_0p = mr_pv_p \quad (3.3)$$

$$p = r_p \frac{v_p}{v_0} = r_p \left(1 + \frac{V_p}{V_0}\right)^{1/2} \quad (3.4)$$

The contribution to the current, due to electrons within a defined narrow velocity range (dn), is given by the product of the flux crossing unit area, only in electrons perpendicular to the probe axis, and the surface area of the effective collection radius. Equation 3.5 shows the contribution of the current due to this narrow electron velocity range:

$$dI = 2\pi r_p l e \left(1 + \frac{V_p}{V_0}\right)^{1/2} \frac{v}{\pi} dn \quad (3.5)$$

From here, it is necessary to consider the distribution of the electron velocities to define dn as a function; this can be considered to be a Maxwellian distribution. Once this has been completed, it is then possible to integrate over each velocity contribution to define the total current. For the full mathematical derivation, please refer to Mott-Smith and Langmuir [63].

The OML theory is limited, as it assumes that the differential of the potential variation $V(r)$ is approximately constant, such that no absorption radius exists. It also assumes that the sheath thickness is significantly larger than the radius of the probe tip. The theory has been extended by Bernstein and Rabinowitz [65], and Laframboise [66], however, in this work, OML theory has been used throughout.

3.3 Photodetachment

Langmuir probes can be combined with an incident laser beam in order to gain information about the negative ions within the plasma; this technique is known as laser photodetachment. This method was used in Chapter 4 — *Influence of the surface material on the volume production of negative hydrogen ions*, to measure the negative hydrogen ion (H^-) densities above different metallic surfaces. It is worth noting that whilst laser photodetachment was only conducted within this work to measure the densities of H^- ions, it can in theory be used to measure their velocities and temperatures [67–70].

3.3.1 Background Theory

A Langmuir probe is used to measure the electron density in a specific region of the plasma. Negative ions are not measured by Langmuir probes as their mass is much larger than an

electron's, resulting in a lower mobility, which therefore limits their contribution to the overall measured current. Negative ions are measured by firstly detaching an electron from the ion. This electron can subsequently be detected by the Langmuir probe, and measured as an additional current. This requires a method to detach the electron. In this work, this is done by using a pulsed laser with a photon energy large enough to detach the electron from the negative ion. It also necessitates an additional measurement of the electron density, with the difference between the two measurements – one with the laser pulse and one without – to yield the negative ion density.

There are a number of considerations that are necessary to make before conducting laser photodetachment. Firstly, the laser beam must be large enough to cover the collection radius of the probe tip, otherwise an accurate ratio of negative ions to electrons cannot be established. Secondly, the beam energy must be large enough to ensure that all the negative ions within the beam undergo photodetachment. The cross-section for the photodetachment of hydrogen is shown by Figure 3.3 [22]; the peak cross-section is very large, because of the low electron affinity of hydrogen. This means that photodetaching the majority of the electrons from H^- is relatively easy with modern day lasers. However, care must be taken to ensure that the ionisation of neutral atomic hydrogen does not take place. Finally, the photodetached electrons must be measured by the Langmuir probe, therefore, the potential applied to the Langmuir probe must be large enough to ensure detection. These points are discussed in greater detail, and alongside the relevant experimental results, within the *Experimental Benchmarks* section of Chapter 4.

3.3.2 Experimental Procedure

In order to measure the negative ion densities, laser photodetachment was conducted. The Q-switched Nd:YAG laser, which was used, with the frequency doubling option (Continuum, Minilite II), provides narrow-band radiation at a wavelength of 532 nm, in pulses of 20 mJ, within a 5 ns duration, at a frequency of 10 Hz. The laser output beam, with a diameter of 3 mm, is aligned along the dog-legged part of the Langmuir probe tip, a tungsten wire that is 0.15 mm in diameter and has a length of 9 mm. The probe tip was located 9 mm above the central point of the installed sample, approximately 33 mm below the powered electrode. The probe tip was connected into an insulating alumina shaft which allowed the signal to be routed through filtering components located away from the probe tip.

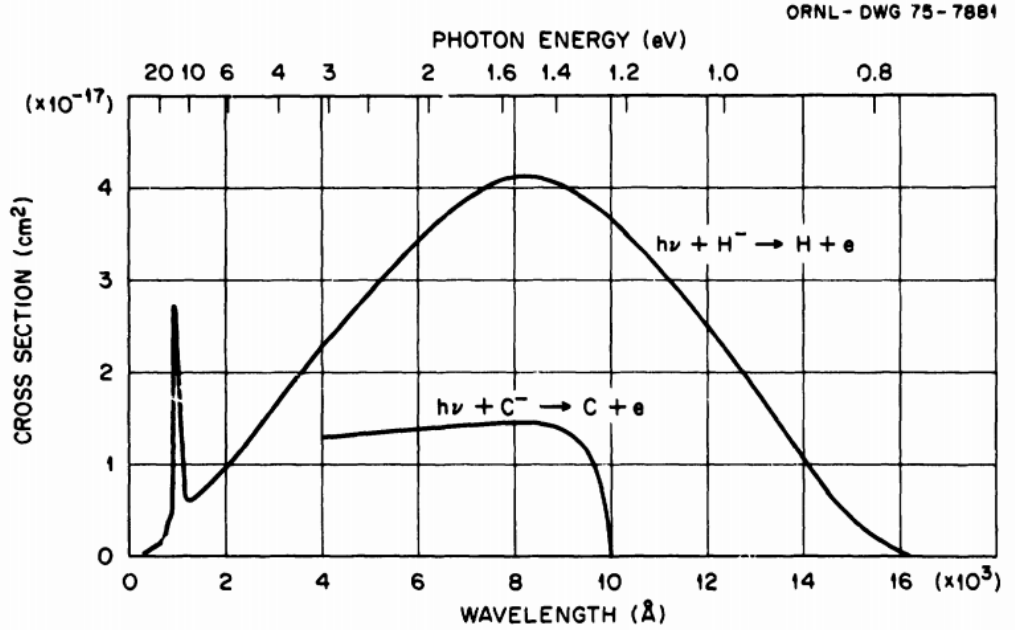


Figure 3.3: Cross-section for photodetachment of electrons from H^- and C^- [22].

The Langmuir probe was first used to acquire an IV-curve through the use of a dedicated Hiden ESPion controller. From this IV-curve, the plasma potential (V_p) was calculated by using the crossing point of the second differential. For the photodetachment measurements, the probe must be biased above the plasma potential. This is done in order to ensure that the majority of the photodetached electrons from the laser interaction volume are collected, whilst not creating measurable secondary emission effects. The current, corresponding to the applied voltage (V_{app}), was then recorded from the IV-curve. In order to measure the photodetachment signal, the Hiden ESPion controller was then disconnected, and the probe connected to a DC power supply (HP 6115A 0-50 V) and the DC $1 \text{ M}\Omega$ output of a Teledyne Lecroy Wavesurfer 3054 oscilloscope. The analysis circuitry for these experiments was based on J. Santoso et. al. [71]. The probe was cleaned regularly to avoid the adverse effects of deposits on the tip. The cleaning procedure involved positively biasing the tip, at 60 V, in a 500 W continuously driven hydrogen plasma.

Once the photodetachment pulse was measured, it was averaged over 128 scans to reduce background noise. The maxima of the photodetachment pulse was compared to the current at V_{app} ; this was done to calculate the H^- fraction, with respect to the electron density ($\frac{\Delta I}{I}$). In order to find absolute densities, it was necessary to establish the electron density. The electron density and electron temperature was calculated using the Hiden ESPsoft software

package based on the OML probe theory [63,64]. Whilst this is possible, it was typically less reliable than finding the positive ion density (n_i) from the ion saturation regime. This, under the assumption of quasi-neutrality, can be used to find the absolute negative ion density, as shown in Equation 3.6. It is worth noting that RF-driven plasmas at this pressure, < 100 Pa, tend to be dominated by H_3^+ ions [72] and as such, a mass number of three was used during the analysis routine.

$$n_{H^-} = \frac{\Delta I}{I} \cdot \frac{n_i}{(1 + \frac{\Delta I}{I})} \quad (3.6)$$

3.4 Phase Resolved Optical Emission Spectroscopy

Important information regarding the plasma dynamics can be obtained by measuring the optical emission with respect to time within the RF-cycle. This technique is known as phase resolve optical emission spectroscopy (PROES), and has been used to investigate the ionisation and excitation dynamics of phase-dependent species, primarily focussed on electron dynamics [73,74]. Consequently, this work focusses on the emission from the hydrogen α Balmer line (656 nm), and primarily uses PROES as a method for assessing the relative density of secondary electrons produced between different metallic surfaces. The results of this work are presented within Chapter 4 — *Influence of the surface material on the volume production of negative hydrogen ions*.

3.4.1 Background Theory

The change in the population of an excited state n_i , from which the detected photons are emitted, depends on a number of factors. Firstly, direct electron impact excitation from the ground state, n_0 to n_i . Secondly, population of n_i through electron impact excitation of metastable states. Thirdly, population from higher excited state cascading down to the state i . Finally, the depopulation of the excited state i , due to spontaneous emission. At the pressure regime investigated within this work, >15 Pa, the populating of n_i from cascade effects, and from metastable excitation, especially when dealing with diatomic gasses, are negligible. This is because of the low population of these states, due to quenching from the molecular species [75]. By ignoring the negligible effect of cascades and metastable excitation, an excitation function can be defined $E_i(t)$, as shown by Equation 3.7:

$$E_i(t) = \frac{1}{n_0 A_{ik}} \left(\frac{d\dot{n}_{Ph,i}(t)}{dt} + A_i \dot{n}_{Ph,i}(t) \right) \quad (3.7)$$

The number of photons emitted per unit volume and time is defined as $\dot{n}_{Ph,i}(t)$ and is equal to the product of the transition probability of the observed emission A_{ik} and n_i . The effective decay rate is shown by Equation 3.8:

$$A_i = \sum_k A_{ik} g_{ik} + \sum_q k_q n_q \quad (3.8)$$

Here, g_{ik} is the optical escape factor and k_q is the quenching coefficient of species q of density n_q . The effective decay rate accounts for the spontaneous emission and the relaxation of n_i via collisional quenching. The inverse of the effective decay rate yields the effective lifetime. It is possible to estimate the effect of quenching on the effective decay rate by estimating, or measuring, the temperature of the gas. However, in this work, the effective lifetime of n_i was measured as part of the process to measure the ground state atom density via two-photon absorption laser induced fluorescence. This diagnostic method, including the method of acquiring the effective lifetime, is discussed in Section 3.6.

3.4.2 Experimental Procedure

The plasma emission as a function of the phase within the RF-cycle was detected with an iCCD camera (Andor iStar, DH344T-18U-73), with a 656 nm interference filter installed (to provide sensitivity for the hydrogen α Balmer line), and a digital delay generator. The TTL output of the rRF generator was used to externally trigger a digital delay generator (DDG), which in turn inserted a delay before sending a trigger to the camera. The imaging plane of the camera was chosen to be as close to the Langmuir probe measurements as possible. This was completed by acquiring images with the probe tip prior to plasma exposure, in order to confirm alignment of the camera. All of the experimental measurements were conducted without the Langmuir probe inserted.

The PROES images presented in this study were taken with an exposure of 6.4 seconds, and gate width of 3.6 ns, it is worth noting that the optical gate has a large rise and fall time, resulting in only 1.7 ns of *full* acquisition. Following the acquisition at one point in the rf cycle, a 2 ns delay is introduced by the DDG, and the measurement procedure begins again. This procedure is repeated for at least 1 rf cycle, although, more may be conducted

in order to check for consistencies between rf cycles.

3.5 Collaboration with the Physics of Ionic and Molecular Interactions (PIIM) group in Marseille

This section of the methodology is related to Chapter 5 — *An investigation of direct surface production of negative ions from novel surfaces.*

3.5.1 Description of the Reactor

Figure 3.4 (a) shows a schematic representation of the Plasma Helicon to Irradiate Surfaces In Situ (PHISIS) experimental reactor used during this collaboration. This reactor consists of an upper cylindrical source chamber and a lower spherical diffusion chamber. The plasma, a helicon plasma operated exclusively in the capacitive mode [76], is ignited by a Huttinger PFG 1600 radio-frequency generator followed by a Huttinger matchbox connected to a Boswell antenna. A feed gas of either hydrogen, or deuterium, was used throughout the core experiments on this device. However, admixtures of argon and oxygen were also used to clean the chamber at regular intervals.

The pressure of the diffusion chamber is measured by a MKS Baratron gauge, and is regulated by a Brooks 5850 20 sccm mass flow controller. A 150 mm inner diameter Riber gate valve, installed just before the entrance to the turbo molecular pump, was adjusted accordingly in order to maintain the desired pressure.

3.5.2 Electron Cyclotron Resonance Plasma

An electron cyclotron resonance (ECR) plasma was briefly used for some of the measurements presented within Chapter 5. The ECR source (Boreal Plasmas) was set to a frequency of 2.45 GHz for the magnetic field of 845 Gauss; this is considerably larger than the ion plasma frequency. The MPG-4 Opthos Instruments Inc. generator was coupled with a home-made matching network, and the reflected power was minimised by tuning the position of two impedance matchers located within the ECR source itself. This ECR has been characterised, and discussed, in much greater detail in the referenced PhD thesis [77].

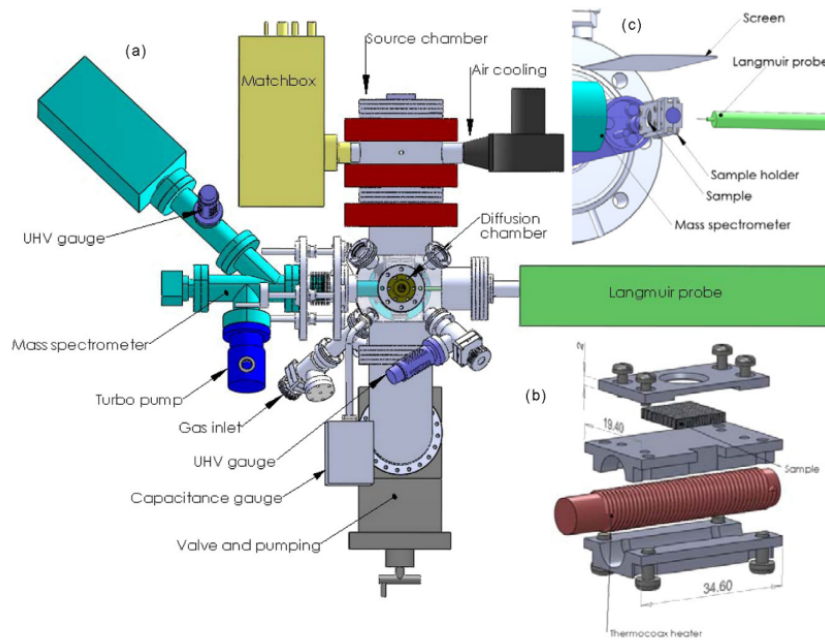


Figure 3.4: A schematic representation of the experimental reactor (a), sample holder (b), and a zoomed in view of the sample and aperture of the mass spectrometer (c).

3.5.3 Sample Holder

Figure 3.4 (b) shows a schematic representation of the used sample holder. The sample holder is connected via the frame to a Equipment Scientific Alimentation de Laboratoire CN7C DC voltage source. The voltage applied to the frame V_{DC} is not equal to the voltage at the surface of the sample V_S . The difference in this voltage was calibrated through the use of a multimeter prior to the installation of the sample holder. A tungsten heating element was positioned behind the sample, which allowed simultaneous heating and biasing of the sample. The temperature was measured by a K-type thermocouple located within the frame of the sample holder, and was calibrated externally to the chamber by measuring the temperature of the sample. An AXESS tech. proportional-integral-derivative (PID) controller was used to regulate the temperature of the installed samples.

The samples installed were approximately 1 mm thick with a surface area of 1 cm², with only one face exposed to the plasma. The sample holder was connected via a load-lock system, which allowed the samples to be changed without breaking the vacuum in the diffusion chamber.

3.5.4 EQP Mass Spectrometry

The sample holder was installed within the lower spherical diffusion chamber, positioned such that the samples were normal to the aperture of an electrostatic quadrupole plasma mass spectrometer (Hiden, EQP 300). The separation between the sample and the mass spectrometer was measured to be 37 mm, which was the closest possible distance. Previous studies have demonstrated that the separation of the sample and the aperture has a negligible effect on the measured negative ion energy distribution functions (NIEDFs) [78].

Figure 3.4 (c) shows a zoomed in schematic view of the sample and the mass spectrometer's aperture. The aperture of the mass spectrometer has a diameter of 0.1 mm, which is located behind a 5 mm gap in the outer grounded shield of the mass spectrometer's chassis. An additional grounded screen, shown by Figure 3.4 (c), is installed 50 mm above the sample and the mass spectrometer to reduce the RF fluctuations. The aperture of the mass spectrometer can be polarised, and has been calibrated so that a near planar plasma sheath is formed [79].

A complete explanation of how EQP mass spectrometry works would be beyond the scope of this work, however, at least a basic understanding is required in order to understand how a measurement is acquired. The mass spectrometer consists of four key components which must be considered, these are shown pictorially in Figure 3.5. The first key component is the internal ioniser, however, mass spectrometry was used within this work to measure charged species, primarily negative ions, which means that the internal ioniser was not used. Immediately after the internal ioniser is an ion flight tube, this allows the mass spectrometer to be inserted within the plasma to different lengths. However, in all the experiments conducted within this work the insertion length was kept constant. The second key component is an energy analyser which creates an electric field such that only ions of a specific energy are transmitted. The resolution of the energy analyser used within this work is approximately 0.25 eV FWHM; the resolution was supplied by the manufacturer. The third key component is the quadrupole mass filter which consists of four parallel rods arranged around a central axis, as depicted by Figure 3.5. The potential applied to these rods is a combination of a DC offset and a time-varying RF potential. Each pair of rods consists of one rod with a positive phase, and the other negative. This allows the creation of a fluctuating electric field that can be controlled by altering the voltages applied to each rod; this selectively allow a single mass to charge ratio ion to travel through the central axis. The

other ions' trajectories will be destabilised and the ions will be lost through collisions with the rods. The final key component to consider is the detector which consists of a series of dynodes. Upon the collision of an ion with a dynode, a secondary electron is emitted, which in turn strikes an additional dynode that produces more secondary electrons. These electrons are then measured which results in the counts being outputted by the mass spectrometer.

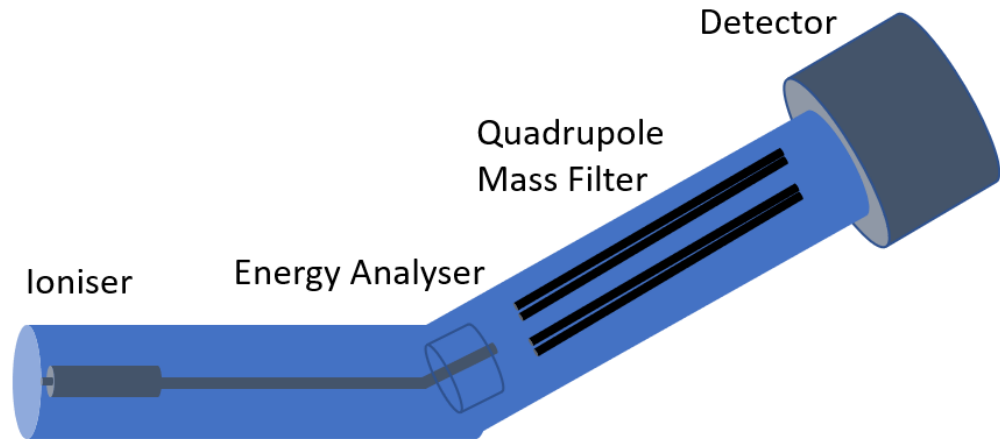


Figure 3.5: A schematic representation of the EQP mass spectrometer. Labelled are the internal ioniser, energy analyser, Quadrupole mass filter, and detector.

3.5.5 Negative Ion Extraction

Figure 3.6 shows the electrical potential profile between the target sample and the aperture of the EQP mass spectrometer. The aperture is grounded, and the sample is negatively biased. This bias can be varied between -20 and -130 V depending on the experimental conditions. Once the plasma is ignited, there is a potential drop between the plasma potential V_p and the surface bias. Positive ions are accelerated through this potential drop across the sheath, and subsequently impinge onto the target's surface. The positive ions, in the case of a hydrogen or deuterium plasma, are primarily molecular ions, and are assumed to dissociate during impact with the surface. The majority of these ions are adsorbed onto the surface of the target, but some will be reflected by the surface. However, due to the electrical potential profile, very few will reach the core plasma. Neutral species are able to diffuse off the surface and enter the core plasma, as they are unaffected by the potential profile. The negative ions that will be produced, either through backscattering or sputtering, will be accelerated through the potential drop by $e(V_p - V_s)$. These accelerated negative ions will reach the

sheath region in front of the grounded mass spectrometer aperture, and are decelerated by eV_p , resulting in a total energy gain of $-eV_s$.

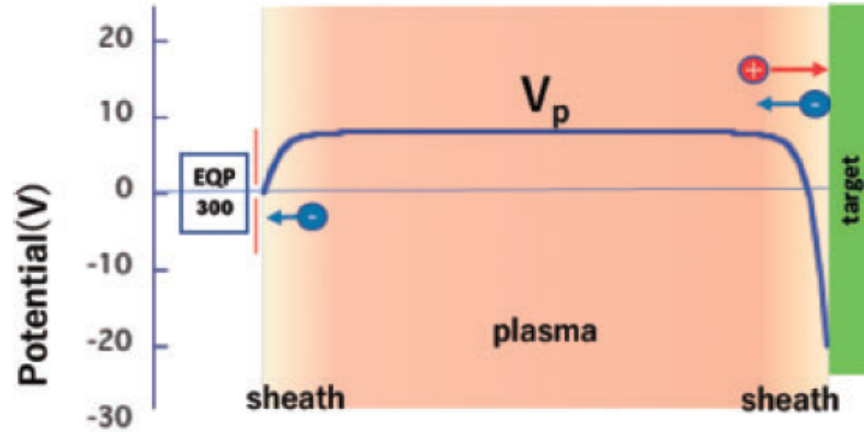


Figure 3.6: Electrical potential profile between the sample and the aperture of the EQP mass spectrometer. The aperture of the mass spectrometer is grounded, and $V_s = -20$ V. Copyright (2018) The Japan Society of Applied Physics [1].

3.5.6 Experimental Procedure

In order to acquire NIEDFs, the following experimental procedure was performed. Firstly, the plasma was brought to a steady state by measuring the positive ion distribution, H^+ , H_2^+ , and H_3^+ . This was then checked against the previously measured molecular ion distribution to ensure that the same ratios were obtained. The time taken to reach steady state depends on a number of possible factors including: the plasma source, the temperature of the chamber walls, and degassing of the installed surface. Following this, a DC bias was applied to the sample, this allowed negative ions to be produced due to the positive ion bombardment. The negative ions were then measured by the EQP mass spectrometer; the number of counts was monitored as a function of time to ensure that measurements only took place once an equilibrium had been reached.

3.6 Two Photon Absorption Laser Induced Fluorescence — TALIF

TALIF was used within this work to measure the atomic hydrogen density at approximately 1 cm above different metallic surfaces for Chapter 6 — *Influence of the surface material upon the atomic hydrogen densities*. This section gives a detailed explanation of the diagnostic and relevant background theory.

3.6.1 Introduction to TALIF

Before an explanation of two photon absorption laser induced fluorescence (TALIF) can be presented, it is important to understand its predecessor, laser induced fluorescence (LIF) [80]. LIF is an active and indirect diagnostic that allows for spatially resolved measurements of the ground state densities [81]. Whilst LIF is an absorption technique, the methodology allows for spatial resolution and has been used to measure radical species such as CF, CF₂ [82], SiH₂ [83], and hydroxyl radicals [84, 85].

A photon impinging on a ground state species can facilitate a transition into a higher energy level. This excited state can subsequently relax into a lower energy level, releasing a photon in the process, hereafter referred to as a fluorescence photon. These photons originate in the overlap region between the laser and the plasma, and upon their detection, the ground state density can be calculated. Fluorescence photons are released isotropically, which allows for spatial resolution when using LIF/TALIF, whereas classical absorption spectroscopy is inherently line integrated and cannot provide spatial information.

Whilst this method is well established for molecular species [81, 86], it is not easily applicable for atomic species. The energy gap between the ground state and the first excited state for atomic species is large enough that the required photons would be in the vacuum ultraviolet (VUV) portion of the electromagnetic spectrum. An appropriate lasing medium is required in order to generate photons of this wavelength (<194 nm), and such mediums are uncommon.

Excimer lasers [87] or non-linear optical manipulation of higher wavelengths would allow VUV photons to be produced, however, due to the absorption of the VUV photons by atmospheric species, a continuous vacuum would be required. TALIF circumnavigates these problems by using two photons, with each photon providing half the energy required for

the transition. Photon energy and wavelength are intrinsically linked, therefore halving the energy requirement doubles the wavelength. Consequently, the photons are no longer part of the VUV spectrum. Whilst the generation of photons is no longer a limiting factor, the probability of two photons being absorbed by the species of interest is far lower than that of a single photon. Higher intensity lasers are therefore required to compensate for this. Nevertheless, even with the technical difficulties that TALIF presents, it has been used to successfully measure species such as atomic oxygen [88–90], atomic hydrogen [91–93], and atomic nitrogen [94, 95].

3.6.2 Excitation

3.6.2.1 Optical Selection Rules

Before the topic of excitation can be considered, it is important to understand which excited states can be populated and depopulated due to optical selection rules. Optical selection rules determine the *allowed* and *forbidden* transitions; it is worth noting that the *forbidden* transitions can still take place, but with a much smaller probability. Whilst TALIF is a two-photon process, the excitation can be considered as a single photon exciting the ground state into an intermediate ‘virtual’ level, and then a second transition from this ‘virtual’ level into the excited state. This has the important consequence that TALIF’s excitation is governed by single photon selection rules. The first of these is that parity (π) should not change:

$$\pi = -1^l \quad (3.9)$$

Where l is the angular momentum quantum number, determined by the orbital structure, $l_s = 0$, $l_p = 1$, $l_d = 2$, etc.... The second selection rule that must be obeyed is related to the total angular momentum quantum number J . Single photon selection rules mandate that $J \rightarrow J/J \pm 1$, however, for two photon interactions, $J \rightarrow J \pm 2$ is also a valid transition.

An example of these rules can be seen from the excitation of atomic hydrogen. Whilst the transitions from the $1s$ state to the $3s$ and $3d$ states are allowed – the parity is unchanged in these transitions – the population of the $3p$ state is forbidden. The $3p$ state can become populated under certain conditions due to a phenomenon known as L-state mixing [93].

3.6.2.2 Ground State Excitation

The following sections outline the theory surrounding TALIF; a full treatment has been completed by Goehlich *et al.* [96]. In order for the fluorescence photons to be generated, the species needs to be excited from the ground state into an excited state. Subsequently, the relaxation into a lower energy level releases the fluorescence photon. Equation 3.10 shows the rate of the transition between the ground state E_1 and E_2 :

$$R(t) = G^{(2)}\sigma^{(2)}g(\nu)\left(\frac{I_0}{h\nu}\right)^2 \quad (3.10)$$

Here, the superscript ⁽²⁾ is used throughout to distinguish a two photon process. The rate of excitation is proportional to the square of the photon flux, as two photons need to be absorbed in order to facilitate the transition. $G^{(2)}$ is the photon statistic factor, which is the probability of the two photons matching the transition between the ground state and the excited state. This value is equal to 2, larger than that of conventional LIF, due to the increased probability of off-resonance photons matching the transition energy [92]. The two photon excitation cross-section, $\sigma^{(2)}$, is the probability of two photons interacting with the ground state in order to facilitate the transition. This is far smaller than the corresponding cross-section in LIF, as two photons are needed for the transition. The value is not found analytically due to the complex quantum mechanical models required, therefore, empirical values are used.

The normalised line profile as a function of frequency is defined as $g(\nu)$, which is a convolution of the natural line profile of the transition and the laser spectral profile. The natural line profile of the transition is pressure broadened due to collisions and Doppler broadened, unless Doppler-free TALIF methods are utilised. The normalised line profile is a Voigt distribution, which is a convolution of Gaussian and Lorentzian distributions. Both the natural line profile of the transition and the pressure broadening are described by Lorentzian distributions, whereas, the Doppler broadening and the laser spectral profile are Gaussian distributions. The photon flux is described as the laser intensity I_0 divided by the photon energy $h\nu$; this is squared as two photons are required to make the transition.

By using Equation 3.10, the rate of change of the ground state density can now be defined; this is shown by Equation 3.11:

$$\frac{d}{dt}n_1(t) = -R(t)n_1(t) \quad (3.11)$$

The rate of change of the the ground state density is negative due to its use in populating the first excited state. The one-photon transition from the excited state, E_2 , back to the ground state, E_1 , is, in contrast to LIF, spectrally forbidden. Here, it is assumed that the ground state density is large and remains constant such that $n_1(t) \approx n_0$. The population rate for the excited state E_2 can now be expressed with respect to the ground state density:

$$\frac{d}{dt}n_2(t) = R(t)n_1(t) - An_2(t) \quad (3.12)$$

The first term on the right hand side of this equation describes the population of E_2 from the ground state. The second term describes the depopulation of E_2 through loss mechanisms.

Figure 3.7 shows a schematic representation of the various processes taking place, including the excitation from E_1 to E_2 and various loss mechanisms, which will be discussed in detail in the next section.

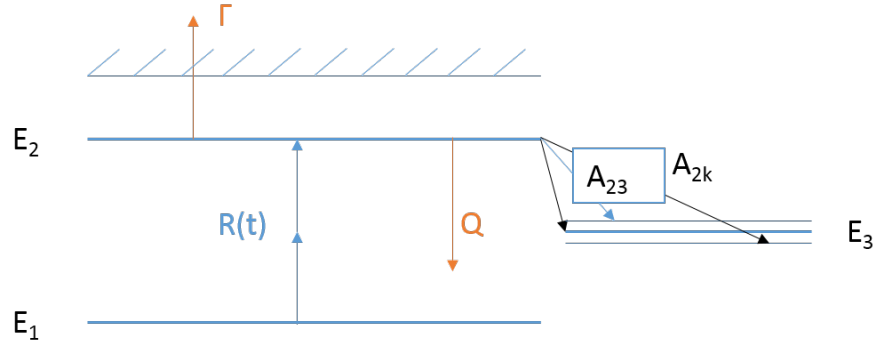


Figure 3.7: A schematic representation using a three level energy diagram, showing various loss mechanisms, including: Quenching (Q), Photo-ionisation (Γ), radiative decay (A_{2k}), and the excitation mechanism from the ground state E_1 .

3.6.3 Loss Mechanisms

3.6.3.1 De-excitation

The emission from the excited state E_2 to E_3 is the natural place to start as these fluorescence photons can be measured. Should the state E_2 only decay in this manner, then measuring

the density of the excited state would be relatively straight forward. However, the excited state E_2 can decay into numerous states; this can be defined by Equation 3.13:

$$A_2 = \sum_k A_{2k} \quad (3.13)$$

Equation 3.13 gives the total decay from excited state E_2 into all possible lower states k , where A_2 represents the rate of decay from the state E_2 . The inverse of this would yield the natural life time of the upper state E_2 , defined by $\tau = \frac{1}{A_2}$.

3.6.3.2 Quenching

Photons are only released during the process of radiative decay, however, energy can also be released during non-radiative processes, for example via collisions. The excited state of the species of interest may collide with another species within the plasma. Collisions reduce the population of the excited state E_2 without the emission of a fluorescence photon. If quenching is not taken into account then the density of E_2 will be underestimated, as the observer will measure a weaker fluorescence signal.

This phenomenon now must be included in the generalised effective loss rate A , such that $A = A_2 + Q$, where Q represents the loss due to collisional quenching channels. Depending on the plasma in question multiple species may be able to quench the excited state; the probability of this happening depends on the quenching species. The quenching rate is given by the product of $n_q k_q$, with n_q representing the quenching species density, and k_q the quenching coefficient, or rather, how probable it is that quenching will occur. The summation of all possible quenching channels must be accounted for in order to properly account for the total contribution of quenching.

$$Q = \sum_q n_q k_q \quad (3.14)$$

3.6.3.3 Ionisation

Photoionisation is another effect that must be considered in order to account for the total depopulation of the excited state E_2 . This process occurs when a third photon is absorbed by the excited state E_2 . Ionisation from the excited state E_2 results in a decrease of n_2 without the emission of a fluorescence photon. Therefore, this process must be included in

the effective loss rate, as defined by Equation 3.15:

$$A = A_2 + Q + \Gamma \quad (3.15)$$

Photoionisation of the excited state E_2 can be avoided providing that the laser energy is kept sufficiently low; which allows for the assumption that $\Gamma = 0$. This enables the effective loss rate equation to be simplified:

$$A = A_2 + Q \quad (3.16)$$

3.6.4 Detection

A reworking of the loss parameters can prove useful for drawing all of the physics together. Assuming, as previously stated, that we are operating in a regime with negligible ionisation, then we can combine our loss terms together into the reduced optical branching ratio a_{23} as shown by Equation 3.17.

$$a_{23} = \frac{A_{23}}{A_2 + Q} \quad (3.17)$$

If the effect of quenching (Q) was negligible, Equation 3.17 would simplify to: $a_{23} = \frac{A_{23}}{A_2}$. This is simply the ratio of E_2 decaying into the fluorescence channel divided by all other possible radiative decays.

It is now almost possible to draw all the elements of the excitation and loss mechanisms together under one equation. Firstly, the detection of the fluorescence photons must be considered. The signal measured (S) will be attenuated by various factors, such as, the sensitivity of the detector for a given wavelength ($\eta(\nu)$) and the transmission through the optics (T(ν)). The fluorescence photons are emitted isotropically, therefore, the solid angle of the detector ($\Delta\Omega$) needs to be taken into consideration.

$$S = \eta T \frac{\Delta\Omega}{4\pi} n_{h\nu} \quad (3.18)$$

It is now important to consider the $n_{h\nu}$ factor in this equation. This is simply the number of fluorescent photons produced, which is a product of the density of the excited state n_2 and the optical branching ratio a_{23} .

$$S = \eta T \frac{\Delta\Omega}{4\pi} a_{23} n_2 \quad (3.19)$$

This can be simplified further via integrating Equation 3.12 with respect to the total fluorescence time and space between 0 and ∞ . This results in the detected signal as follows:

$$S = \eta T \frac{\Delta\Omega}{4\pi} a_{23} R(t) n_1 \quad (3.20)$$

Now using Equation 3.10, the full form of this equation can be written as follows:

$$S = \eta T \frac{\Delta\Omega}{4\pi} a_{23} n_1 G^{(2)} \sigma^{(2)} g(\nu) \left(\frac{E}{h\nu}\right)^2 \quad (3.21)$$

This can then be rearranged as required to give information about the ground state density n_1 :

$$n_1 = \frac{4\pi S}{\eta T \Delta\Omega a_{23} G^{(2)} \sigma^{(2)} g(\nu)} \left(\frac{h\nu}{E}\right)^2 \quad (3.22)$$

Whilst the above equation can in theory be used to directly calculate the ground state atomic densities of species, it requires specific information about the normalised laser profile and the spatio-temporal characteristic of the laser pulse. In order to circumnavigate this problem, a calibration must be used in order to obtain absolute atomic densities.

3.6.5 Calibration

In order to ascertain an absolute measurement of the atomic ground state density, one option is to normalise the fluorescence signal (S) against a known concentration of the species of interest. For atomic species such as O and H, this is experimentally challenging due to the preference for these species to exist in their molecular states. One way that this can be achieved is by the use of a flow tube reactor [97] in which the atomic species are generated via microwave excitation. However, not all experiments can facilitate a flow tube. A full treatment of the difficulties with using this calibration technique has been conducted by Niemi *et. al.* [98].

Goehlich *et. al.* provided a more convenient solution for calibrating the TALIF signal by using a noble gas as a reference [96]. The noble gases provide a stable source of atoms that importantly have a similar excitation scheme to the species of interest. This allows for the

setup to be similar between both the calibration and the original experiment. In particular, the laser's spatial, spectral, and temporal profiles will be shared, which bypasses the need for specific information for these parameters. Figure 3.8 shows the excitation scheme for hydrogen, or nitrogen, calibrated with respect to krypton.

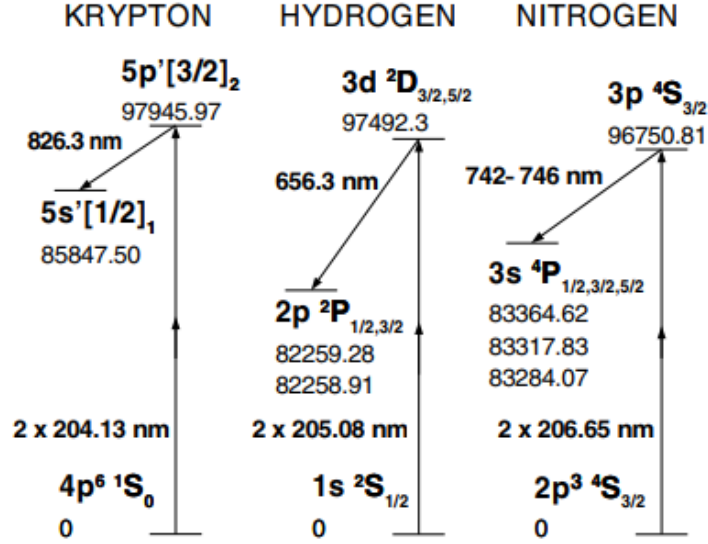


Figure 3.8: TALIF excitation scheme for atomic hydrogen, and nitrogen, with respect to krypton [92].

Calibration using noble gases requires the ratio of the TALIF signal between the species of interest (X) and the reference species (R). Equation 3.23 shows the full rearranged form of this equation with the subscript X and R being used to distinguish between the species of interest and the reference species respectively. The photon flux has been rewritten in terms of wavelengths (λ) as opposed to frequency (ν).

$$\frac{S_X}{S_R} = \frac{\eta_X}{\eta_R} \frac{T_X}{T_R} \frac{a_{23X}}{a_{23R}} \left(\frac{E_X}{E_R}\right)^2 \left(\frac{\lambda_X}{\lambda_R}\right)^2 \frac{\sigma_X^{(2)}}{\sigma_R^{(2)}} \frac{n_X}{n_R} \quad (3.23)$$

This can be rearranged trivially to find an expression for the absolute atomic densities of the species of interest n_X .

$$n_X = \frac{S_X}{S_R} \frac{\eta_R}{\eta_X} \frac{T_R}{T_X} \frac{a_{23R}}{a_{23X}} \left(\frac{E_R}{E_X}\right)^2 \left(\frac{\lambda_R}{\lambda_X}\right)^2 \frac{\sigma_R^{(2)}}{\sigma_X^{(2)}} n_R \quad (3.24)$$

This can be further simplified by considering how each of these terms are obtained. The ratio of the fluorescent signals are obtained experimentally. The sensitivity of the detection

optics, ν , and the transmission of the optics, T , are known values. The reduced optical branching ratios, a_{23} , are either known from the natural radiative decay rates or can be found experimentally by measuring the effective decay rates; this can be completed by measuring the fluorescence signal as a function of time, for more information please refer to section 3.6.8 *Effective Lifetime Measurements*. The laser pulse energy is known, furthermore, with careful consideration of the excitation schemes used, Figure 3.8, then only the laser energy is required. The ratio of the wavelengths are known and the two-photon excitation cross-sections can be found in literature. Ultimately, all the terms can be separated into two coefficients representing the invariant parameters and the effective decay rates; these are represented by C and A respectively.

$$C = \frac{\eta_R}{\eta_X} \frac{T_R}{T_X} \left(\frac{\lambda_R}{\lambda_X} \right)^2 \frac{\sigma_R^{(2)}}{\sigma_X^{(2)}} \left(\frac{E_R}{E_X} \right)^2 \quad (3.25)$$

The equation can now be rewritten in considerably simpler terms:

$$n_x = C \frac{S_X}{S_R} \frac{A_R}{A_X} n_R \quad (3.26)$$

3.6.6 Experimental Procedure

3.6.6.1 Beam Line

The laser system used for all the TALIF measurements is a Continuum Surelite SL-EX Nd:YAG, coupled with a Continuum Horizon optical parametric oscillator (OPO). This system is capable of lasing with a wavelength range of 192–2750 nm and with a pulse width of 3–5 ns depending on the wavelength of operation; the laser is pulsed at a frequency of 10 Hz.

Figure 3.9 shows the external beam line used for all the TALIF measurements presented within this thesis. Two different beam paths are outlined in order to allow measurements of both atomic hydrogen (red) and atomic oxygen (blue). However, only atomic hydrogen densities are presented within this work. Immediately before the beam enters the GEC reference cell, there is an iris which acts to reduce the beam waist and a focussing lens. The focal point of the beam is located in the centre of the GEC reference cell, approximately 1 cm above the grounded electrode. The beam is terminated on the far side of the GEC reference cell into a beam dump.

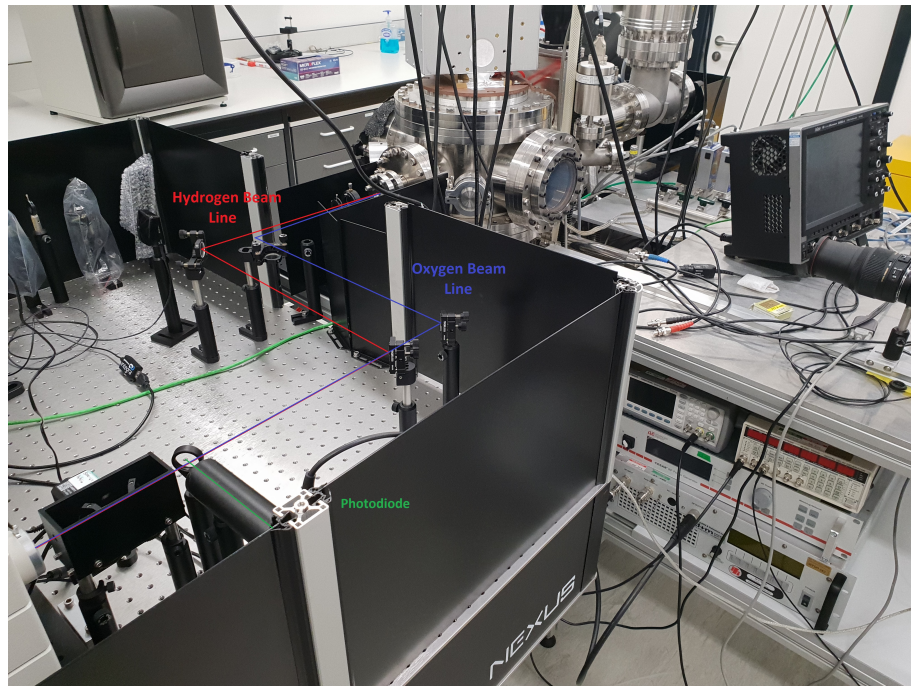


Figure 3.9: Annotated beam line for the TALIF measurements

3.6.6.2 Attenuation Scheme

Immediately after the beam exits the aperture of the OPO unit, it enters an attenuation scheme. The beam is attenuated in order to maintain a consistent pulse energy throughout an experiment. The attenuator consists of two windows that are designed to operate at a specific wavelength, corresponding to the output of the laser. The first window is coated with an angle dependant dielectric that acts to reduce the beam energy, unless positioned normal to the incident beam. The second window acts to moderate the spatial displacement of the beam caused by the transmission through the first window, therefore, the windows must be positioned at congruent opposite angles. The position of these windows was controlled using a Zaber T-NM17A04 stepper motor.

Directly following the second window, the beam encounters a beam splitter. Part of the laser beam is directed into a Thorlabs DET 10A/M photo-diode; there are diffusers located before the photo-diode to ensure the impinging energy is within tolerance. The photo-diode outputs to a LeCroy WaveSurfer 104MXs-B 1 GHz 10 GS/s oscilloscope that records the peak to peak voltage in mV; the oscilloscope is in turn connected to the laptop. A proportional–integral–derivative controller (PID) is used to control the position of the two mirrors simultaneously, in order to achieve the desired attenuated signal.

This attenuation scheme allows for the laser energy to be controlled, which is important in order to enable saturation curves to be plotted. The energy was measured by using a Gentec QE25LP-S-MB energy meter. These curves are necessary in order to determine the maximum possible laser energy without causing significant photoionisation events. Figure 3.10 shows an example of a saturation curve for Krypton at a gas pressure of 30 Pa. A deviation from a linear trend can be observed at approximately 200 μJ . Due to this, all calibration experiments were operated at a pulse energy of 180 μJ . The same procedure was conducted in order to determine the pulse energy for operating with hydrogen. Saturation was observed to occur at 800 μJ , therefore, the pulse energy was chosen to be 780 μJ for the hydrogen measurements.

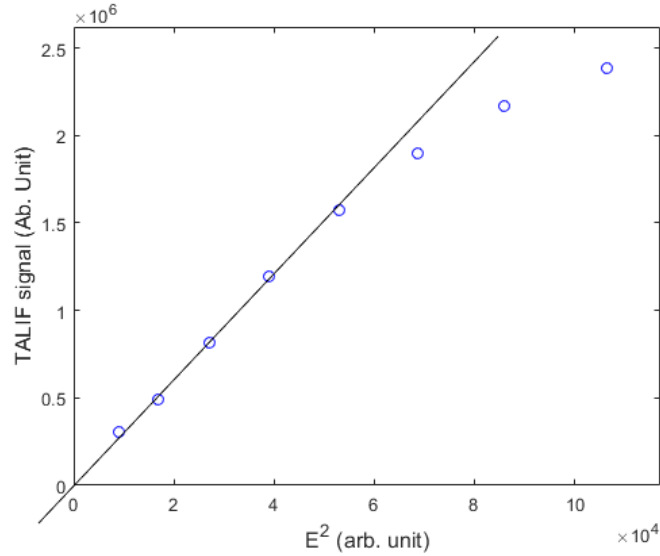


Figure 3.10: Saturation curve for Krypton at a gas pressure of 30 Pa. The deviation from a linear relationship can be observed at approximately 200 μJ . The laser energy was therefore selected to be 180 μJ , in order to not cause photoionisation events.

3.6.7 Detection Scheme

The fluorescence signal is measured normal to the beam line by using an Andor iStar DH344T-18U-73 ICCD camera. A focussing lens is used in order to directly observe the overlap region of the focussed laser beam and the plasma. In order to provide sensitivity to the desired fluorescence wavelength, an interference filter is fitted directly onto the ICCD camera. The interference filters used are 656 nm (hydrogen α Balmer), and 825 nm, for hydrogen and krypton respectively. The bandwidths of these filters are approximately 10

nm. The wavelength dependency of the interference filters' transmission was provided by the manufacturer (Thorlabs).

The output of the laser acts as the master trigger for the synchronisation of the laser pulse and camera acquisition. The TTL output of the lasers Q-switch is connected to a Stanford Research Systems DG 645 digital delay generator (DDG). The DDG inserts an appropriate delay before externally triggering the camera. Figure 3.11 gives an example of the images that are acquired by the camera of the laser fluorescence against the background emission of the plasma. The central box shows the region of interest, 210–270 x-pixels, 180–195 y-pixels, that is used for the data analysis; this is discussed in more detail in the next sections.

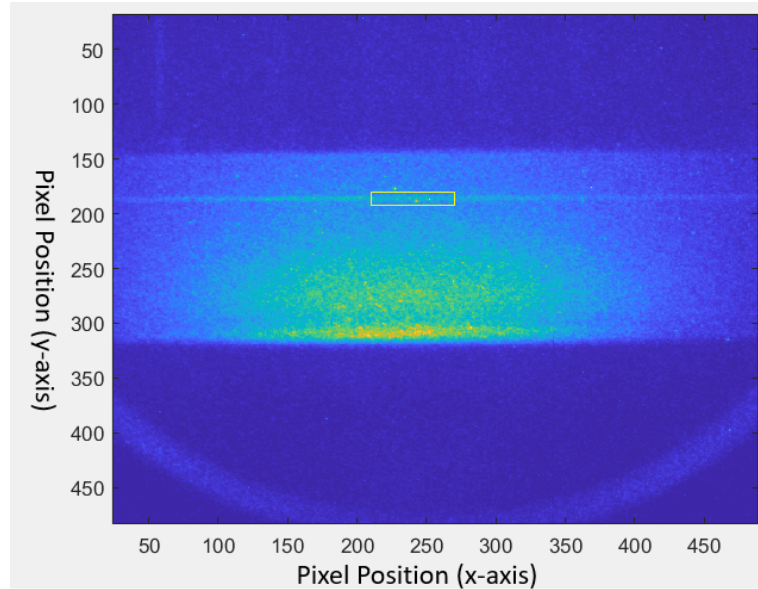


Figure 3.11: An example of the laser fluorescence against the background emission of a 25 Pa hydrogen plasma, operated at an applied power of 700 W. The region of interest used for the data analysis was between 210–270 and 180–195 pixels in the x and y-positions respectively.

3.6.8 Effective Lifetime Measurements

Whilst it is possible to perform TALIF measurements using quenching coefficients from literature, this introduces a significant error into the final absolute density measurements. In order to reduce these errors, the effective lifetimes were measured. The inverse of the effective lifetime yields the effective decay rates (A_X), which are required when calculating the absolute atomic densities.

The effective lifetimes are calculated by measuring the time evolution of the fluorescence signal after the incidence of the laser pulse. These experiments are conducted by using a

short gate width (the minimum gate width is 3.6 ns) on the camera and averaging over 256 laser pulses (determined by the length of exposure), in order to minimise the effects of the fluctuations in the laser pulse energy. After one measurement has been completed, the delay between the laser pulse and camera acquisition is increased by 2 ns. This is then repeated for 25 data points (50 ns). Finally, an exponential decay can be fitted to these data points that allows the effective lifetime, or decay rate, to be calculated. These measurements are conducted for both hydrogen and krypton, allowing the ratio of the effective decay rates to be calculated, as required by Equation 3.26. An example of this exponential fit is given within Figure 3.12.

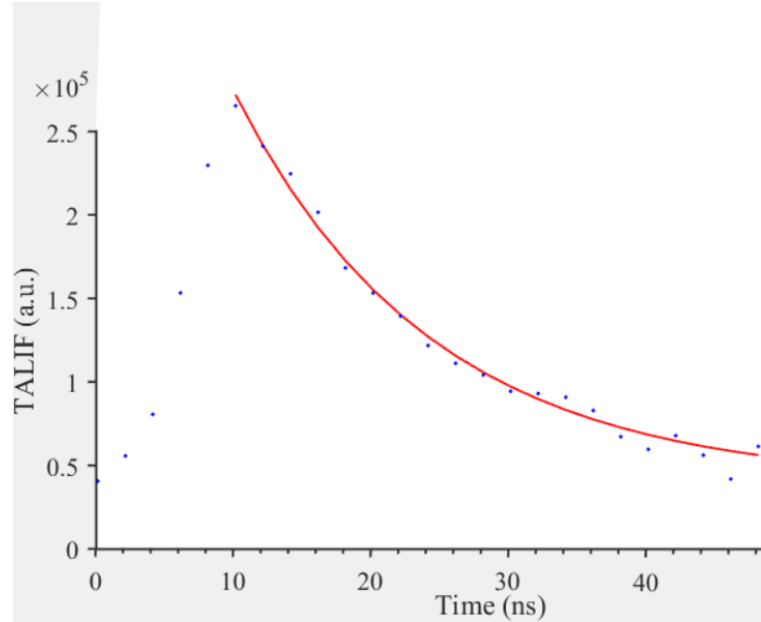


Figure 3.12: An example of an exponential fit that allows the effective decay rate to be calculated. The TALIF signal in this instance, represented by the y-axis, is the fluorescence count by the ICCD camera for a single peak wavelength.

3.6.9 Total Fluorescence Signal

In order to capture the total fluorescence signal (S_X), caused by the overlap of the laser focus and the plasma, a longer gate width is required. A gate width of 200 ns was used for all the measurements conducted within this thesis; this was chosen as larger temporal integrations were observed to cause no increase in S_X . S_X is also spectrally dependent, and therefore a wavelength scan must be performed. The wavelength was scanned in 0.01 nm increments, the minimum possible wavelength step, in order to find the spectral dependence. These temporal

and spectral integrations of the fluorescence signal were conducted for both hydrogen and krypton to allow an accurate ratio of the total fluorescence signals to be calculated. The fluorescence signals, as a function of the wavelength, were plotted, as shown by Figure 3.13; a Gaussian distribution was then fitted. The total fluorescence signal S_X is defined as the area of this distribution.

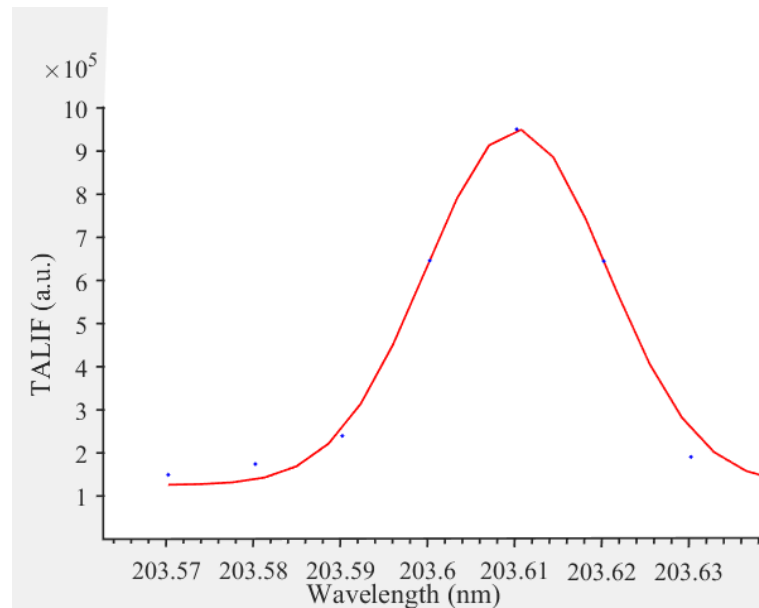


Figure 3.13: An example of the Gaussian fitting for the spectral integration, wavelength scan, measurement. The area under the Gaussian distribution is defined as the total fluorescence signal.

3.6.10 Error Analysis

There are two different ways in which the errors for TALIF can be estimated. Firstly, the systematic errors can be considered, which will have an impact on the absolute densities calculated. Secondly, there are the stochastic errors, which will affect the relative measurements.

In relation to the systematic errors, each element of Equation 3.24 must be considered, and the associated error discussed. Firstly, the quantum efficiency of the iCCD camera must be examined. Unfortunately, the manufacturer has not provided an error for this quantity, therefore an estimated error of $\pm 10\%$ has been used. The ratio of the transmission through the focussing lens, for hydrogen and krypton, is almost identical, and as such can be largely ignored. The error in the transmission through the interference filters is 1% . Assuming no

quenching, the reduced optical branching ratio can be simplified to the optical branching ratio, which only has a small associated error. However, the measurements for the natural lifetimes have a reasonably significant error, averaging to be 8 % [98]. The largest error in the TALIF measurements is due to the two-photon cross-section, this is found empirically, and for some species, no estimate exists. The error associated with the two-photon cross-sections ratio for hydrogen and krypton is 50 % [92]. When these errors are taken in quadrature, a total error estimation of ± 52 % is calculated.

Whilst the systematic errors are large, this is only a problem when directly comparing absolute densities to other diagnostic/computational methods. Relative measurements are only affected by the stochastic errors. The first stochastic error to consider are the effective lifetime measurements which are measured to a 95 % confidence interval; the associated errors with these measurements are estimated to be ± 5 %. The error in the laser energy is assumed to be 6 %, as this is the maximum standard deviation of the shot-to-shot pulse energy observed during the experiments. Finally, there is the error in the total fluorescence signal. The number of points used to calculate the Gaussian distribution is limited by the wavelength step of the laser (0.01 nm). The 95 % confidence interval, that was used for Figure 3.13, reveals only a small difference (< 2 %) in the total signal. Nevertheless, the small number of points can lead to a problem of an artificially good fit. Therefore, the error is generously estimated to be 6 %. When taken in quadrature, a total of ± 12 % is assumed for the error in the relative densities.

3.7 Confocal Microscopy

Confocal microscopy is presented within this thesis as a confirmation of the crystalline faces of various nitrogen doped diamond samples. This diagnostic was not completed by the author, but by the company which supplied the samples. Nevertheless, it is prudent to provide a brief explanation of how the diagnostic works and provide references for further reading for those who are interested.

Confocal microscopy uses a laser to generate the fluorescence that is subsequently observed by a CCD detector. A pinhole is used to isolate only the fluorescence from the desired focal plane. This is in contrast to classical fluorescence microscopy that suffers from blurred images caused by the fluorescence before and after the focal plane. By adjusting the posi-

tions of the mirrors that reflect the laser light onto a sample, a spatial scan of the sample can be obtained. This spatial profile of fluorescence signals can be combined together post acquisition in order to generate the two-dimensional images. This same technique can be used to generate three-dimensional images by adjusting the focal plane and repeating the spatial scans. This technique is common in both material science and biology. An overview of the technique by Tata *et. al.* [99] gives a great introduction for how the diagnostic is utilised in material science. Finally, a more direct example on analysing plasma assisted diamond growth has been published by Gu *et. al.* [100].

Chapter 4

Influence of the surface material on the volume production of negative hydrogen ions

4.1 Prelude

This chapter presents absolute H^- ion density measurements within the GEC reference cell across a wide range of pressures and powers for multiple grounded electrode materials, including: tungsten, stainless steel 304, copper, aluminium, and molybdenum. These measurements were conducted using laser photodetachment, as described in Section 3.3. A hydrogen plasma was driven at 13.56 MHz by a power generator, connected through an automatic matching network, coupled onto a 5-turn copper coil. This generation apparatus was used in tandem with a digital delay generator in order to produce a pulsed plasma with a repetition rate of 10 Hz and a duty cycle of 10%. Here, it is worth noting the usage of the word *power* throughout this section, both within the text and on the figures. The quoted value for the power is the forward power supplied by the generator, in all instances this is matched using a matching network to reduce the reflected power to zero. This forward power is the power that would be supplied if the plasma was run in a continuous operation, however, when pulsed this is no longer an accurate representation of the applied power. Unfortunately, due to the connection between the generator, matching network, and 5-turn copper coil there was no possibility to make an accurate power measurement. Hence, these values should not

be taken as a definitive quantified value. Nevertheless, if a comparison is desired this can be estimated by considering the measured electron densities in both systems.

The temperature of the grounded electrode was cooled through the use of water cooling channels beneath the surface. However, because the thermal conductivity between the installed samples and the electrode was poor, the plasma had to be pulsed. This significantly reduced the thermal loading upon the sample, which was confirmed through the use of an IR thermal sensor. A feed gas of hydrogen (99.9995 %) was used throughout these experiments, with the pressure controlled through the use of a butterfly valve and mass flow controllers.

All of the measurements presented within this chapter were conducted within the GEC reference cell which was coupled inductively. However, the power was kept below the threshold for the E-H transition; the transition to H-mode occurred at powers of 800 W and greater. This was chosen for three distinct reasons. Firstly, the additional thermal loading upon the transition to H-mode was difficult to control and thermal effects were noted to cause significant changes in the measured H^- ion density. Secondly, the capacitors tasked with filtering the radio-frequency signal inside the shaft of the Langmuir probe were significantly affected by the additional thermal load on the probe tip. Finally, the instance of the E-H mode transition was not consistent between pulses. This observation was made through using a photomultiplier tube connected to an oscilloscope; the transition to the H-mode regime was distinctive due to a large voltage spike.

In general, metallic surfaces, such as molybdenum, are frequently used as a base to evaporate caesium upon in order to produce a large quantity of H^- ions. The motivation for this chapter was therefore to investigate whether different metallic samples had a significant influence on the volume production of H^- ions. The H^- ion measurements show that the surfaces appear to fall into one of two distinct categories. The first of these consists of tungsten and stainless steel 304, which exhibit similar qualitative and quantitative trends. The other category, comprising of copper, aluminium, and molybdenum, also exhibit similar quantitative and qualitative trends to one another. All of the data for stainless steel, aluminium, and copper was acquired and processed by the author. Equally, the 25 Pa experiments for tungsten and molybdenum were also acquired by the author. However, the 17 and 37.5 Pa measurements for tungsten were acquired by J. Branson, but were interpreted by the author.

4.2 Experimental Benchmarks

One of the key stages in any experimental campaign is to ensure that the required calibration is completed. For the photodetachment experiments, there are a number of preliminary tests which must be first performed. Firstly, the H^- ion density will vary depending on the voltage applied to the Langmuir probe. The voltage must be large enough to attract all of the detached electrons, but care must be taken to ensure that the voltage is not too large to avoid secondary electron emission effects. Figure 4.1 shows the H^- ion density as a function of the applied voltage bias (V_{app}), and although the plasma potential (V_p) was measured to be 7 V, it can be observed that the H^- ion density did not saturate until V_{app} was 14 V. Increasing the voltage past this point had no affect on the H^- ion density. However, in order to be mindful of possible secondary emission effects the applied voltage was chosen to be $V_{app} = V_p + 7$ V.

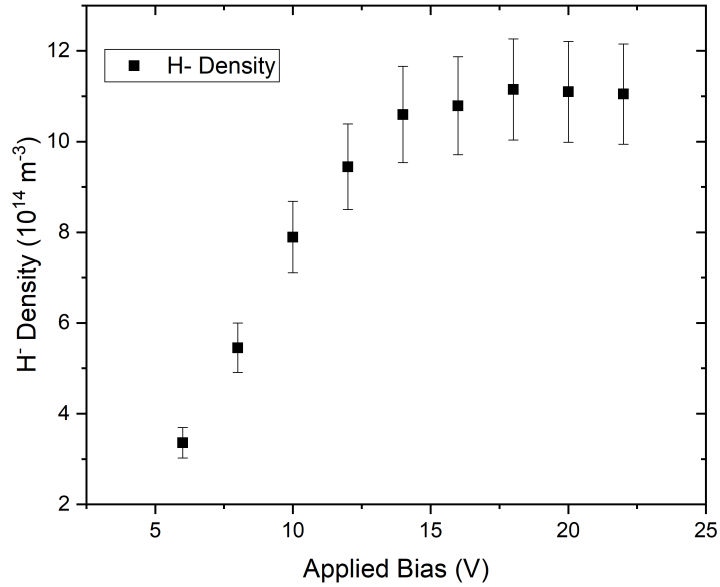


Figure 4.1: H^- densities as a function of applied voltages. A V_p of 7 V was measured, however, the H^- density does not saturate until 14 V. Therefore, all future experiments use an applied voltage of: $V_{app} = V_p + 7$ V in order to account for this.

Another key experiment to conduct is the affect of the laser energy on the H^- ion density, because if the laser energy is too low, then not all of the electrons will be detached. However, the laser energy must not be too large, as this may cause the liberation of electrons from

the tungsten tip. Figure 4.2 shows the H^- ion density as a function of the arbitrary laser energy settings (1-6). At low energies, the measured H^- ion density was initially low, but saturation quickly occurs. No additional increase in the H^- ion density was observed past this saturation point, which indicates that the liberation of electrons from the tip is negligible. The laser was operated at its maximum energy for all subsequent experiments.

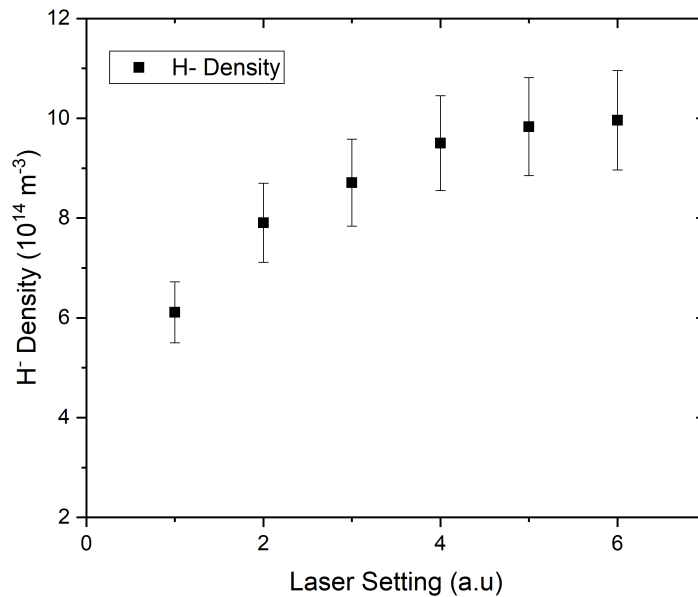


Figure 4.2: H^- density as a function of laser energy (the laser had 6 arbitrary energy settings). The H^- density was found to be fully saturated at the maximum setting, without causing secondary emission effects, so this was used for all future experiments.

The final conducted calibration experiment investigated the effect of the plasma pulse on the H^- ion density; this is especially important as the measurements taken within this section were time resolved within the plasma pulse. Chemical species within the plasma take a variable time to reach an equilibrium, depending on the species in question. Therefore, it is important to check when this equilibrium occurs for the H^- ions. Figure 4.3 shows the H^- ion density as a function of time within the pulse for two different metallic surfaces installed: aluminium and stainless steel 304. Whilst there are some variations in the densities throughout the pulse, an equilibrium is achieved almost immediately. For all subsequent experiments, the photodetachment pulses were synchronised to occur 2 ms into the plasma pulse, as this timing proved to be sufficient for the H^- ion density to be stable.

Whilst the previous three figures act as the core calibration for subsequent investiga-

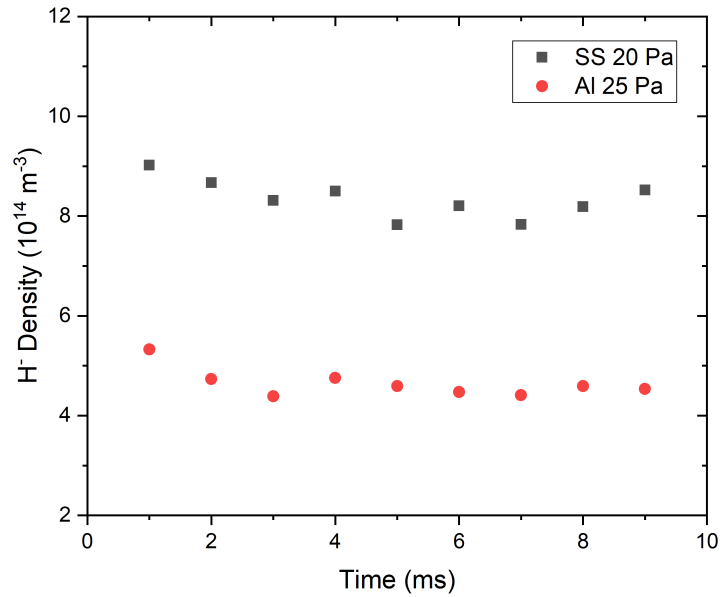


Figure 4.3: H^- density as a function of time within the plasma pulse. The H^- densities vary slightly within the pulse, however, it is approximately stable after 2 ms.

tions, it was also necessary to check for consistency in the acquired data. Figure 4.4 shows the H^- ion density as a function of power for the copper sample, at a pressure of 25 Pa. This experiment was conducted under identical conditions on three separate occasions, with the GEC reference cell being opened fully to atmosphere between each measurement. By comparing the measured densities, the standard deviation can be calculated for each power. This gave a range of percentage errors from 5.7–14.9 %, depending on the power. As there are no obvious correlations between the percentage error and the power, an average of all of these was taken; this resulted in an error of approximately 10 %. A similar experiment was also run by another PhD student, J. Branson, for a tungsten surface, which yielded approximately the same error. This error of 10 % has been attached to all experimental results.

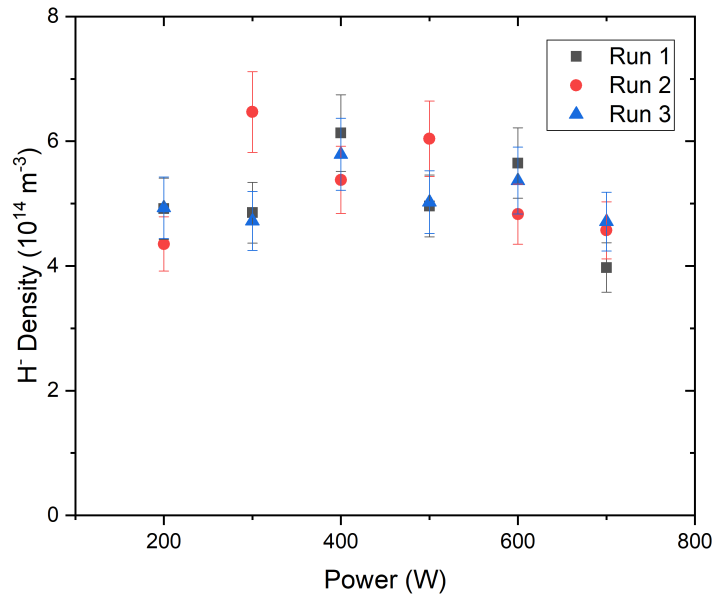


Figure 4.4: H^- density as a function of power with the copper surface, at a pressure of 25 Pa. Each experimental run was performed under the identical conditions, allowing for statistical error bars to be calculated from the standard deviation. This resulted in an average error of approximately 10%.

4.3 Stainless Steel 304 Surface

The first material investigated was the stainless steel 304 sample, hereafter referred to simply as steel. As discussed previously in the methodology section, Section 3.3, there are multiple steps required to calculate an absolute H^- ion density. These steps can be briefly broken down into the following sections. Firstly, an IV-curve must be acquired; this IV-curve is required for multiple steps of the experimental procedure. However, it can directly enable the electron density to be calculated; this is done by the Hiden ESPsoft package, which utilises orbital motion limited probe theory. The positive ion density is calculated and then, using the assumption of quasi-neutrality, the electron density is found. Figure 4.5 shows the measured electron density for the steel sample. Three different pressures, 20, 25, and 30 Pa, were investigated as a function of power. As expected, a linear increase of the electron density with increasing power for each pressure value was observed. All of the materials investigated within this chapter showed a similar linear relationship between applied power and electron density, therefore, the electron densities are not shown.

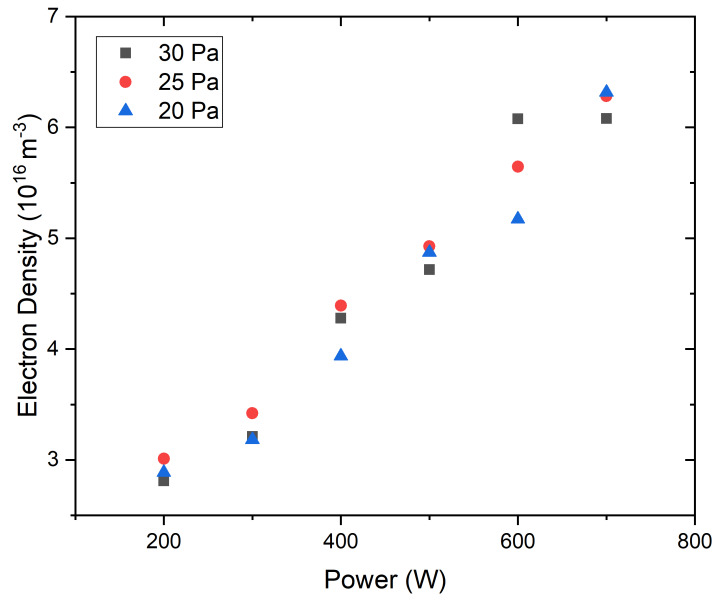


Figure 4.5: Electron density as a function of power for the stainless steel 304 sample, at three different pressures: 20, 25, and 30 Pa.

By measuring the size of the photodetachment pulse, and by knowing the current at V_{app} (I_{app}), the fraction of the total negative charges held within the negative ions, namely H^- ions, can be calculated. This value is referred to as the H^- fraction; this quantity can sometimes prove more useful in the analysis than the absolute density of H^- ions, because the absolute densities are a convolution of the H^- fraction and the electron density.

Figure 4.6 shows the H^- fraction as a function of power for the three pressures, 20, 25, and 30 Pa. The highest pressure, 30 Pa, corresponds to the lowest H^- fraction. However, as the power is increased past 400 W, an increase in the H^- fraction is observed. In contrast, the lowest pressure, 20 Pa, has the highest initial H^- fraction, but decreases with power. The 25 Pa experimental run results in a balance between these two extrema, with a slightly increasing H^- fraction with power.

Once the H^- fraction and electron densities have been found, then it is possible to calculate the absolute density of H^- ions. The absolute H^- ion densities for three different pressures, as a function of power, for the stainless steel 304 sample, are shown by Figure 4.7. The 20 Pa results show an initially high H^- ion density which increases to a maximum at 500 W, before decreasing below the 25 Pa results. In contrast, the 30 Pa results demonstrate an

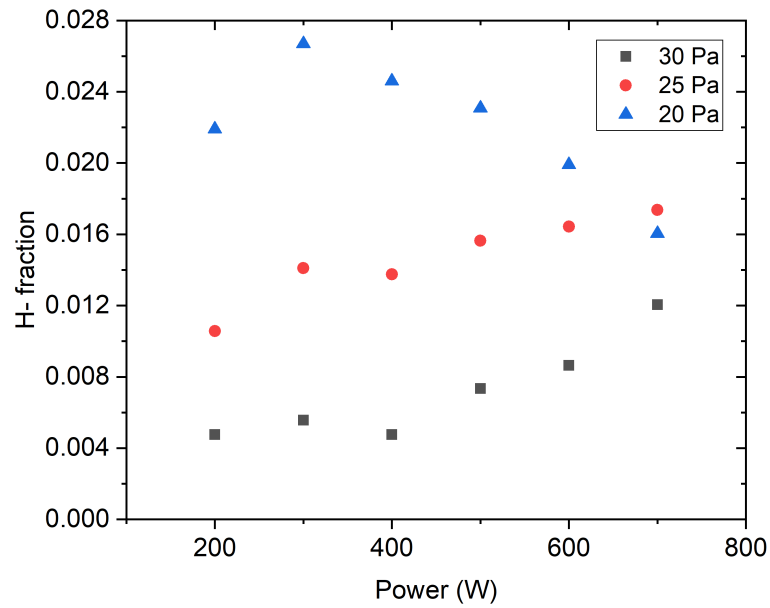


Figure 4.6: H^- fraction as a function of power for the stainless steel 304 sample, at three different pressures: 20, 25, and 30 Pa.

initially small H^- ion density, with only a slight increase between 200 and 400 W. However, at powers greater than 400 W, a linear increase with power is observed. Finally, the 25 Pa data set shows a linear increase with power, with the H^- ion densities being between that of the 20 and 30 Pa results. Interestingly, the 700 W data point yields a higher H^- density than at 20 Pa.

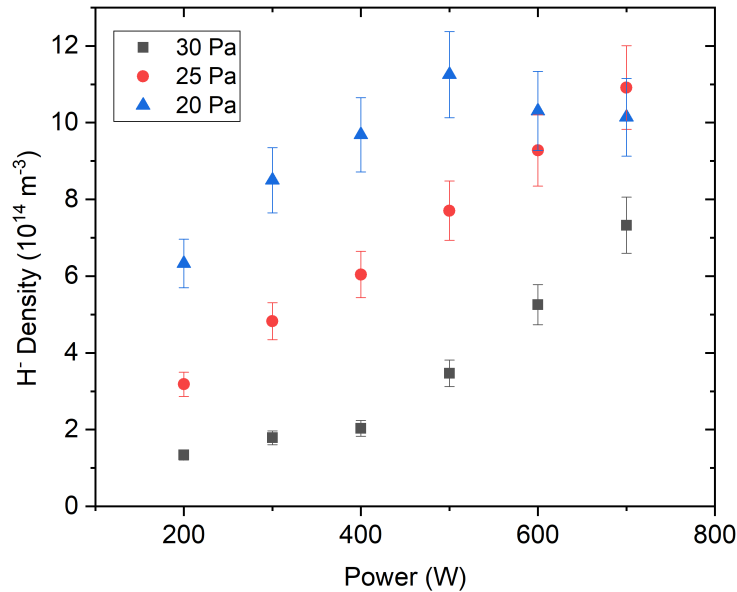


Figure 4.7: H^- density as a function of power for the stainless steel 304 sample, at three different pressures: 20, 25, and 30 Pa.

4.4 Copper Surface

In this section, the results from a copper grounded material are presented. Figure 4.8 shows the H^- fractions as a function of power for three different pressures, 20, 25, and 30 Pa. All three pressures show similar trends to each other, with an initially high H^- fraction, which then decreases with power. This is in contrast to the steel surface which exhibited pressure dependent trends. The highest pressure, 30 Pa, shows the smallest H^- fraction at all powers. However, in contrast to the steel sample, the 20 and 25 Pa results are similar to one another, with no clear distinction between them.

Figure 4.9 shows the absolute H^- ion densities as a function of power for the copper surface, at pressures of 20, 25, and 30 Pa. The absolute densities at lower powers, 200–400 W, demonstrate a similar pressure trend to those in Figure 4.7, with the highest pressure, 30 Pa, resulting in the lowest initial H^- ion density. However, for applied powers greater than 500 W, the H^- ion densities converge, regardless of the pressure. Interestingly, the variation in the measured densities is smaller than that for the steel sample.

The combination of different qualitative trends and absolute H^- ion densities suggests that the surface significantly affects the production or the destruction of H^- ions. The surface

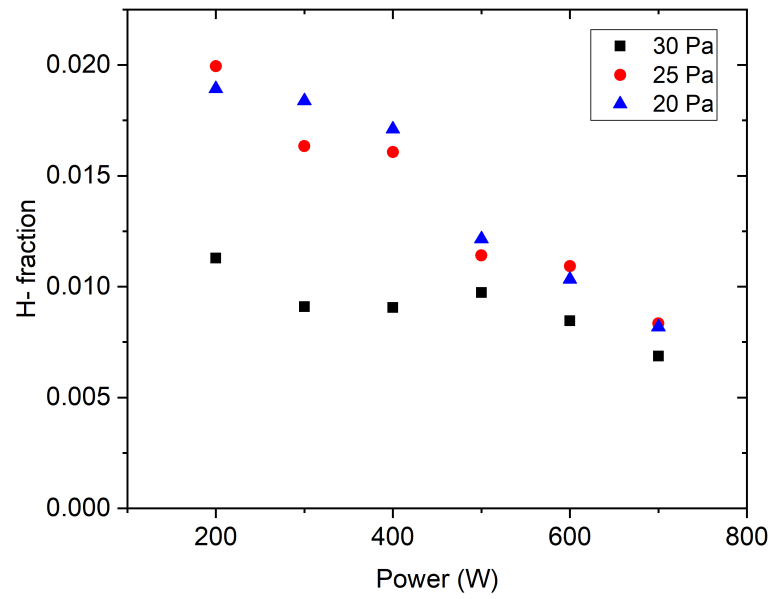


Figure 4.8: H^- fraction as a function of power for the copper surface, at three different pressures: 20, 25, and 30 Pa.

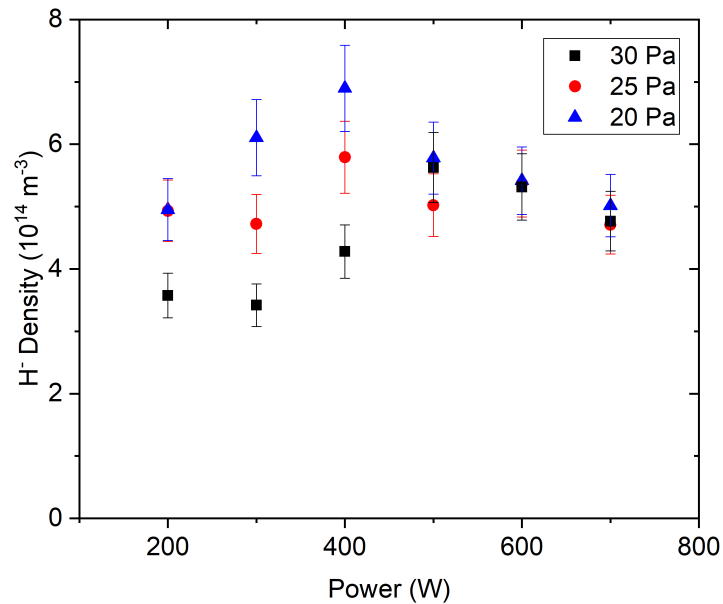


Figure 4.9: H^- density as a function of power for the copper surface, at three different pressures: 20, 25, and 30 Pa.

can affect the bulk plasma through multiple different mechanisms, including, secondary electron emission, recombination of atomic species, and direct surface production of negative ions. Each of these mechanisms may affect the measured negative ion density.

Secondary electron emission is the creation of fast electrons at the surface that are subsequently emitted into the bulk plasma. These electrons, hereafter named γ electrons, may create vibrationally excited species of molecular hydrogen. The dissociative attachment process requires vibrationally excited molecular species in order to generate negative ions. If the number of γ electrons varied between the steel and copper surfaces, then this could explain the differences in the H^- ion densities. If the two surfaces resulted in a different number of γ electrons, then this would be observed in the PROES images. Figure 4.10 compares the PROES measurements between a copper (**a**) and steel surface (**b**). The PROES images show two full RF cycles, with **I** denoting the sheath expansion stage in which the electrons are accelerated by the expanding sheath. The second structure **II** is when the sheath is fully expanded, and positive ion bombardment is at a maximum; this results in the largest emission of secondary electrons from the surface. The driven electrode is located at the top of the images ($Z = 4$ cm), and the grounded metallic surface is located at the bottom ($Z = 0.8$ cm). The plasma is operated at 20 Pa with an applied power of 500 W for both of these images. The PROES images imply that the plasma dynamics are almost identical to one another. If the differences in the H^- ion densities were due to γ electrons, then this should be observed as a differing intensity between the surfaces. The instance of this peak should be when the sheath is fully expanded (**II**), however, this is not observed. An example of this γ electron peak can be seen more clearly in Doyle et. al. [101].

Direct surface production of negative ions largely depends on the work function of the material [48]. A lower work function allows an electron to be more easily liberated from the surface, which can in turn be captured by an atomic species. Alternatively, two electrons can be simultaneously captured by a singularly charged positive ion; the later mechanism has been found to be more likely than the former. The work functions of the materials investigated are 4.55, 4.3, 4.65, 4.28, and 4.6 eV for tungsten, stainless steel 304, copper, aluminium, and molybdenum respectively [51,102]. The similarities between the work functions of steel and copper, and subsequently presented metallic surfaces, implies that direct surface production of negative ions is unlikely to be the cause of these discrepancies in the H^- ion densities.

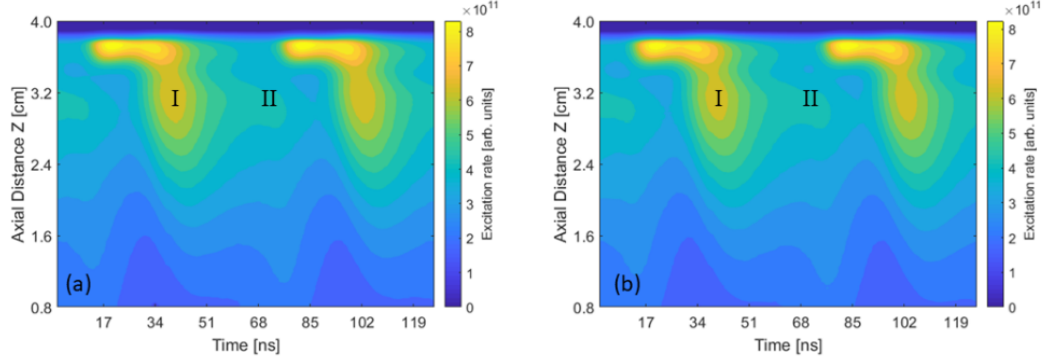


Figure 4.10: Results of phase-resolved optical emission spectroscopy measurements showing the excitation rate of the hydrogen α Balmer line at 656 nm. The plasma is operated at 20 Pa with an applied power of 500 W. Image (a) shows the copper sample and the image (b) for the stainless steel 304 sample. **I** denotes the instance of sheath expansion, and **II** denotes sheath expanded. During **II**, the effect of γ electrons should be the most pronounced.

The final consideration to make is the recombination of atomic species at the surface. As previously discussed, in Section 2.9.2, there are a number of pathways by which atomic recombination at the surface can occur. Both the ER and HA recombination processes can produce vibrationally excited molecular species due to their exothermic nature. These vibrationally excited species may then be released into the plasma, where the dissociative attachment can take place, producing negative ions.

These surface-produced vibrationally excited species may provide the answer for surface-to-surface variations in the measured H^- ion densities. We were unable to find studies that directly compare the vibrational distribution of copper and stainless steel surfaces. Nevertheless, there is a study by S. Markelj and I. Cadez in which they compared the vibrational distribution of molecular hydrogen between a copper and tungsten surface [103]. They observed a much larger vibrational temperature with the tungsten surface, as opposed to the copper surface. They combined their experimental measurements with a Monte Carlo simulation to suggest that the difference in vibrational temperature may be due to the presence of different binding sites on the surface of tungsten [104].

In order to facilitate a comparison between surfaces, based on the observations of Markelj et. al [103], a tungsten sample was also investigated. Figure 4.11 shows the H^- ion densities as a function of power for this tungsten surface. The qualitative trends with varying pressures are observed to be similar to those observed for the steel sample. A wider pressure range of 17–37.5 Pa was taken in order to ascertain whether the effects of pressure were more

pronounced at higher and lower pressures, compared with steel.

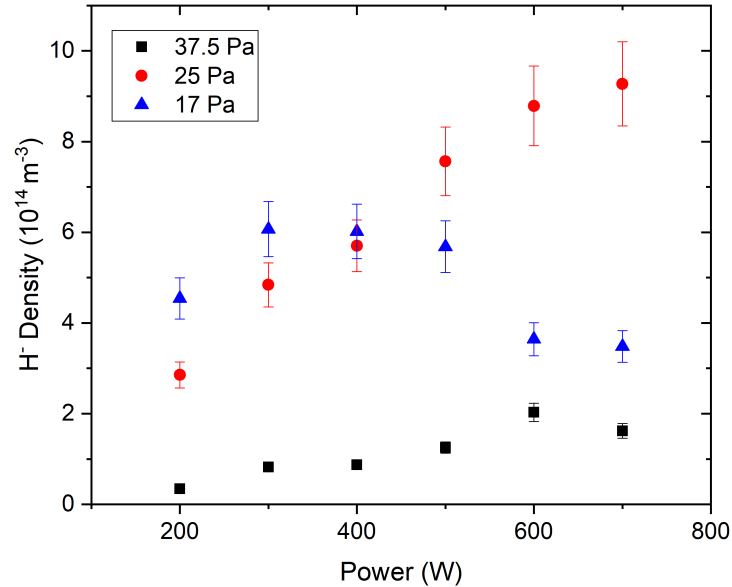


Figure 4.11: H^- density variation with power for the tungsten surface, at three different pressures: 17, 25, and 37.5 Pa.

4.5 Comparison Between Surfaces

This section focusses on directly comparing the absolute H^- ion densities between different materials. Figure 4.12 shows the direct comparison between the tungsten and steel surfaces at three different pressures. The H^- ion densities measured for the 25 Pa data set, agree within the error of each other. Additionally, whilst the pressures are different, the lower and higher pressures follow similar qualitative trends. Interestingly, in both cases, the lower pressure scans, whilst initially exhibiting the highest H^- ion densities, are superseded at higher powers by their 25 Pa counterparts.

The differences in the H^- ion densities between pressures may be due to one of three different mechanisms, or, a combination of these. All of which pertain to the increased number of collisions at higher pressures. The first considers the reduction in the number of fast electrons. At higher pressures, the plasma is more collisional; this acts to reduce the population of fast electrons for a set applied power. These fast electrons in the volume are required in order to create vibrationally excited species, which are necessary precursors for

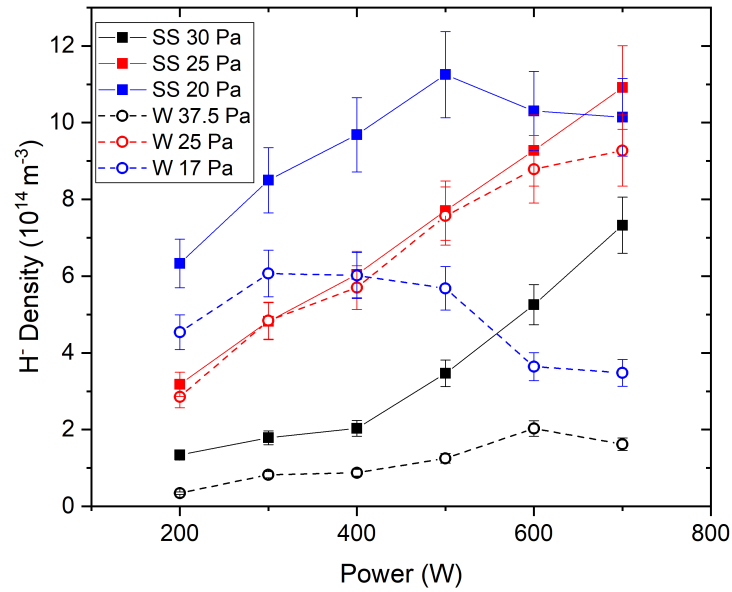


Figure 4.12: H^- density variation as a function of power for both the tungsten and steel surfaces, at three different pressures.

volume produced negative ions. A reduction in their density could decrease the population of vibrationally excited species, and in turn the negative ion density. The second mechanism may be due to associative detachment, Section 2.8.3.3, because if the atomic hydrogen density increases with pressure, then more H^- ions would be destroyed. If these were the only mechanisms, the variation of the H^- ion density with pressure should be similar between surfaces. However, the effects are more prominent for the steel and tungsten surfaces. An alternative, or complimentary, explanation requires a consideration of vibrational relaxation, specifically, relaxation through molecule-atom collisions. If the density of atomic hydrogen increases with pressure, for a set power, then this would increase the probability of a molecule-atom relaxation event, which acts to reduce the number of negative ions produced. The fast electron population may also provide an explanation for the reduction in the H^- ion densities for low pressure, high power operation. One of the key mechanisms for the destruction of H^- ions is through a collision with a fast electron via the electron detachment mechanism. At low pressures and high powers, the number of these energetic electrons is higher, which may explain the reduction in the measured H^- ion densities for low pressure measurements beyond 500 W.

Figure 4.12 shows that increasing pressure decreases the H^- ion density. Moreover, in the case of steel, it shows an unchanged H^- ion density for 30 Pa between 200 and 400 W. A similar result can be observed for the tungsten sample at 37.5 Pa, however, at this higher pressure, the H^- ion density only varies slightly between 200 and 700 W. The H^- ion density in the steel case, at 30 Pa, begins to increase between 400 and 700 W, which may be attributed to a continued increase in the electron density, relative to a plateau in the atomic hydrogen density. Subsequently, further studies are necessary to validate this hypothesis. The 20 Pa measurement for steel and the 17 Pa measurement for tungsten show similar trends, with an initially high H^- ion density which increases with power until a maximum. A further increase in power past this maximum results in a decrease in the H^- density, which may be attributed to the destruction of negative ions through electron detachment.

As previously discussed, there appears to be an observable difference between the pressure dependent qualitative trends with a steel or tungsten surface installed, compared to a copper surface. In order to ascertain whether copper was the exception to other surfaces, an aluminium surface was also investigated. Figure 4.13 shows the absolute H^- ion density measurements for three different pressures for both the copper and aluminium surfaces. A similar pressure dependent trend can be observed, with the highest pressures, 30 Pa, resulting in the initially smallest H^- ion density. The aluminium surface typically results a smaller observed H^- ion density at all pressures than that of a copper surface, however, at powers of 500 W and larger, the densities converge. An interesting point to note is that the 20 Pa result for aluminium, yields the lowest H^- ion density at 700 W. This is in contrast with negative ion sources, where the lowest pressure is used to yield the highest negative ion density.

Figure 4.14 allows a direct comparison to be drawn between the five different surfaces, namely, tungsten, stainless steel 304, copper, aluminium, and molybdenum. The H^- ion densities were measured as a function of power at a gas pressure of 25 Pa. The data suggests that the five surfaces can be split into two distinct groups, one containing tungsten and steel, and the other containing copper, aluminium, and molybdenum. The notable difference in the measured H^- ion densities between these different material sets may be explained by the difference in the vibrational temperature, as previously discussed. The data sets for both tungsten and steel agree with each other, within the error, for every data point, and appear to display a linear trend with power.

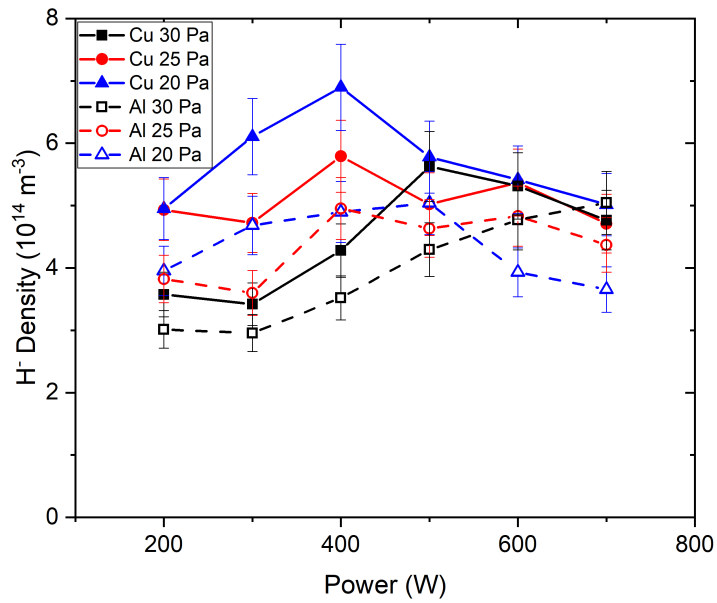


Figure 4.13: H^- density variation as a function of power for both the copper and aluminium surfaces, at three different pressures: 20, 25, and 30 Pa.

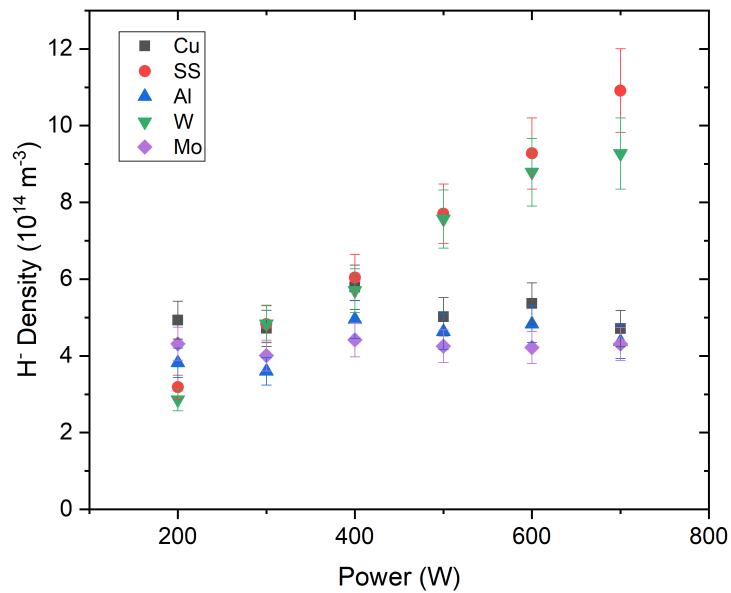


Figure 4.14: H^- density as a function of power for five different surfaces, including: tungsten, stainless steel 304, copper, aluminium, and molybdenum, at a gas pressure of 25 Pa.

4.6 Discussion

Much of the discussion of these results is contained within the previous sections. However, there are various considerations which require addressing, even if only to elucidate as to why their effects were neglected.

4.6.1 Comparison to Literature

The absolute H^- ion densities measured within this study are comparable to other experimental studies [105,106], although some adjustment is necessary due to the different reactor configurations and pressures. Some of the surfaces have been directly compared before for the creation of H^- ions. For instance, it has been shown that stainless steel increases the relative density of H^- ions by a factor of 2 when compared to a copper wall [107]. Although, the opposite has also been reported by Leung *et. al.* and Fukumasa *et. al.* [108,109]. Other materials have also been investigated and compared, for example, tungsten and tantalum [110]. One of the problems with these studies are the deviations in the experimental apparatus and operating conditions. To this end, a standard reference reactor, such as the GEC reference cell, may allow for more direct comparisons.

A study by S. Markelj and I. Cadez [103], measured and compared the vibrational temperatures between tungsten and copper surfaces. This showed a larger vibrational temperature from the tungsten surface, compared to the copper one. Given the necessity of vibrationally excited species in the generation of negative ions through the dissociative attachment pathway, this may act to evidence the relatively high H^- ion densities measured in tungsten compared to copper.

4.6.2 Surface Loss Rates

One of the first considerations made was the direct influence of the atomic species. The loss of atomic hydrogen through surface interactions can generally be categorised as the surface loss coefficient β_H . The exact values of this vary from surface-to-surface, and may depend on the operating conditions of the plasma. A full investigation of this parameter would require not only atomic hydrogen densities, but also a measure of atomic velocities. A relative scaling of various materials has been conducted by Sode *et. al.* [111]. In their paper, they reported that the β_H values for copper and stainless steel were approximately equal;

with β_H for tungsten being twice as small and aluminium five times smaller. The combined sets of data presented within this chapter do not scale in the same way as reported, which suggests additional effects were causing the observed trends.

4.6.3 Thermal Properties

The plasma was, as previously mentioned, operated in a pulsed mode due to the thermal load on the samples. However, the thermal conductivities may have influenced the measured H^- ion densities. The temperatures of the samples were measured prior to plasma exposure, with temperatures ranging from 20–24 °C. The temperatures were then remeasured post exposure, which confirmed a negligible variation. These temperatures were not measured in situ, but after the chamber was vented to atmosphere; this may have allowed sufficient cooling to mask the thermal effects. The thermal conductivities of the samples were investigated as a possible cause for the surface-to-surface discrepancies in the H^- ion densities. The thermal conductivities were 197 $W(mK)^{-1}$, 15 $W(mK)^{-1}$, 413 $W(mK)^{-1}$, 237 $W(mK)^{-1}$, and 143 $W(mK)^{-1}$ for the tungsten, steel, copper, aluminium, and molybdenum surfaces respectively. The differences in the thermal conductivities do not map onto the observed variations in the H^- ion densities between surfaces. It was concluded that these differences in thermal conductivity were unlikely to have been the cause of the H^- ion density variations.

4.6.4 Interstitial Hydrogen Trapping

It was considered that atomic hydrogen may be trapped within the crystalline lattice of the various metallic surfaces. These captured hydrogen atoms can then be released through ionic collisions with the surface, and may capture an electron during their liberation. The lattice constants were 3.593, 3.155, 3.597, 4.046, and 3.142 angstroms for tungsten, steel, copper, aluminium, and molybdenum respectively. Given how similar these lattice constants are, it was deemed unlikely that adsorbed hydrogen into interstitial sites was causing the observed variations.

4.7 Chapter Summary

The results presented within this chapter demonstrate a dependency of the measured H^- ion density on the parameters, power, pressure, and surface material. The steel and tungsten

samples were observed to cause similar trends in the H^- ion density when power and pressure were varied. Their agreement was particularly pronounced in the 25 Pa measurements, where the measured densities agreed within the error for every data point. In contrast, the copper, aluminium, and molybdenum surfaces were observed to result in different qualitative trends to the steel and tungsten samples, yet were similar to one another. It has been proposed within this chapter that the most likely explanation for the difference in the measured H^- ion densities may be due to the different number of vibrationally excited molecules created at the surface. This hypothesis is supported by vibrational temperature measurements conducted by S. Markelj and I. Cadez [103]. They compared the vibrational temperature resulting from a tungsten and copper sample, and observed that the tungsten sample yielded a considerably higher vibrational temperature. These vibrationally excited species may then undergo dissociative attachment in the bulk plasma, creating the observed H^- ions.

The variation in the H^- ion densities with pressure, are more apparent for both the steel and tungsten surfaces, as opposed to the copper, aluminium, and molybdenum surfaces. This may suggest that vibrational relaxation plays a crucial role in limiting the density of negative ions within the volume. Further work should focus on measuring the vibrational distribution. Ideally, these measurements could be taken at different axial positions as this would evidence the effect of the surface to a greater extent. This would allow a direct comparison between the vibrational temperatures and the H^- ion densities and facilitate a more direct comparison between the two effects.

Chapter 5

An investigation of direct surface production of negative ions from novel surfaces.

5.1 Prelude

This chapter presents relative negative ion yields measured by EQP mass spectrometry, as discussed in Section 3.5.3. Two materials were investigated within this chapter, nitrogen doped diamond (NDD) and a nanoporous $12\text{CaO} \cdot 7\text{Al}_2\text{O}_3$ (C12A7) electride. The materials were negatively biased with respect to the plasma for two reasons. Firstly, to facilitate positive ion bombardment of the surfaces, which results in surface produced negative ions. Secondly, to repel the surface produced negative ions towards the grounded aperture of the mass spectrometer. The applied surface biases were varied between $V_s = -20$ V and $V_s = -130$ V.

The degree of doping during the creation on the NDD samples was varied, with three different parts per million (ppm) investigated, 20, 50, and 100 ppm. The investigation was performed within a helicon reactor, consisting of an upper cylindrical source chamber that was connected to a lower spherical diffusion chamber. The plasma used was a hydrogen, or deuterium, capacitively coupled plasma, at a gas pressure of 2 Pa. The plasma was driven using a 13.56 MHz RF source, operated at 26 W applied power. For more details regarding the experimental setup, please refer to Section 3.5.1.

The sample holder allowed simultaneous heating and biasing of the samples. The distance between the samples and the mass spectrometer was measured to be 37 mm and the samples had a uniform area of 1 cm^2 . The relative populations of the positive ionic species, H^+ , H_2^+ , and H_3^+ , were measured using the mass spectrometer. The dominant ion was H_3^+ , with a population of approximately 90 % of the total positive ions. The samples were located normal to the aperture of the mass spectrometer, this alignment was checked by performing an angular measurement in each case. The maximum signal from this angular measurement was assumed to be the correct alignment.

The majority of the figures presented within this chapter discuss the yield of negative ions. The definition of the word *yield* has changed multiple times in the group's publishing history. Therefore, I would like to explicitly draw attention to the usage of this word within this chapter. Negative ion energy distribution functions (NIEDFs) were measured by the aforementioned mass spectrometer, and the yield is defined as the area under the NIEDF curves. Furthermore, the level of doping is referred to multiple times within this chapter. In every instance, this refers to the level of dopant in the gas phase during the creation of the nitrogen doped diamond films.

The data presented within this chapter is the result of a collaboration between the author and the Physics of Ionic and Molecular Interactions (PIIM) group at Aix-Marseille University, France. The NDD samples were prepared by an external company and provided to the PIIM group. However, all of the data was acquired, processed, and interpreted by the author. The electrified sample was created by Hosono et. al. [112] at the Tokyo Institute of Technology, Japan. Additionally, the electrified measurements were conducted in tandem with M. Sasao from Doshisha University, Japan and R. Moussaoui from Aix-Marseille University, France. The acquisition, processing, and analysis of the data was a combined effort between the author, the members of the PIIM group, and M. Sasao. This work has subsequently been published by M. Sasao [1].

5.1.1 Literature Review

The motivation for studying negative ions has been previously discussed in Section 2.7.3.1. However, a brief literature review of the PIIM's group research is prudent as it explains why NDD was chosen for study. One of the aims of the research group is to investigate alternative materials to caesium for the production of a large quantity of negative ions. In

particular, they focus on using insulating materials, due to their tendency for large band gaps, which may enhance negative ion production. For more information regarding why insulating materials are of interest please refer to Section 2.9.4.2.

One of the original candidates that was investigated, as a replacement to caesiated metallic surfaces, was highly orientated pyrolytic graphite (HOPG) [113,114]. It was reported elsewhere that diamond-like carbon surfaces result in a yield twice that of graphite [115], and a mechanism for this was proposed by Linermann *et. al.* [116]. The PIIM group later showed a 5-fold increase in the negative ion yield with a boron doped diamond (BDD) surface compared to HOPG [117]. The addition of a boron dopant was chosen in order to provide p-type doping, and to improve the conductivity of diamond at room temperature. The yield of negative ions was always higher with BDD than for MCD. However, no effect from the level of doping was observed. Ahmad *et. al.* [78] compared HOPG, BDD, nanocrystalline diamond, and ultra nanocrystalline diamond surfaces for their production of H^- ions. It was reported that HOPG surfaces showed the highest yield at room temperature. Although, at 400 °C, the BDD surfaces were shown to have the highest yield. Ahmad *et. al.* combined these H^- ion measurements with Raman spectroscopy. They concluded that the hydrogen content of the surface, hydrogen atoms trapped in the first few nm of the material, and the sp^3/sp^2 ratio, were key parameters in the direct surface production of H^- ions for carbon based materials. This work has been extended recently in order to discuss the effect of surface erosion and modification, due to positive ion bombardment [118].

Nitrogen doped diamond was chosen due to its n-type doping, which in the case of nitrogen, creates a deep donor level in the band gap of the diamond at approximately 1.7 eV [119]. This lowers the overall work function of the diamond to approximately 3.1 eV [120], which is lower than the p-type BDD samples; these have a work function of approximately 3.9 eV [120]. The utilised electrified material has been measured to have a work function of 2.4 eV [44], which is comparable to that of metal potassium, whilst being chemically and thermally stable. In comparison, the work function of caesium is 2.1 eV [44], which makes the electrified sample an interesting material for further investigation.

5.2 Nitrogen Doped Diamond

Before measurements comparing the different doping levels could be conducted, some calibration experiments were required. In order to ensure that an equilibrium was reached, the time evolution of the yield for the 100 ppm NDD sample was measured; this is shown by Figure 5.1. It was observed that an equilibrium was reached after approximately 7 minutes. All future measurements were conducted after a ten minute equilibrating period in order to reduce the drift in yield.

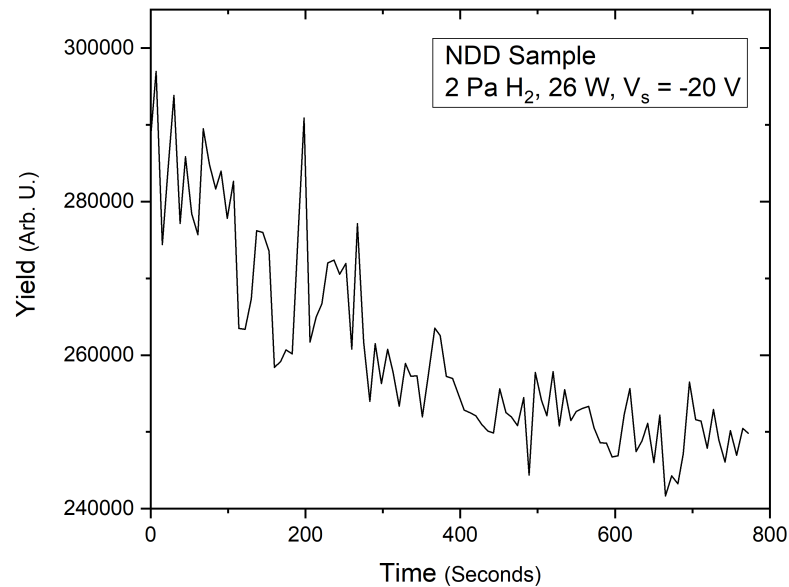


Figure 5.1: Negative ion yield as a function of time for the 100 ppm NDD sample. The sample was heated to 400°C, at a gas pressure of 2 Pa, and a surface bias of -20 V.

At room temperature, it was not possible to continuously bias any of the NDD samples, regardless of dopant level. Therefore, the samples were thermally heated by a tungsten filament that was located behind the sample. The temperatures of the samples were recorded using a thermocouple, located inside the frame of the sample holder, that was calibrated by using a second thermocouple that was connected to the plasma facing surface. However, this method does induce a notable error due to minor variations in thermal conductivity, sample thickness, and thermal contact with the sample holder. The error in the temperatures are estimated to be $\pm 20^\circ\text{C}$; the error bars have not been shown on any figures within this chapter to improve the legibility of the figures. It was found that heating the 100 ppm NDD

sample to 400°C was sufficient to allow for biasing of the sample.

It has been previously discussed that the majority of the figures within this chapter will discuss the negative ion yield; this is defined by the area under the NIEDF curve. Figure 5.2 gives examples of these NIEDFs at different temperatures for the 100 ppm NDD sample, biased at -20 V . The vertical axis represents the counts per second on the detector of the mass spectrometer. The horizontal axis represents the negative ion energy after a subtraction of the energy, that has been gained from the potential profile, which exists between the surface and mass spectrometer. It is known that negative ions can be generated through dissociative attachment in the volume, therefore, it was confirmed that the negative ions were created through surface production. This was completed by measuring the NIEDF without any bias applied to the surface, that resulted in no measurable NIEDF; the potential profile does not allow volume produced negative ions to be extracted. This consequently confirmed that any measured negative ions were created at the surface. The low energy peak of this NIEDF is indicative of negative ion generation through sputtering processes [79]. The 400°C NIEDF has an lower overall count than the other temperature measurements. This is likely because this sample was not fully biased at this temperature, unlike the other samples.

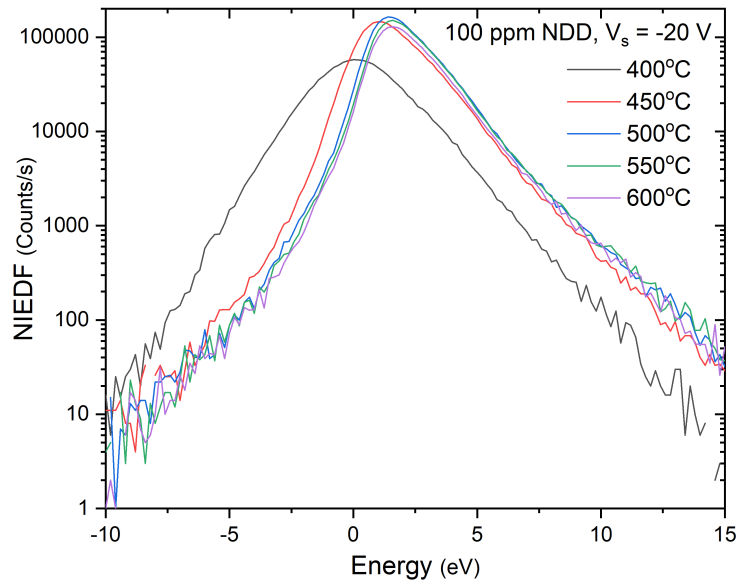


Figure 5.2: Negative ion energy distribution functions for the 100 ppm NDD sample at different temperatures. The gas pressure was set to 2 Pa with 26 W of external power applied to the plasma.

Figure 5.3 shows the negative ion yield as a function of temperature for the 100 ppm NDD sample biased at -20 V. An initial increase in the yield can be observed up to a maximum at 450-500°C before a decrease at higher temperatures. This trend has also been observed by Kumar *et. al.* [117] in their study of micro-crystalline boron doped diamond (MCBDD) samples, and is characteristic of a change in the sp^3/sp^2 ratio. However, the 100 ppm NDD sample exhibits this trend at a higher temperature than reported for MCBDD. The sp^3/sp^2 ratio likely changes due to the repairing of non-diamond bonds, that occurs through annealing at higher temperatures. This effect was confirmed by Ahmad *et. al* [78] who reported a progressive increase in the sp^3/sp^2 ratio at higher temperatures, after plasma treatment at room temperature. The decrease in yield at higher temperatures has also been previously observed [114], and is attributed to the difficulties that can be encountered when measuring higher energy negative ions [121]. Whilst this is the likely explanation for the macroscopic trend, it should be noted that the yield at 400°C may be lower than expected due to the challenges in biasing the sample at low temperatures.

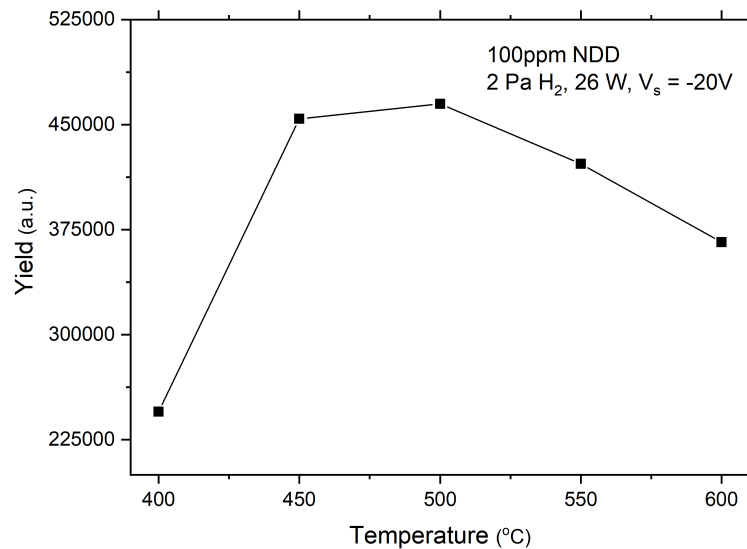


Figure 5.3: Negative ion yield as a function of temperature for the 100 ppm NDD sample at a gas pressure of 2 Pa, with a surface bias of -20 V. A peak can be observed between 450-500°C, before the yield begins to decrease with power.

Figure 5.4 shows the negative ion yield as a function of the surface bias magnitude for the 100 ppm NDD sample, at a temperature of 500°C. A peak can be observed at 30 V, before a pattern of decreasing yield with increasing bias emerges. The initial increase in the

yield, up to 30 V, is likely because the impinging positive ions require sufficient energy in order to sputter the adsorbed hydrogen from the surface. Secondly, once the negative ions are created at the surface, they require extraction to the aperture of the mass spectrometer. A higher bias increases the likelihood of their extraction. The higher negative biases cause a further increase in the acceleration of the positive ions towards the surface that can cause significant surface damage upon their impingement. The decrease in the yield at higher biases is attributed to this surface damage [118].

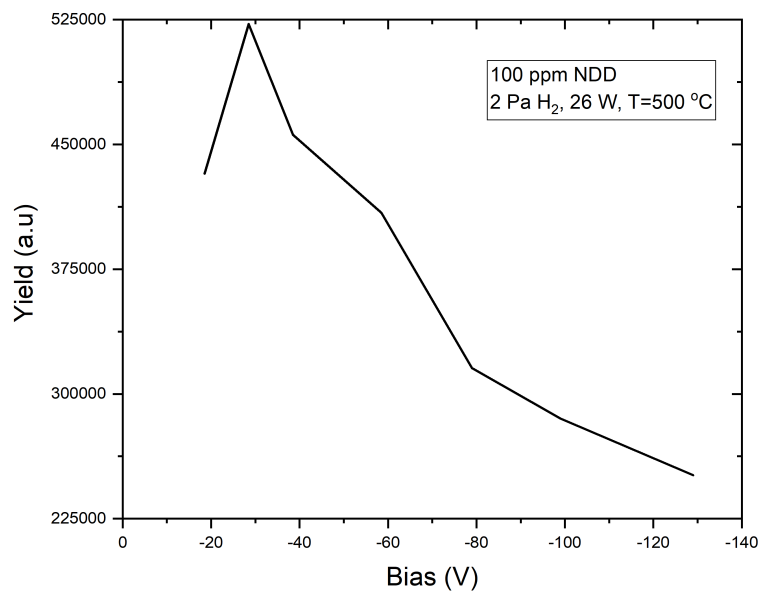


Figure 5.4: Negative ion yield as a function of the applied bias magnitude for the 100 ppm NDD sample at 500°C. A peak can be observed at 30 V, before the yield begins to decrease with additional bias.

Whilst increasing the surface bias does appear to result in considerable surface damage, it is worth noting that this damage is reversible. Figure 5.5 shows the negative ion yield as a function of time, at a surface bias of -20 V, after previous exposure to a higher surface bias, up to a maxima of -100 V. The higher biases result in a lower yield, however, the recovery of the signal can be seen over the course of many minutes. The yield was measured again the next morning, and a full recovery of the signal was observed for every bias. One of the key advantages NDD may have over other surfaces, such as caesium, is its ability to recover the signal after exposure. Caesium negative ion sources require continuous evaporation of caesium upon a metallic grid, which creates numerous technical problems, and a significant

maintenance cost [122, 123].

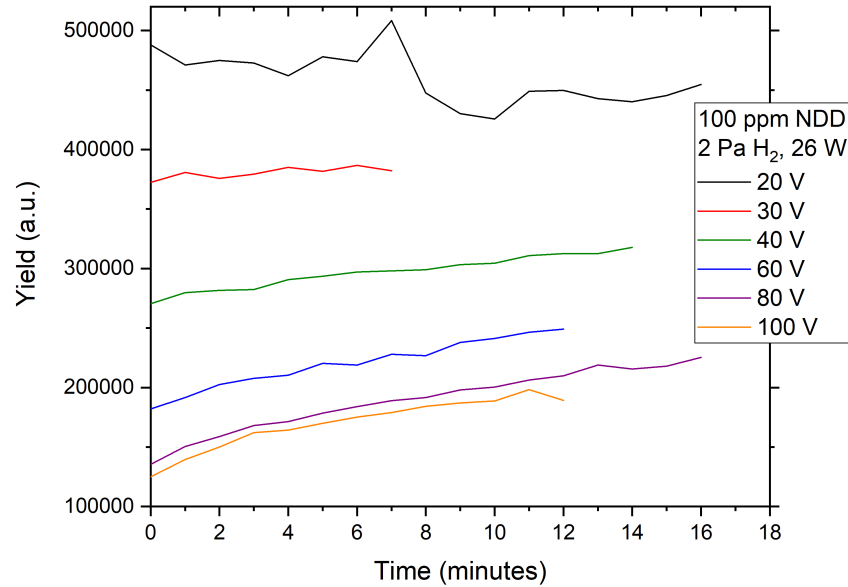


Figure 5.5: Negative ion yield as a function of time for the 100 ppm NDD sample at 500°C. The samples were exposed to a (negative) bias of a magnitude between 20 and 100 V, before being returned to -20 V.

It had been previously observed that varying the dopant level of boron did not result in a significant change in the negative ion yield. One of the goals of this investigation was to confirm whether this was also the case with nitrogen doping. Figure 5.6 compares the negative ion yield as a function of temperature between a 50 and a 100 ppm NDD sample. The 50 ppm NDD sample could not be biased at 400°C, hence why this data point is not reported. The same characteristic trend with temperature can be observed, with a peak in the yield observed at 500°C. Regardless of the temperature, the 100 ppm NDD sample had a higher yield than the 50 ppm NDD sample. The most likely explanation for why a higher dopant level results in a higher yield is the creation of more deep donor levels. These deep donor levels act to reduce the overall work function of the material [120], which allows electrons to be more easily liberated. These electrons can then be captured by sputtered hydrogen species in order to create H^- ions.

In order to ascertain whether this result was indicative of a trend or simply an anomaly, a 20 ppm NDD sample was also investigated. Figure 5.7 shows all three of these samples as a function of temperature. Regardless of temperature, the 20 ppm NDD sample resulted in

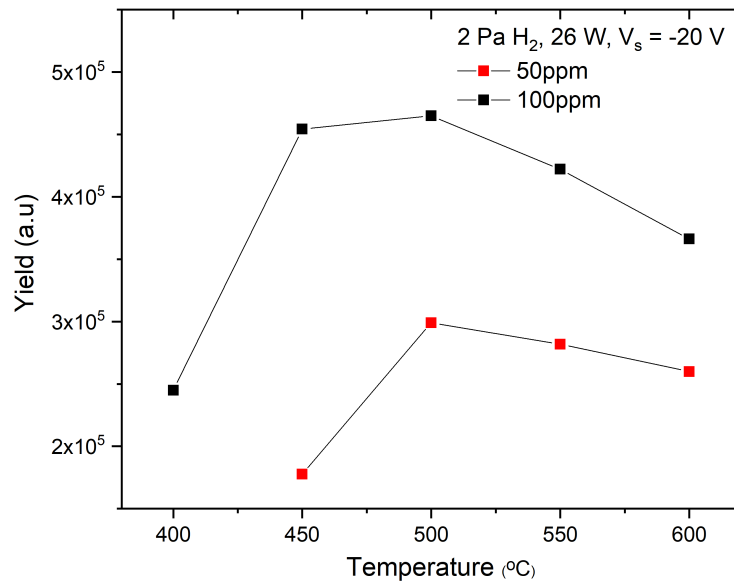


Figure 5.6: Negative ion yield as a function of temperature for an applied bias of -20 V, shown for both the 50 and 100 ppm NDD samples.

a larger yield than either of the other dopant levels. The most likely reason for why this is case is the crystal faces of the samples. As previously mentioned, the doping refers to the concentration of nitrogen in the gas phase during the production of these samples. Different levels of nitrogen in the gas phase resulted in different crystalline faces being preferentially formed. The 50 and 100 ppm samples primarily contained the (111) crystalline face, however, the 20 ppm NDD sample contained a combination of both (100) and (111) faces. Confocal microscopy images of these three samples are shown by Figure 5.8, which confirms the previously discussed crystalline faces. These images were not taken by the author, but by the company who provided the samples. For a description on how confocal microscopy works please refer to Section 3.7 *Confocal Microscopy*. It is not yet fully understood why the combination of two crystalline faces would result in a higher negative ion yield. Nevertheless, it is likely because of the varying electronic properties, such as the conductivity, of different crystalline faces.

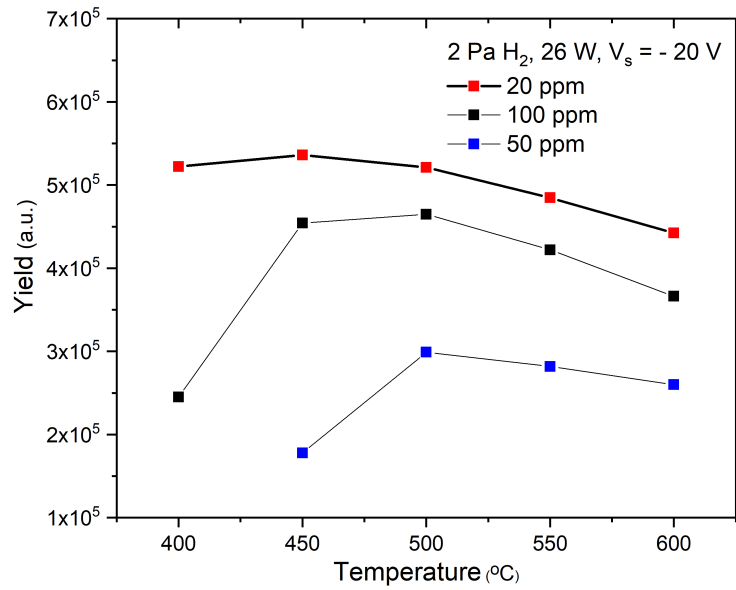


Figure 5.7: Negative ion yield as a function of temperature for an applied bias of -20 V, for the 20, 50, and 100 ppm NDD samples.

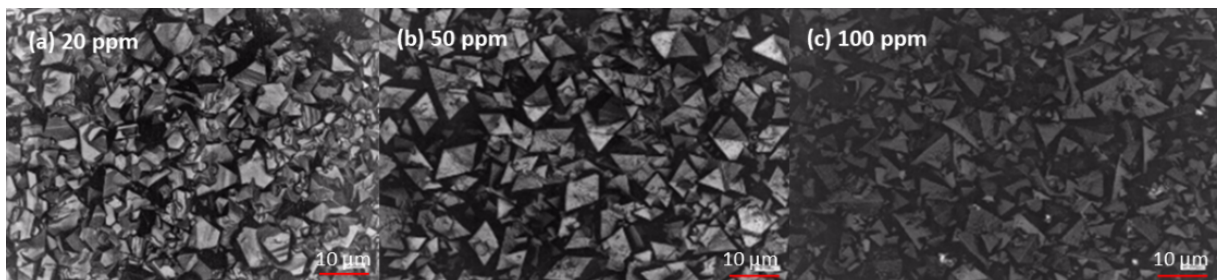


Figure 5.8: Confocal microscopy images for the three different NDD samples: a) 20 ppm b) 50 ppm c) 100 ppm. The 50 and 100 ppm samples clearly show a preference for the [111] crystalline plane, in comparison to the 20 ppm, which contains a mixture of both the [100] and [111] planes.

5.3 Electride Results

The graphs presented within this section have already been published by M. Sasao et. al. [1], however, the figures have been approved for reuse by the journal. The material investigated in this section is a $12CaO \cdot 7Al_2O_3$ electride, created by Hosono et. al. [112,124,125]. The work function of this material has been measured previously to be 2.4 eV [44], for comparison, the work function of caesium is 2.1 eV [44]. This low work function was one of the key reasons why the surface was investigated in order to assess its potential for creating a large number

of negative ions. One advantage the electrified material has over doped diamond samples, apart from a lower work function, is the ability to bias at room temperature; this is achieved because the material contains an abundant number of hydride ions and irradiation through UV light [126].

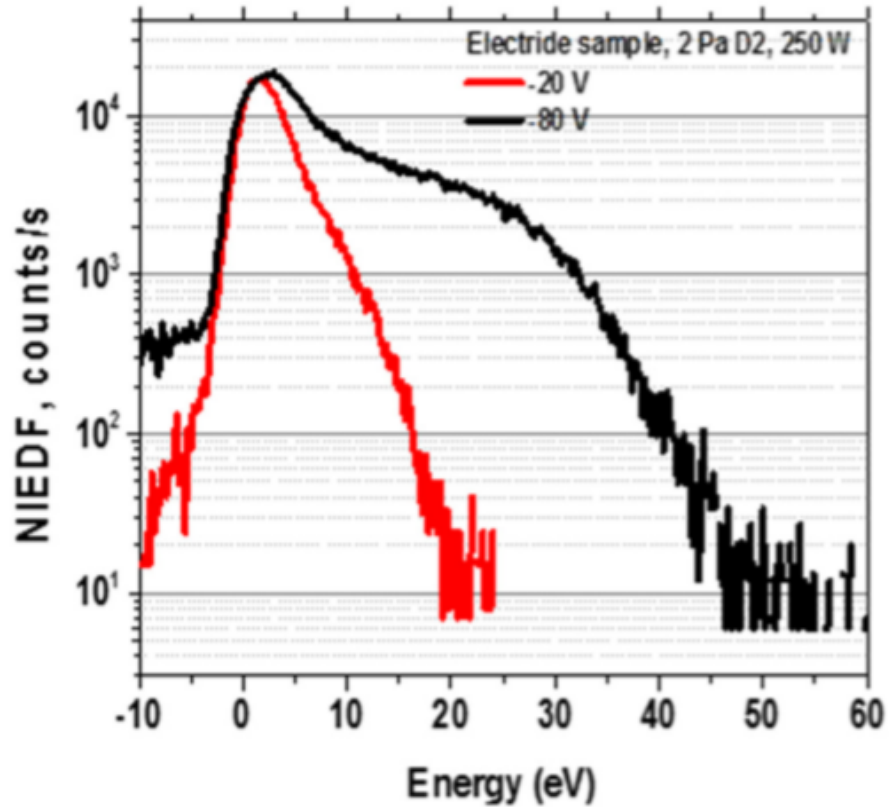


Figure 5.9: NIEDF for the electrified sample immersed into a RF driven 2 Pa deuterium plasma with an applied power of 250 W. Two separate biases have been applied, the first at $V_s = -20$ V and then second at $V_s = -80$ V. Copyright (2018) The Japan Society of Applied Physics [1].

Figure 5.9 shows the NIEDF of the electrified sample immersed in a 250 W RF 2 Pa deuterium plasma at two different surface biases (-20 and -80 V). The -20 V surface bias NIEDFs are comparable to that shown previously for the NDD samples, with the low energy contribution originating from direct sputtering of adsorbed hydrogen (or deuterium). The higher surface bias (-80 V), shows a combination of two mechanisms, firstly the sputtering as mentioned previously, and a broader higher energy contribution. This higher energy contribution is due to the backscattering process, which is a result of energetic ions, and atoms, impinging upon the surface whilst retaining a major part of their kinetic energy.

These energetic particles can capture a single electron, in the case of atomic species, or two electrons for singularly positive charged species to form a highly energetic negative ion. The contribution of backscattering to the NIEDF is broad for two main reasons. Firstly, the fraction of the energy lost due to the collision with the surface is not constant, which allows reflected ionic species to have a large range of energy values. Secondly, the negative ion measured is D^- , however, the impinging positive ion can be one of three ions D^+ , D_2^+ , and D_3^+ . The charge to mass ratios of these ionic species are different, and therefore upon their reflection (and subsequent capture of two electrons) the range of energy which the negative ion can contain is significantly broader than negative ions produced directly through sputtering. This was confirmed by Schiesko et. al. who reported the maximum energy of the D^- was always lower than that of H^- [127].

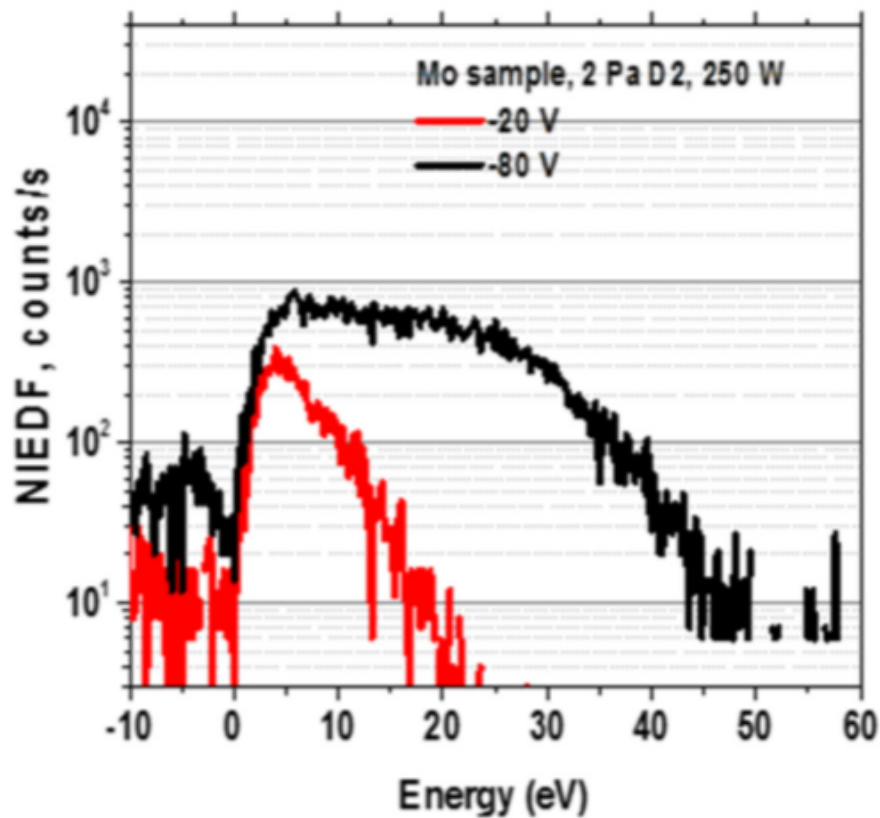


Figure 5.10: NIEDFs for the molybdenum sample immersed into a RF driven 2 Pa deuterium plasma with an applied power of 250 W. Two separate biases have been applied, the first at $V_s = -20$ V and then second at $V_s = -80$ V. Copyright (2018) The Japan Society of Applied Physics [1]

One of difficulties in measuring the contribution of backscattered negative ions is the

angle in which they are reflected. The sputtered negative ions are more likely to reach the aperture of the mass spectrometer, because they are emitted from the surface closer to the normal than backscattered ions [121]. In order to accurately measure the contribution of the backscattered negative ions an angular scan must be conducted, which can be combined with simulations in order to produce an accurate result for the total yield of negative ions. Whilst these angular scans were performed by the author, partly to check for the angular alignment of the sample with respect to the aperture of the mass spectrometer, the simulation work was completed by another author and is therefore not presented here. An example of these simulations for MCBDD can be found by Kogut *et. al.* [118]. By conducting an angular measurement, a negative ion angular energy distribution (NIAEDF) can be acquired, which can be processed to give a more representative yield of negative ions.

A molybdenum target was also investigated in order to facilitate a comparison to the electrified sample, as shown by Figure 5.10. The molybdenum sample was immersed in a 250 W RF 2 Pa deuterium plasma at two different surface biases (-20 and -80 V) and the NIEDF was measured. The maximum number of counts in each instance is over an order of magnitude lower than that of the electrified sample. Both the sputtering and backscattering contributions decrease by a similar order of magnitude with the molybdenum sample installed, compared to that of the electrified sample.

In order to confirm that the low energy peak was due to sputtering processes, the NIEDF was measured under two different plasma conditions. The sample was first exposed to a 1 Pa hydrogen ECR plasma at an applied power of 60 W with a surface bias of -130 V for 10 minutes. The timing for this was chosen as a saturation was observed after 10 minutes, with no further signal increase after 30 minutes, or two hours of exposure. Following this, it was exposed to either a ECR argon plasma (shown in black, 0.1 Pa, 30 W) or a ECR hydrogen plasma (shown in red, 1 Pa, 60 W) both with an applied surface bias of -60 V. The results for this experiment are shown by Figure 5.11. In both instances, the low energy peak associated with direct sputtering of adsorbed hydrogen was present, indicating that the process is driven by the desorption of previously embedded hydrogen. As expected, the backscattering contribution was only present in the case of a hydrogen plasma; as there were no hydrogen species present in the argon plasma to be backscattered.

The final experiment conducted was the effect of heating the material in order to reduce the adsorbed hydrogen content. The sample was exposed to the previous conditions (ECR

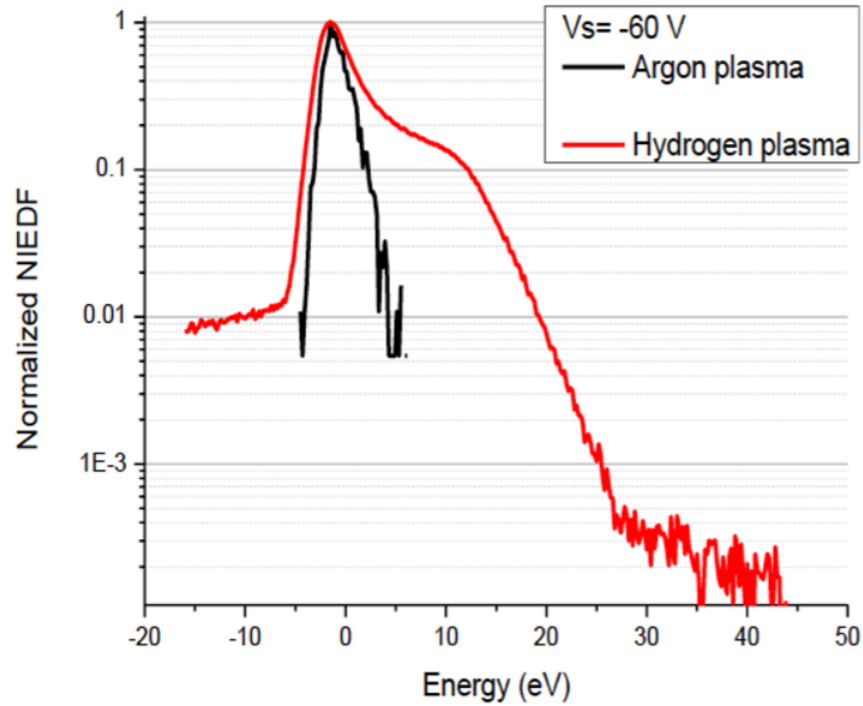


Figure 5.11: A comparison of normalised NIEDFs for the electrified sample immersed into an ECR driven plasma, following an initial 10 minute treatment within a hydrogen ECR plasma (1 Pa, 60 W, $V_s = -130$ V). The results from an argon plasma (shown in black, 0.1 Pa, 30 W, $V_s = -60$ V) are compared to a hydrogen plasma (shown in red, 1 Pa, 60 W, $V_s = -60$ V). Copyright (2018) The Japan Society of Applied Physics [1]

hydrogen plasma, 1 Pa, 60 W, $V_s = -130$ V) for 10 minutes in order to implant hydrogen into the surface. Following this, the material was baked at 500°C in order to remove the implanted hydrogen. Figure 5.12 compares the negative ion yield, and the maximum counts detected, post heating compared to a non-baked experiment. Post heating of the sample the negative ion yield was measured to be approximately 6 times lower than the non-baked experiment, showing clearly that baking the sample removes the adsorbed hydrogen.

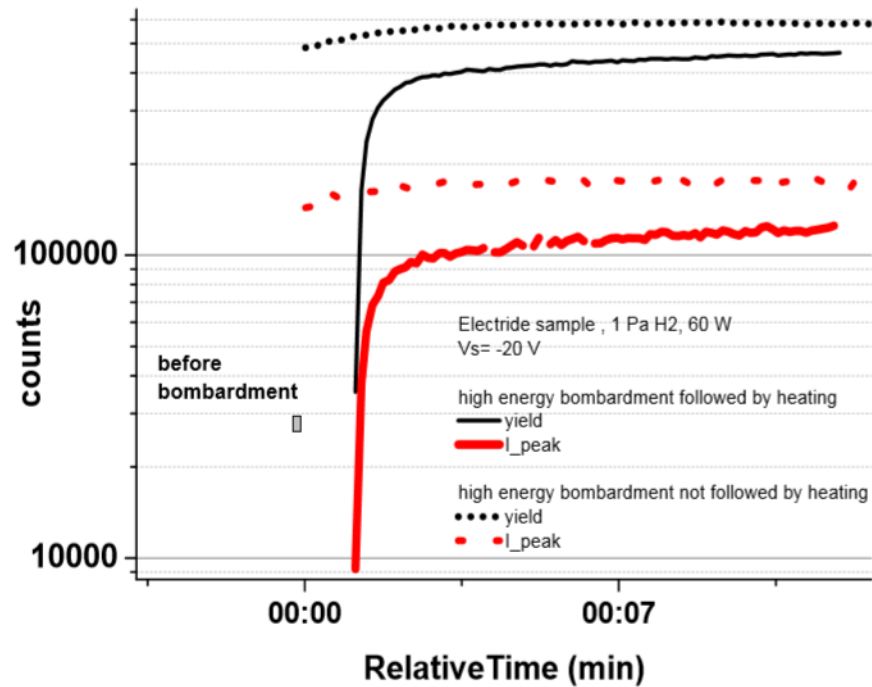


Figure 5.12: Time evolution of the negative ion yield after a high energy bombardment. Two results are shown, one follows the high energy bombardment with heating, the other shows the results of no applied heating following the pre-treatment. Copyright (2018) The Japan Society of Applied Physics [1]

5.4 Discussion

In a similar manner to the previous chapter, much of the discussion of the results is contained within the results sections. However, certain elements which require further discussion are contained within this section.

5.4.1 Nitrogen Doped Diamond Sample Creation

The creation of doped diamond films is a research field within its own right, and it would be beyond the scope of this thesis to discuss in detail. However, it is worth mentioning how the nitrogen doped diamond samples studied within this chapter were created. The NDD samples were created using a plasma enhanced chemical vapour deposition (PECVD) with a bell jar reactor operating at a pressure of 200 mbar, and an applied power (microwave) of 3 kW. The substrate was heated to 850°C and a methane concentration of 5 % was used, the films were deposited onto a (100) silicon wafer. The dopant levels stated within this chapter refer to the nitrogen content during the gas phase of their creation. However,

another PhD student, G. Smith, has conducted Raman spectroscopy to confirm an increase in the nitrogen content of the final films. This is consistent with previously published work, which has shown a link between the gas phase dopant level and the dopant level of the final sample [128].

The concentration of nitrogen in the gas phase during the growth of these NDD samples does not only influence the final nitrogen content of the diamond. It also effects the preference for which crystalline face will grow. As the nitrogen content is increased from 20 ppm to 50 ppm (and beyond to 100 ppm) the proportion of (111) crystalline faces increases. The crystal sizes in each of these three cases were similar at approximately 10 μm . A combination of the degree of doping and the crystalline face significantly effect the transport properties of the NDD samples [129]. In order to ascertain why the the 20 ppm NDD sample results in a larger yield than both the 50 and 100 ppm NDD samples is not trivial, and would likely require beam experiments in order to further understand the electronic properties of these samples.

5.4.2 Conductivity of nitrogen doped diamond

It has been previously reported that increasing nitrogen content in diamond films results in an increase of the electronic conductivity [130]. The explanation for this has been theoretically reported to be due to the preferential incorporation of nitrogen atoms into the grain boundaries [131], and subsequent conduction through these grain boundaries. However, it has been reported that there are likely other important factors which determine the conductivity of the films [132]. These observations of higher nitrogen content resulting in higher conductivity have been observed in the marked difference between the 50 and 100 ppm NDD samples investigated within this chapter; as the 50 ppm sample could not be biased at 400°C. The 20 ppm NDD sample was able to biased at 400°C, however, this may be due to the (100) crystalline face being preferentially grown. This is currently an active research area, for more information please see the following references [133, 134].

5.4.3 Comparison of negative ion yields to other surfaces

Directly comparing the negative ion yield between either the NDD or electrude samples to previous studies is not trivial for a number of a reasons. Firstly, all the measurements presented within this chapter are relative numbers, therefore, any variation in plasma conditions,

reactor design, sample holder, or sample size can make direct comparisons very difficult. Secondly, the temperature of the samples have been chosen to ensure that appropriate negative biases can be applied. Whilst this makes sense for individual materials, it can make direct comparisons between surfaces challenging. Finally, a number of major experimental changes have been conducted by the group since their work on HOPG [114], for example, a refined biasing procedure to correct transmission issues within the mass spectrometer, and a significant reduction in noise caused by the RF field on the mass spectrometer.

Whilst direct comparisons with previously published work may not be 100 % accurate, it is currently the best available option. Ahmad et. al. [78] reported a large scale comparison between multiple different surfaces for a large range of plasma conditions, which allows a rough comparison to be drawn. One of the results published was a NIEDF for a 100 W RF 2 Pa hydrogen plasma, for a boron doped diamond sample heated to 400°C. The maximum counts observed was approximately the same as the 100 ppm NDD sample discussed within this section (1×10^5 counts/s). The yields were not reported in the same way, however, without an accurate calculation of backscattering contributions this still may not have been valid.

This work has been continued by another PhD student from the University of York, G. Smith. They have conducted a direct comparison of the NDD samples (with a wider range of nitrogen doping), with both MCD and MCBDD. They have confirmed that at low biases ($V_s = -20$ V) the NDD results in a higher yield than either MCD or MCBDD. However, at higher biases ($V_s = -130$ V) the NDD samples perform significantly worse than MCBDD, and comparatively to MCD. Equally, they have confirmed the same conclusion as this work, namely, that higher nitrogen doping results in a higher yield; providing that the crystalline face, and crystal size, is unchanged.

The electrified sample yielded a similar yield and maximum counts to the 20 ppm NDD sample, however, major variations in the plasma conditions (RF vs ECR) limit a direct comparison. M. Sasao has future work planned with the group at PIIM to continue the investigation of the sample, with one of the aims being to directly compare to previously published materials. The electrified was directly compared to a molybdenum sample within this chapter, and produced a significantly higher yield. This higher yield may be attributed to the lower work function of electrified. However, the specific nano-structure of the electrified sample may facilitate the displacement of engaged electrons with H^- ions [135]. Further

work would be necessary in order to confirm the magnitude of this effect.

5.5 Chapter Summary

The nitrogen doped diamond results within this chapter clearly show an effect due to the dopant level or the crystalline face, or most likely, a combination of both. Due to the dependence of the concentration of nitrogen in the gas phase on the crystalline face it is not possible to de-convolute these two effects. It has also been shown that a higher magnitude of surface bias results in a small yield of negative ions, most likely due to the surface damage caused by highly energetic ionic species. However, this surface damage is reversible, although, it can take many hours in order to fully recover the original signal. The temperature dependence of the yield with the NDD samples was also investigated, and found to behave similar to previously investigated MCBDD samples, likely as a result of the changing sp^3/sp^2 ratio [78].

The electrified results presented within this chapter are a result of a collaboration with M. Sasao [1] and have shown a large yield of negative ions from this low (2.4 eV) work function material. The contribution due to sputtered hydrogen atoms has been confirmed and has been observed to be over an order of magnitude larger than a molybdenum sample.

Both of these materials may be viable replacements for current caesiated negative ion sources, however, a direct comparison to caesium is required in order to facilitate this comparison. This is a project which the PIIM group in Marseille are considering, however, there are many difficulties in handling caesium and furthermore, once caesium has been introduced to a vessel you cannot easily return to a non-caesiated environment. Prior to this, they are aiming to absolutely calibrate their mass spectrometer by using a magnetised retard field energy analyser as discussed by Rafalskyi *et. al* [136].

Chapter 6

Influence of the surface material upon the atomic hydrogen densities

6.1 Prelude

This Chapter presents atomic hydrogen density measurements within the GEC reference cell. These were taken in analogous conditions to those of Chapter 4 — *Influence of the surface material on the volume production of negative hydrogen ions*. To remind the reader, the surfaces investigated were: tungsten, stainless steel 304, copper, aluminium, and molybdenum. The measurements were conducted using TALIF, as has been previously discussed in Section 3.6, and the experimental set up was the same as described in Section 3.1: the GEC reference cell.

The TALIF measurements were conducted in a continuous operation mode, as opposed to the pulsed operation in which the H^- ion density measurements were conducted; this caused some heating of the installed samples. However, an experiment was conducted to measure the H density after different exposure times to the plasma. For example, a measurement at $t = 0$ was taken, then an additional measurement one hour later. This was observed to cause no difference in the atomic hydrogen density. The data points were within the error bars, likely due to the time-scale required to acquire each data point: approximately 40 minutes.

The measurements were conducted with the power being coupled to the 5-turn copper coil. However, the H densities presented within this chapter are measured within the E-mode (capacitive) regime. Some measurements were conducted in H-mode, but they are presented in Appendix A — *The E to H-mode Transition*.

These measurements were taken as the H densities were used to explain various trends observed within the H^- ion measurements of Chapter 4. For example, the creation of H^- ions via electron collisions with vibrationally excited molecules, which were produced due to the recombination of atomic hydrogen at the surface; as discussed in Section 2.9.2. Furthermore, the explanation of the pressure trends observed within Chapter 4 required measurements of how the H density varies with pressure.

Finally, the aim of measuring atomic hydrogen was to ultimately characterise the surface loss coefficients of atomic hydrogen. In Chapter 4 *Influence of the surface material on the volume production of negative hydrogen ions* it was shown that the surface does influence the production of H^- ions even in the absence of direct surface production of H^- ions. Unfortunately, a combination of time-constraints and significant alterations to the experimental reactor rendered the measuring of atomic loss coefficients impossible.

6.2 Power and Pressure Variations

This section focusses on the dependency of the H density on both the applied power and the pressure. Figure 6.1 shows the H density as a function of the applied power for the copper sample, at a pressure of 25 Pa. It can be observed that increasing power increases the H density. However, at power of 500 W and greater, the H density begins to plateau. The creation of atomic hydrogen is predominantly driven through electron impact dissociation, which requires the collision of an electron, with sufficient energy, and a hydrogen molecule. It has previously been shown, Figure 4.5, that electron density scales linearly with power, assuming no mode transition is observed. Therefore, it is logical that the H density would increase with the applied power. Unfortunately, the deviation from a linear increase is not necessarily straightforward. One explanation for this may be due to the increase in gas temperature with the applied power [137]. As the pressure and volume are fixed, then the number of molecules will decrease with the increasing temperature through the ideal gas law. This reduces the number of molecules available to dissociate, and may explain the observed plateau. An alternative, or complimentary, explanation may involve the production of γ electrons at the surface. These are high energy electrons, which may have energies that result in a low dissociation cross-section [138]. This can act to reduce the population of electrons with a more favourable electron energy for the dissociation process. A combination

of these two factors is the likely explanation for the observed trend with increasing power.

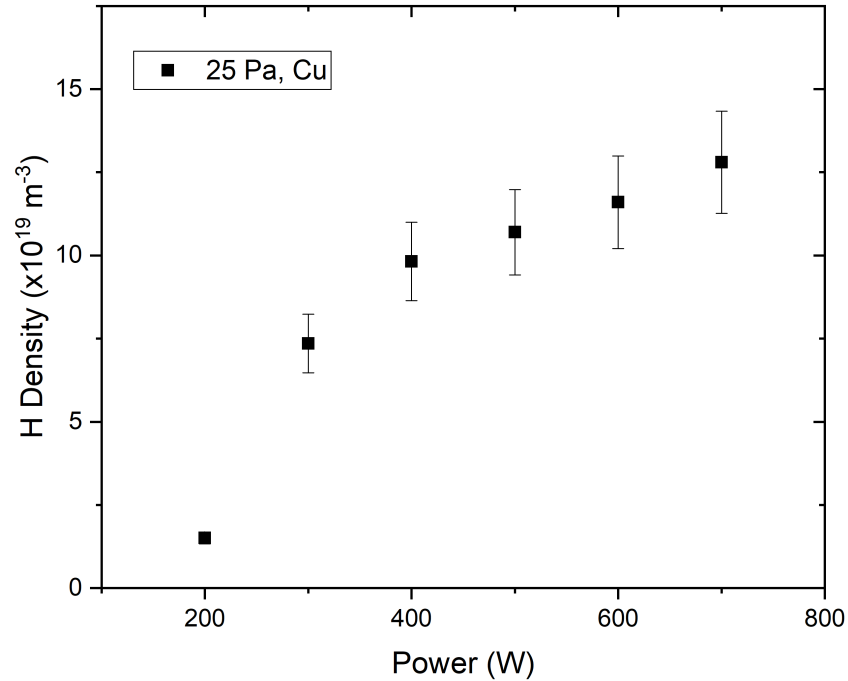


Figure 6.1: Atomic hydrogen density as a function of power for the copper sample, at a pressure of 25 Pa.

In Chapter 4 numerous results were presented to show how the H^- ion density varies with the applied power and pressure. The explanation for why the H^- ion densities decreased with increasing pressure, for a set power, was two-fold. Firstly, a consideration of the reduction of fast electrons, that are necessary for the E-V excitation process, and secondly, the effect of V-t relaxation. It was proposed that the difference in the H^- ion densities between pressures may be dependent on the atomic hydrogen density. This is because, if the H density increased with pressure, then more vibrationally excited species would be destroyed through the V-t relaxation pathway. Figures 6.2 and 6.3 show the H density as a function of power for three different pressures, 20, 25, and 30 Pa. Figure 6.2 shows the results for the copper sample, whereas, Figure 6.3 used the stainless steel sample. In both instances, we can observe that increasing the pressure increases the H density. Furthermore, the same trend, whereby the H density increases with the applied power, can be observed for all pressures in both Figure 6.2 and 6.3.

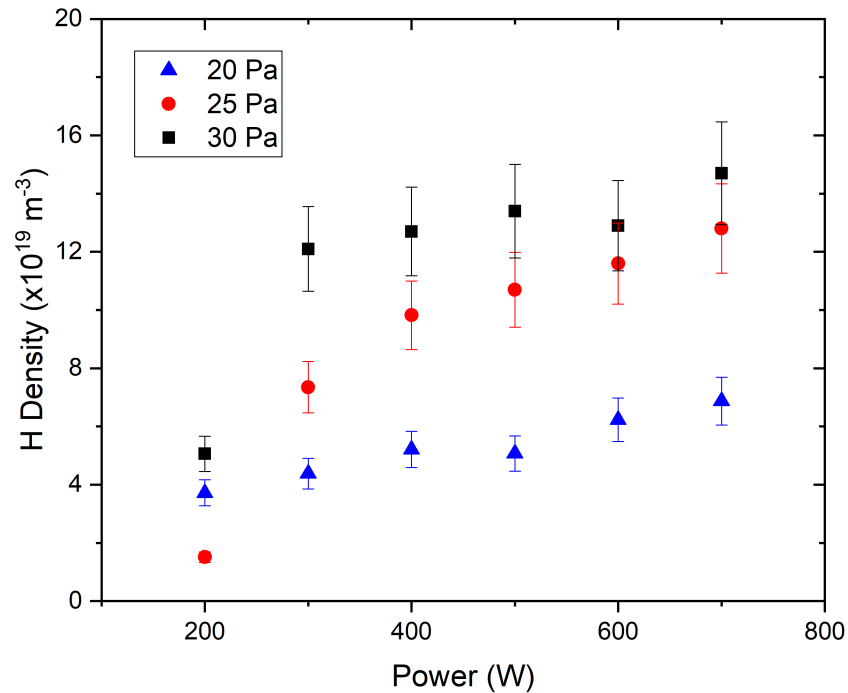


Figure 6.2: Atomic hydrogen density as a function of power for the copper sample, at three pressures: 20, 25, and 30 Pa.

The explanation as to why the H density increases with pressure is not straightforward, and depends on many interlinking parameters. Firstly, as the pressure increases, for a constant volume and temperature, the number of molecules will increase. Equally, the electron density increases with pressure, this means that more electron-molecule collisions can occur, which may result in dissociation. Secondly, as the pressure is increased the number of collisions rises. This acts to reduce the electron temperature; as measured in Chapter 4 with the Langmuir Probe. This reduces the number of electrons with the available energy to cause dissociation. It is also important to consider the destruction of atomic hydrogen; this is primarily due to interactions with the wall [24]. The motion of atomic hydrogen is due to diffusion, where an increase in pressure results in an increase in collisions, which acts to decrease the surface loss probability [139]. Due to the complexity of all of these factors, and others which have been discounted due to their more marginal effects, it is very difficult to know how the density would vary with pressure without performing a measurement.

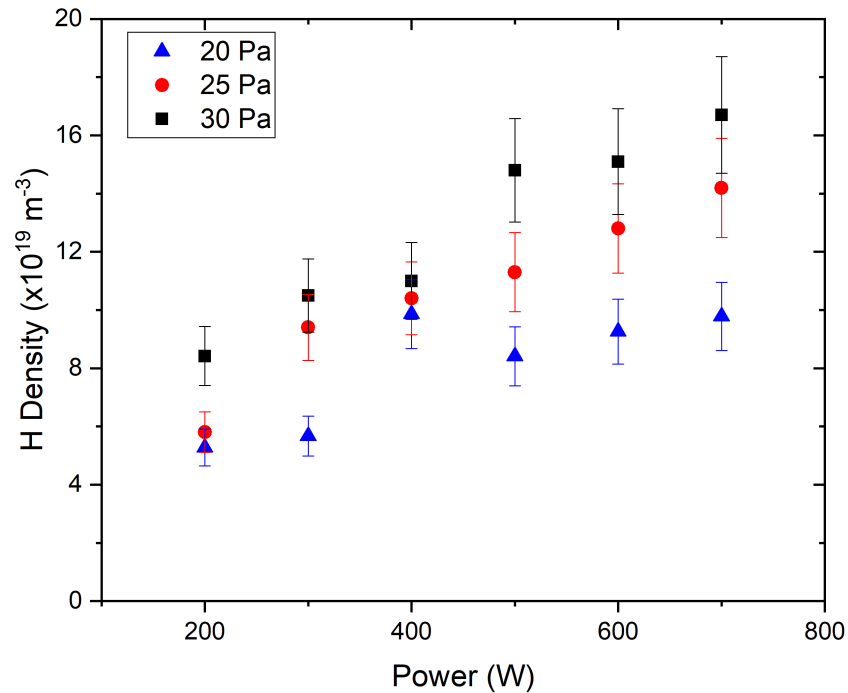


Figure 6.3: Atomic hydrogen density as a function of power, for the steel sample, at three pressures: 20, 25, and 30 Pa.

6.3 Surface Variations

One of the aims of this chapter was to investigate how the atomic hydrogen densities varied as a function of power for the different metallic surfaces. Figure 6.4 shows these results for a pressure of 25 Pa and powers between 200–700 W. With the exception of the 500 W aluminium data point (blue triangle), the density increases with power for all the surface investigated. Unfortunately, the variation between the surfaces is not easy to interpret. Stainless steel, copper (excluding the 200 W data point), and aluminium (excluding the 500 W data point), are all within error. In contrast, molybdenum and tungsten consistently result in the lowest H density, excluding the 200 W copper data point, and are within error.

It is possible to speculate as to what the cause of these discrepancies may be. For example, stainless steel and copper are reported to have a similar surface loss coefficient [111]. However, a full set of surface loss measurements should be conducted under identical experimental conditions in order to fully characterise these materials. This may lend additional evidence to the hypothesis that the measured H^- ion densities were due to the creation

of vibrationally excited hydrogen molecules, facilitated by the presence of weak binding sites [103]. Unfortunately, time constraints did not make this possible during this project.

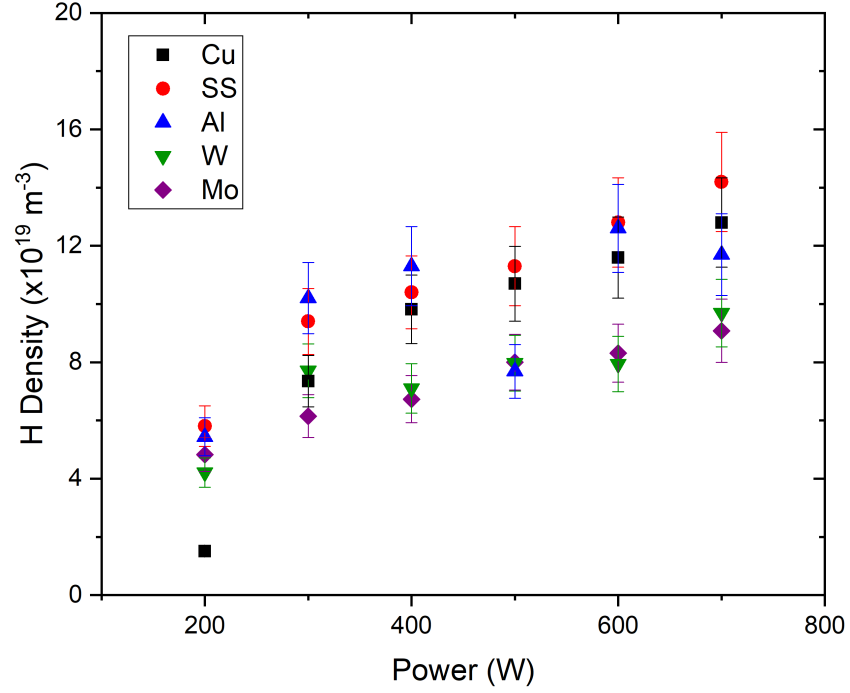


Figure 6.4: Atomic hydrogen density as a function of power for five different surfaces, including: tungsten, stainless steel 304, copper, aluminium, and molybdenum, at a gas pressure of 25 Pa.

6.4 Discussion

6.4.1 Comparison to Literature

Abosolute atomic hydrogen densities have been previously measured in a similar experimental set up by Abdel-Rahman *et. al.* [140]. The majority of their measurements were conducted within H-mode, from which some comparisons can be drawn in Appendix A. They reported a H density of 4×10^{19} – 3.5×10^{20} m^{-3} for applied powers of 100–400 W at a gas pressure of 15 Pa. They also observed a large increase in the atomic hydrogen density, between 100–150 W, as the transition to H-mode began. Whilst it is difficult to draw direct comparisons, this range is similar to the one that has been presented within this chapter.

6.4.2 Surface Loss Coefficients

The surface loss coefficients for these materials have already been presented and discussed in Section 4.6.2 [111]. They reported a similar surface loss rate for both copper and stainless steel, which would match the observation from Figure 6.4 in which steel and copper had the largest atomic hydrogen densities. Sode *et. al.* also reported that tungsten's surface loss rate was twice as small as steel, and aluminium five times smaller [111]. However, it has been observed that the atomic hydrogen density in tungsten is smaller than that of copper and steel, and that the H density is substantially larger with the aluminium sample. Unfortunately, such comparisons between surface loss rates and absolute densities are not straightforward, and as such, surface loss coefficient measurements should be conducted to further develop this work.

6.5 Chapter Summary

The results presented within this chapter confirm a dependency of the atomic hydrogen density on both the power and the pressure. Whilst the dependence on power was easily predictable, the pressure dependency can be quite complex and was necessary to confirm due to the effect of atomic hydrogen on the vibrationally excited molecules of hydrogen. It was observed in Chapter 4 that the H^- ion density decreases with increasing pressure. Subsequently, it was proposed that if the atomic hydrogen density increases with pressure, then additional V-t relaxation events could be limiting the production of H^- ions.

A dependency of the atomic hydrogen density, due to the surface material, was also observed, with stainless steel, aluminium, and copper resulting in the highest densities. Whilst, it has been reported that the surface loss coefficients for steel and copper are similar, the surface loss rate for aluminium should be five times smaller [111]. In the work presented here, the atomic hydrogen density above the aluminium surface resulted in a similar density to that of the copper and steel surface. Unfortunately, comparing the measured atomic hydrogen densities to surface loss rates is not necessarily accurate. Therefore, for a true comparison, surface loss measurements would be required for this experimental setup.

Measuring the surface loss rate coefficients for atomic hydrogen would also be an important step towards quantifying the production of H^- ions. This would also require a measure of the vibrational temperature, feasibly by using Fulcher spectroscopy, as this would allow

a measurement of the vibrational temperature in the vicinity of each surface. By combining the measurements of the fraction of atomic hydrogen lost to a surface, surface loss coefficients, the vibrational temperature changes observed due to different surfaces and the H^- ion measurements a full quantifiable model could be created. This could be combined with the chemical reactions and cross-sections presented in Section 2.8 *Volume production of Negative Hydrogen Ions H^-* to create a full model of the production, and destruction, of H^- ions.

Chapter 7

Conclusions

The focus of this study has been to investigate the role of surface produced, and surface assisted, negative hydrogen ion generation within low pressure, low temperature, radio-frequency plasmas. Ultimately, the aim was to answer the question: *How does the negative hydrogen ion density depend on the surface material?*

In Chapter 4, laser photodetachment was used to investigate the influence of the surface material on the volume production of negative hydrogen ions. All of the surfaces that were investigated, tungsten, stainless steel 304, copper, aluminium, and molybdenum, had large work functions, approximately 5 eV. The observed dependencies of the H^- ion densities on the surface material were compared to the published work functions and no clear trend was observed. It was observed that the measured H^- ion densities were higher when the tungsten or stainless steel surfaces were installed. The other three materials, copper, aluminium, and molybdenum, exhibited similar quantitative and qualitative trends in the H^- ion density to one another. Phase resolved optical emission spectroscopy (PROES) was used to exclude the possibility of discrepancies in the secondary electron emission coefficient, which could have caused the observed trends. An explanation for the observations was proposed based on the recombination of atomic hydrogen at the surface through the *Hot Atom* recombination process [39]. This recombination mechanism creates vibrationally excited molecular hydrogen, which can undergo dissociative attachment in the bulk plasma to form H^- ions. It had previously been reported that the use of a tungsten surface resulted in a higher vibrational temperature compared to a copper surface [103]. As was observed within this thesis, this in turn facilitated a higher H^- ion density.

The H^- ion density was observed to exhibit different trends when the pressure was var-

ied, depending on which metallic surface was installed. The pressure dependency was more pronounced with the tungsten and stainless steel samples than with the copper, aluminium, or molybdenum samples. It was proposed that the V-t relaxation – relaxation due to collisions between vibrationally excited species and atoms – of the surface produced vibrationally excited molecular hydrogen may explain the observed trends. In order to investigate this hypothesis, the atomic hydrogen densities were measured by two-photon absorption laser induced fluorescence (TALIF). These were taken under the analogous conditions as for the aforementioned H^- ion density measurements. An increase in the atomic hydrogen density with increasing pressure was observed. This evidenced the previous claim of a reduction in the H^- ion density at higher pressures due to an increase in V-t relaxation.

The variation of the atomic hydrogen densities due to the surface was also investigated. It was observed that stainless steel, copper, and aluminium resulted in the largest atomic hydrogen density, with molybdenum and tungsten consistently being the lowest. At this time, no explanation is available to explain these measurements. However, further investigations should focus on measuring the surface loss coefficients using TALIF. This would allow a more direct comparison between the H^- ion densities and the atomic hydrogen densities for the different surfaces.

Negative ions are produced through two mechanisms, either volume production or surface production. It may seem obvious that the surface would have a large influence on the direct surface production of negative ions, however, it is less obvious that the volume process would be heavily influenced by the surface. Nevertheless, the results obtained during this investigation directly show an influence of the surface on the volume produced negative ions. There are many ways in which this work could be expanded, but the most logical would be through the use of Fulcher spectroscopy to measure the vibrational temperature. This would allow a direct comparison between the H^- ion density, atomic hydrogen density, and the vibrational temperature above different surface materials.

It has been discussed how the surface can affect the volume production of H^- ions, nevertheless, this is only one half of the proposed question. The other mechanism to be investigated is the direct surface production of H^- ions, which has a more obvious dependency on the surface material. Alternatives to caesiated metallic surfaces, often molybdenum or tungsten, are of considerable interest for their use in neutral beam injection. Two possible alternatives were investigated in Chapter 5 — *An investigation of direct surface production*

of negative ions from novel surfaces.

The surface production of negative ions from nitrogen doped diamond samples was investigated for the first time through the use of EQP mass spectrometry. It was observed to produce a comparable yield, defined as the area under the negative ion energy distribution function, as the previously highest performing non-caesiated surface, boron doped diamond. It has previously been observed that for boron doped diamond, the level of boron doping did not influence the negative ion yield. By contrast, a substantial influence of the concentration of nitrogen doping was observed. Unfortunately, due to the preferential formation of specific crystalline faces at certain nitrogen doping concentration, it is not possible to deconvolute the affect of the nitrogen doping and the crystalline face. Nitrogen doped diamond samples, regardless of the dopant level, were observed to have the same temperature dependency as boron doped diamond, which is attributed to the change in the sp^3/sp^2 ratio. The nitrogen doped diamond samples were also observed to be particularly susceptible to surface damage; it was observed that high energy positive ion bombardment substantially lowered the negative ion yield. However, it was also observed that the negative ion yield could be recovered in time as the surface repaired defects.

The negative ion yield of a nanoporous $12CaO\ 7Al_2O_3$ (C12A7) electride was also investigated for the first time. This material has been reported to have a work function of 2.4 eV [44], which is comparable to that of caesiated metallic surfaces. These are conventionally used to produce a large density of negative ions. It was confirmed that the production mechanisms for H^- and D^- ions are the same as those for diamond samples, namely, sputtering and backscattering. The negative ion yield was compared to that of molybdenum, and was found to be an order of magnitude higher. Finally, it was confirmed that a substantial portion of the measured H^- yield was due to the adsorbed hydrogen content. A logical continuation of this work would be to facilitate a direct comparison to caesiated metallic surfaces. This is a project that the group at PIIM in Marseille are currently considering. Unfortunately, the use of caesium is not straightforward and can permanently limit future experimental campaigns. Furthermore, they are aiming to absolutely calibrate their mass spectrometer which would allow wider direct comparisons to other diagnostic methods, i.e. photodetachment, and other plasma sources, such as the GEC reference cell.

The original research question of this work was: *How does the negative hydrogen ion density depend on the surface material?* In an attempt to answer this question, the direct

surface production of negative ions from novel surfaces has been investigated and mechanisms for the creation of the ions proposed. Furthermore, surface assisted volume production of H^- ions has been observed for certain metallic surfaces and an explanation for this process has been presented. Equally, atomic hydrogen densities were measured through the use of TALIF in order to evidence specific claims regarding the dependency of the H^- ion density on the pressure.

In conclusion, a deeper understanding of the direct surface production of H^- ions has been presented by investigating previously unmeasured surfaces. There is a clear need to find alternatives to caesiated metallic surfaces for their use in neutral beam injection and both nitrogen doped diamond, and the electride sample, are interesting possible alternatives. However, further investigation is required in order to facilitate a direct comparison to caesium. Finally, it was observed that certain metallic surfaces can assist the volume production of negative ions. Whilst metallic surfaces alone are insufficient for negative ion sources, other samples may also enhance the volume production of H^- ions, whilst simultaneously being effective at producing H^- ions directly from the surface.

Chapter 8

Appendix A – The E to H-mode Transition

As has previously been discussed, inductively coupled plasmas have two modes of operation, E-mode (capacitive) and H-mode (inductive). The majority of the previous data presented within this thesis was taken within E-mode. This was done as the H^- measurements were unable to be acquired during the inductive mode, as the probe tip was unable to withstand the temperature to accurately record the current measurements. However, the atomic hydrogen density measurements were not limited by the mode transition, and may prove interesting for comparison with future measurements of the H^- ion density. Furthermore, in Section 6.4.1, the absolute atomic hydrogen densities were compared to previously published data, and a measurement both before the H-mode transition and afterwards facilitates an easier comparison.

This appendix presents absolute atomic hydrogen density measurements in both E-mode and H-mode. Unfortunately, the comparison to H^- densities cannot be made, however, they present some interesting trends which are supported by previously published literature.

8.1 Results

Figure 8.1 shows the effective lifetimes as a function of power for the tungsten surface, at a pressure of 25 Pa. The H-mode transition can be observed as the sudden increase in the effective lifetime at 800 W. This increase in the effective lifetime can be explained by considering the gas temperature, which increases considerably across the E-H transition [137].

This results in fewer molecules of H_2 , through the ideal gas law, and thus less quenching partners. However, it is worth mentioning that it is not quite that straightforward, as an increase in temperature also causes an increase in the number of collisions, which causes more quenching. The variation in the effective lifetime during E-mode (200–750 W) is very slight, hence why effective lifetime measurements were not displayed in Chapter 6.

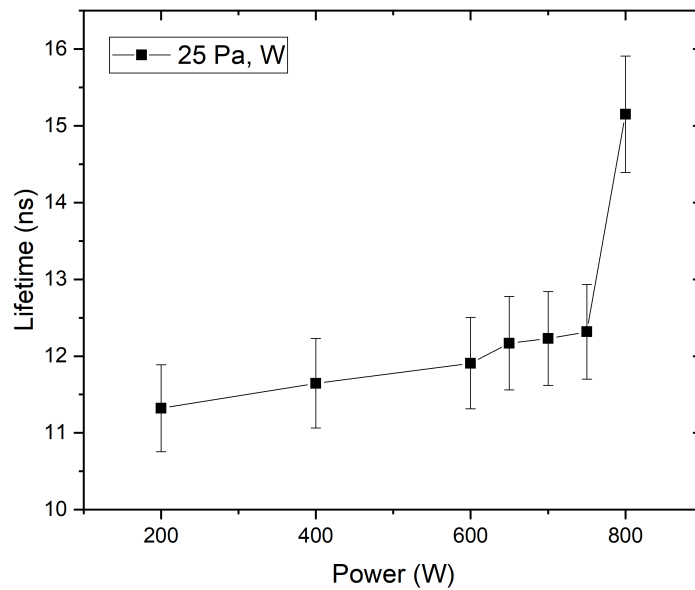


Figure 8.1: The effective lifetime as a function of applied power for the tungsten surface, at a pressure of 25 Pa. The H-mode transition occurs at 800 W.

Figure 8.2 shows the H density as a function of power for the tungsten surface, at a pressure of 25 Pa. The increase in the H density throughout E-mode follows a similar trend to that discussed in Chapter 6, however, the density is increased by almost a factor of 5 across the E-H mode transition. This is due to the large increase in the electron density [141], which causes additional dissociation events and a large increase in the H density.

Figures 8.3–8.5 show the phase resolved excitation structures for the tungsten sample, at a gas pressure of 25 Pa. The applied powers are 200, 750, and 950 W for Figures 8.3, 8.4, and 8.5 respectively. Figure 8.3 shows one primary excitation structure due to sheath expansion. As the power is increased, a second excitation structure becomes visible; this is shown by Figure 8.4. This second mechanism occurs because of the affect of the secondary electron emission from the surface. As the applied power is further increased, the transition to H-

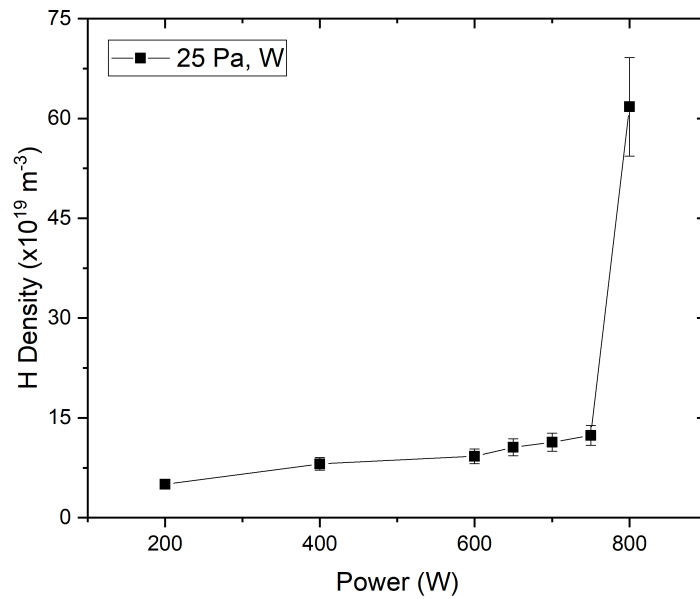


Figure 8.2: Atomic hydrogen density as a function of power for the tungsten surface, at a pressure of 25 Pa. The H-mode transition occurs at 800 W.

mode occurs. This can be observed in Figure 8.5 as two characteristic excitation structures, due to the currents within the discharge being induced twice per RF-cycle [137].

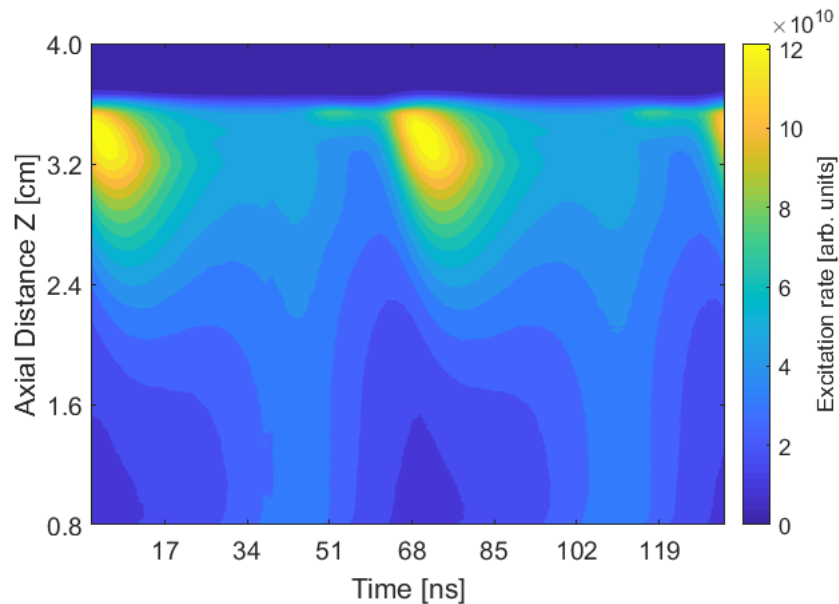


Figure 8.3: Excitation structure as measured by PROES. The plasma operated at 25 Pa with an applied power of 200 W. One main heating mechanism is observable at the power, likely due to sheath expansion.

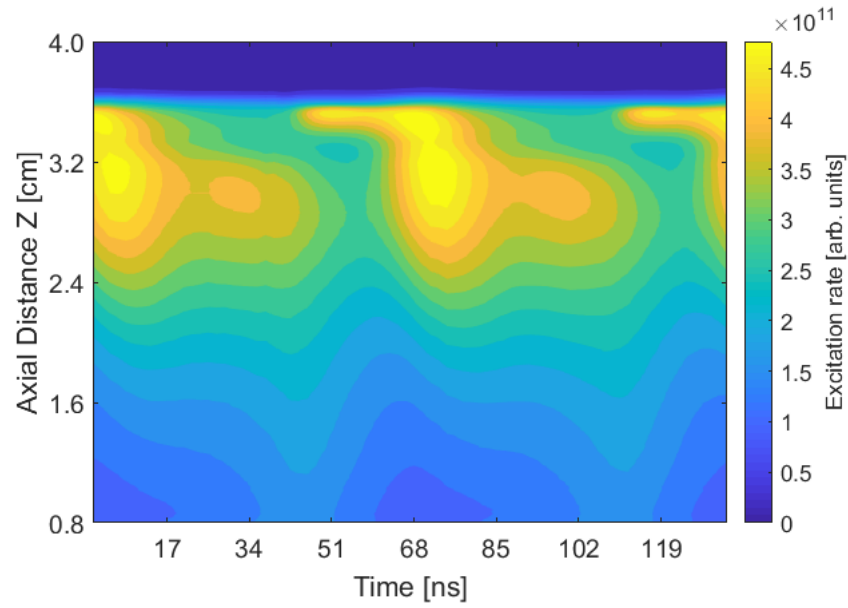


Figure 8.4: Excitation structure as measured by PROES. The plasma operated at 25 Pa with an applied power of 750 W, just prior the H-mode transition. Two heating mechanisms can be observed here, one due to sheath expansion (as seen at 200 W), and another due to the γ electrons.

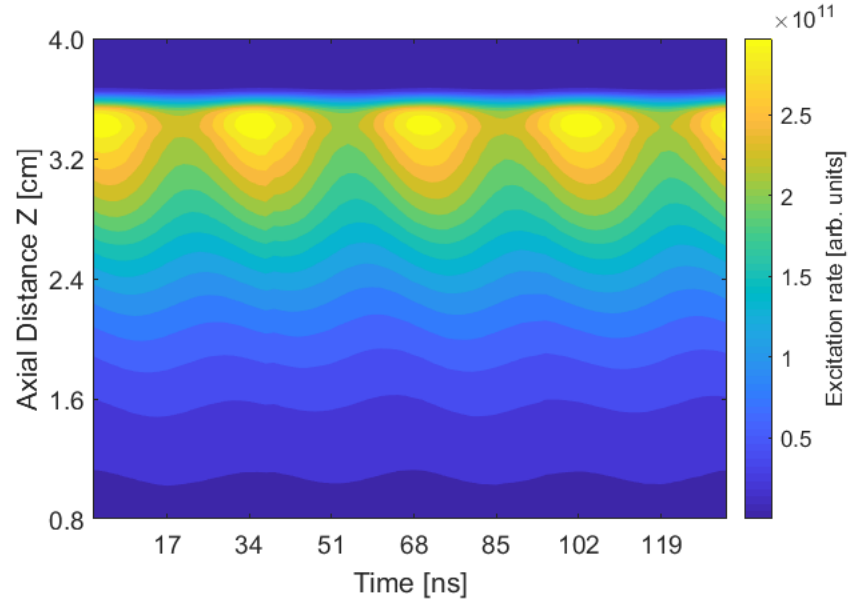


Figure 8.5: Excitation structure as measured by PROES. The plasma operated at 25 Pa with an applied power of 950 W, after the H-mode transition. Two excitation structures can be observed per RF-cycle, this is characteristic of H-mode and is due to the currents within the discharge being induced twice per RF-cycle.

Figure 8.6 shows the H density as a function of power for the tungsten surface, at a

pressure of 30 Pa. As with Figure 8.2, the H density trend within E-mode is similar to those discussed previously. However, a minor variation from this may be seen just prior to the H-mode transition at 900 W. Additional measurements are necessary in order to confirm whether this is a real effect, or a product of too few data points within the transition region. Measurements within this region are challenging as the temperature of the vessel increases substantially, which causes a change in the H-mode transition point. In contrast to Figure 8.2, the H-mode transition occurs at approximately 1000 W, which is higher than the transition point in the 25 Pa case. The H-mode transition has previously been observed to be pressure dependent [140].

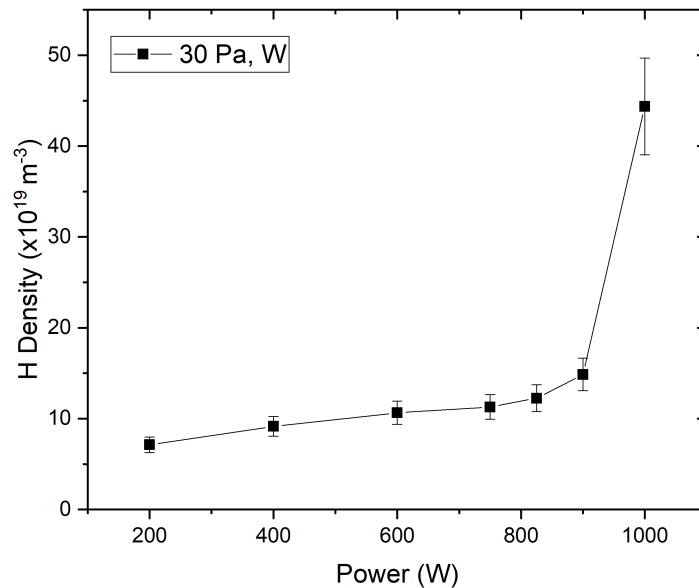


Figure 8.6: Atomic hydrogen density as a function of power for the tungsten surface, at a pressure of 30 Pa. The H-mode transition occurs at 1000 W.

Figure 8.7 shows the H density as a function of power for the tungsten surface, at a pressure of 15 Pa. Interestingly, no H-mode transition is observed at this pressure, although the maximum possible applied power in the experimental setup is 1000 W. It was observed that decreasing the pressure from 30 Pa, Figure 8.6, to 25 Pa, Figure 8.2, caused the H-mode transition to happen at a lower power. Interestingly, when the pressure is reduced further, the transition does not occur. This has previously been reported in an argon plasma by Lee *et. al.*. One possible explanation may be that this is due to the efficiency of electron heat-

ing, when the electron-neutral collision frequency matches the driving frequency. However, further study is required in order to understand this phenomenon.

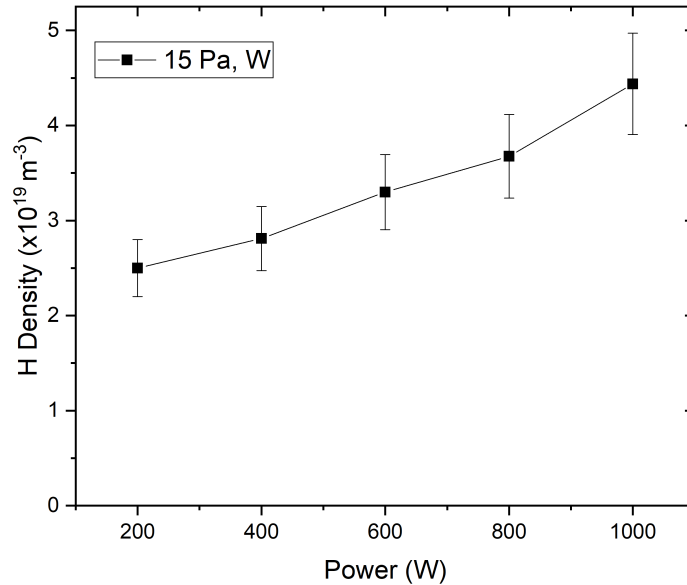


Figure 8.7: Atomic hydrogen density as a function of power for the tungsten surface, at a pressure of 15 Pa. No H-mode transition is observed at this pressure.

8.2 Discussion

As with the previous chapters, much of the discussion is contained alongside the presented results, however, areas which require explicit consideration are discussed here.

8.2.1 Dependency of the Surface on the H-mode Transition

One of the aims of this work was to investigate whether the different surface materials had an effect on the power required for the H-mode transition. It was initially observed that this was the case. However, as has been previously mentioned, the time-scale required to acquire atomic hydrogen densities is approximately 40 minutes. In this time, thermal drifts were substantial, and these have been observed to have an affect on the required power for the transition. In order to confirm whether the required power for the H-mode transition is surface dependent, pulsed measurements should be taken, as this will reduce the thermal

loading on the vessel. Alternatively, if pulsed PROES measurements could be acquired, this would also confirm this effect.

8.3 Appendix Summary

The results presented within this appendix show a large increase in the atomic hydrogen density across the E-H mode transition, with a factor increase of up to 5-fold. A H-mode transition was observed at 1000 W at 30 Pa and 800 W at 25 Pa. However, no transition was observed within 1000 W for the 15 Pa measurements. This confirms a non-trivial dependence of the H-mode transition with pressure, which has previously been observed for an argon plasma by Lee *et. al.* [141], and shows that a minimum applied power can be found by conducting a pressure variation. The surface was also observed to affect the power requirement for the H-mode transition. Unfortunately, due to the time-scales required to acquire data, the thermal fluctuations had a greater effect. Future experiments should focus on using TALIF in a pulse operational mode to circumnavigate this problem.

List of References

- [1] M. Sasao, R. Moussaoui, D. Kogut, J. Ellis, G. Cartry, M. Wada, K. Tsumori, and H. Hosono. Negative-hydrogen-ion production from a nanoporous $12\text{CaO} \cdot 7\text{Al}_2\text{O}_3$ electride surface. *Applied Physics Express*, 11(6):066201, 2018.
- [2] G. J. Smith, J. Ellis, R. Moussaoui, C. Pardanaud, C. Martin, J. Achard, R. Issaoui, T. Gans, J. P. Dedrick, and G. Cartry. Enhancing surface production of negative ions using nitrogen doped diamond in a deuterium plasma. *Journal of Physics D: Applied Physics*, 53(46):465204, 2020.
- [3] J. Ellis, J. Branson, K. Niemi, E. Wagenaars, and T. Gans. Influence of surface materials on the volume production of negative ions in a radio-frequency driven hydrogen plasma. *Journal of Physics D: Applied Physics*, 53(48):485202, 2020.
- [4] M. Lieberman and A. Lichtenberg. *Principles of Plasma Discharges and Materials Processing*. John Wiley and Sons, 111 River Street, Hoboken, NJ 07030 (201) 748-6011, 2005.
- [5] T. Wegner, C. Küllig, and J. Meichsner. On the E-H transition in inductively coupled radio frequency oxygen plasmas: I. density and temperature of electrons, ground state and singlet metastable molecular oxygen. *Plasma Sources Science and Technology*, 26(2):025006, 2017.
- [6] J. Hopwood. Review of inductively coupled plasmas for plasma processing. *Plasma Sources Science and Technology*, 1(2):109, 1992.
- [7] D. J. MacKay. *Sustainable Energy - without the hot air*. UIT Cambridge, PO Box 145, Cambridge, CB41GQ, England, 2009.

- [8] K. Tokimatsu, J. Fujino, S. Konishi, Y. Ogawa, and K. Yamaji. Role of nuclear fusion in future energy systems and the environment under future uncertainties. *Energy Policy*, 31(8):775 , 2003.
- [9] R. Toschi. Nuclear fusion, an energy source. *Fusion Engineering and Design*, 36(1):1, 1997.
- [10] S. Fetter, E. Cheng, and F. Mann. Long-term radioactivity in fusion reactors. *Fusion Engineering and Design*, 6:123, 1988.
- [11] S. Fetter, E. Cheng, and F. Mann. Long-term radioactive waste from fusion reactors: Part II. *Fusion Engineering and Design*, 13(2):239 , 1990.
- [12] J.-L. Boutard, A. Alamo, R. Lindau, and M. Rieth. Fissile core and tritium-breeding blanket: structural materials and their requirements. *Comptes Rendus Physique*, 9(3):287 , 2008. Materials subjected to fast neutron irradiation.
- [13] I. Chapman, et al. Power requirements for electron cyclotron current drive and ion cyclotron resonance heating for sawtooth control in ITER. *Nuclear Fusion*, 53(6):066001, 2013.
- [14] D. Čirić, et al. Overview of the JET neutral beam enhancement project. *Fusion Engineering and Design*, 82(5):610 , 2007. Proceedings of the 24th Symposium on Fusion Technology.
- [15] M. Nicassio. Introduction to neutral beam injection technology. In *York's Fusion Technology*. University of York, 2020.
- [16] E. Surrey, C. Challis, D. Ciric, S. Cox, B. Crowley, I. Jenkins, T. Jones, and D. Keeling. Measurement of the depletion of neutraliser target due to gas heating in the JET neutral beam injection system. *Fusion Engineering and Design*, 73(2):141 , 2005.
- [17] K. Berkner, R. Pyle, and J. Stearns. Intense, mixed-energy hydrogen beams for CTR injection. *Nuclear Fusion*, 15(2):249, 1975.
- [18] U. Fantz, P. Franzen, and D. Wunderlich. Development of negative hydrogen ion sources for fusion: Experiments and modelling. *Chemical Physics*, 398:7 , 2012. Chemical Physics of Low-Temperature Plasmas (in honour of Prof Mario Capitelli).

- [19] B. Heinemann, et al. Design of the “half-size” iter neutral beam source for the test facility elise. *Fusion Engineering and Design*, 84(2):915 , 2009. Proceeding of the 25th Symposium on Fusion Technology.
- [20] U. Fantz, et al. Negative ion RF sources for ITER NBI: status of the development and recent achievements. *Plasma Physics and Controlled Fusion*, 49(12B):B563, 2007.
- [21] L. Schiesko, P. McNeely, U. Fantz, and P. F. and. Caesium influence on plasma parameters and source performance during conditioning of the prototype ITER neutral beam injector negative ion source. *Plasma Physics and Controlled Fusion*, 53(8):085029, 2011.
- [22] C. Barnett, J. Ray, E. Ricci, M. Wilker, E. McDaniel, E. Thomas, and H. Gilbody. Atomic data for controlled fusion research, 1977.
- [23] M. Bacal and M. Wada. Negative hydrogen ion production mechanisms. *Applied Physics Reviews*, 2(2):021305, 2015.
- [24] P. Berlemont, D. A. Skinner, and M. Bacal. Negative ion volume production model: State of the experimental confirmation. *Review of Scientific Instruments*, 64(10):2721, 1993.
- [25] J. R. Hiskes. Cross sections for the vibrational excitation of the $H_2 X^1 \sum^+_{g(v)}$ levels generated by electron collisional excitation of the higher singlet states. *Journal of Applied Physics*, 70(7):3409, 1991.
- [26] J. R. Hiskes. Electron excitation of $H_2 (v')$ levels to yield vibrationally excited H_2 molecules. *AIP Conference Proceedings*, 158(1):34, 1987.
- [27] J. R. Hiskes and A. M. Karo. Generation of negative ions in tandem high-density hydrogen discharges. *Journal of Applied Physics*, 56(7):1927, 1984.
- [28] M. Cacciatore, M. Capitelli, and C. Gorse. Non-equilibrium ionisation of molecular hydrogen in electrical discharges. *Journal of Physics D: Applied Physics*, 13(4):575, 1980.
- [29] D. T. Stibbe and J. Tennyson. Near-threshold electron impact dissociation of H_2 within the adiabatic nuclei approximation. *New Journal of Physics*, 1:2, 1999.

- [30] A. A. Matveyev and V. P. Silakov. Kinetic processes in a highly-ionized non-equilibrium hydrogen plasma. *Plasma Sources Science and Technology*, 4(4):606, 1995.
- [31] B. M. Smirnov. Atomic structure and the resonant charge exchange process. *Physics-Uspekhi*, 44(3):221, 2001.
- [32] D. S. Walton, B. Peart, and K. T. Dolder. A measurement of cross sections for detachment from H-by a method employing inclined ion and electron beams. *Journal of Physics B: Atomic and Molecular Physics*, 4(10):1343, 1971.
- [33] B. Peart, D. S. Walton, and K. T. Dolder. *Journal of Physics B: Atomic and Molecular Physics*, 3(10):1346, 1970.
- [34] J. R. Hiskes, A. M. Karo, and P. A. Willmann. Hydrogen vibrational population distributions and negative ion generation in tandem high density hydrogen discharges. *Journal of Vacuum Science & Technology A*, 3(3):1229, 1985.
- [35] J. R. Hiskes and A. M. Karo. Recombination and dissociation of H_2^+ and H_3^+ ions on surfaces to form $h_2(v')$: Negative-ion formation on low-work-function surfaces. *Journal of Applied Physics*, 67(11):6621, 1990.
- [36] K. Christmann. Interaction of hydrogen with solid surfaces. *Surface Science Reports*, 9(1):1, 1988.
- [37] C. T. Rettner. Reaction of an H atom beam with Cl/Au(111): Dynamics of concurrent Eley–Rideal and Langmuir–Hinshelwood mechanisms. *The Journal of Chemical Physics*, 101(2):1529, 1994.
- [38] S. Caratzoulas, B. Jackson, and M. Persson. Eley–Rideal and hot-atom reaction dynamics of H(g) with H adsorbed on Cu(111). *The Journal of Chemical Physics*, 107(16):6420, 1997.
- [39] J. Harris and B. Kasemo. On precursor mechanisms for surface reactions. *Surface Science Letters*, 105(2):L281, 1981.
- [40] T. Kammler and J. Küppers. Interaction of (h) atoms with Cu(111) surfaces: Adsorption, absorption, and abstraction. *The Journal of Chemical Physics*, 111(17):8115, 1999.

- [41] T. Kammler, D. Kolovos-Vellianitis, and J. Küppers. A hot-atom reaction kinetic model for H abstraction from solid surfaces. *Surface Science*, 460(1):91 , 2000.
- [42] R. I. Hall, I. Čadež, M. Landau, F. Pichou, and C. Schermann. Vibrational excitation of hydrogen via recombinative desorption of atomic hydrogen gas on a metal surface. *Phys. Rev. Lett.*, 60:337, 1988.
- [43] P. J. Eenshuistra, R. M. A. Heeren, A. W. Kleyn, and H. J. Hopman. Dissociation and vibrational excitation of H₂ molecules and wall influence on the densities in a multicusp ion source. *Phys. Rev. A*, 40:3613, 1989.
- [44] Y. Toda, H. Yanagi, E. Ikenaga, J. Kim, M. Kobata, S. Ueda, T. Kamiya, M. Hirano, K. Kobayashi, and H. Hosono. Work function of a room-temperature, stable electride [Ca₂₄Al₂₈O₆₄]⁴⁺(e⁻)₄. *Advanced Materials*, 19(21):3564, 2007.
- [45] M. Maazouz, A. G. Borisov, V. A. Esaulov, J. P. Gauyacq, L. Guillemot, S. Lacombe, and D. Teillet-Billy. Effect of metal band characteristics on resonant electron capture: H⁻ formation in the scattering of hydrogen ions on Mg, Al, and Ag surfaces. *Phys. Rev. B*, 55:13869, 1997.
- [46] A. Borisov, D. Teillet-Billy, and J. Gauyacq. H formation by electron capture in hydrogen-Al(111) collisions: perturbative and nonperturbative approaches. *Surface Science*, 278(1):99 , 1992.
- [47] D. Teillet-Billy and J. Gauyacq. Resonant electron capture in atom metal collisions: H Al(111). *Surface Science*, 269-270:162 , 1992.
- [48] G. Cartry, et al. Alternative solutions to caesium in negative-ion sources: a study of negative-ion surface production on diamond in H₂/D₂ plasmas. *New Journal of Physics*, 19(2):025010, 2017.
- [49] J. N. M. van Wunnik and J. Los. Resonant charge transfer in atom-metal surface reactions. *Physica Scripta*, T6:27, 1983.
- [50] J. Los and J. Geerlings. Charge exchange in atom-surface collisions. *Physics Reports*, 190(3):133 , 1990.
- [51] H. B. Michaelson. The work function of the elements and its periodicity. *Journal of Applied Physics*, 48(11):4729, 1977.

- [52] D. Fehrs and R. Stickney. Contact potential measurements of the adsorption of alkali metals on Ta(110) and W(100) crystals. *Surface Science*, 24(1):309 , 1971.
- [53] A. G. Borisov, V. Sidis, and H. Winter. Diabatic energy level confluence: The mechanism of negative ion conversion of neutral atoms in grazing scattering from insulator surfaces. *Phys. Rev. Lett.*, 77:1893, 1996.
- [54] C. Auth, A. G. Borisov, and H. Winter. High fractions of negative ions in grazing scattering of fast oxygen atoms from a LiF(100) surface. *Phys. Rev. Lett.*, 75:2292, 1995.
- [55] J. K. Olthoff and K. E. Greenberg. The gaseous electronics conference rf reference cell—an introduction. *Journal of research of the National Institute of Standards and Technology*, 100(4):327, 1995. 29151745[pmid].
- [56] P. A. Miller, G. A. Hebner, K. E. Greenberg, P. D. Pochan, and B. P. Aragon. An inductively coupled plasma source for the gaseous electronics conference rf reference cell. *Journal of research of the National Institute of Standards and Technology*, 100(4):427, 1995. 29151752[pmid].
- [57] P. J. Hargis, et al. The gaseous electronics conference radio-frequency reference cell: A defined parallel-plate radio-frequency system for experimental and theoretical studies of plasma-processing discharges. *Review of Scientific Instruments*, 65(1):140, 1994.
- [58] J. K. Olthoff and K. E. Greenberg. The Gaseous Electronics Conference RF Reference Cell—An Introduction. *Journal of Research of the National Institute of Standards and Technology*, 100(4):327, 1995.
- [59] A. Schwabedissen, E. C. Benck, and J. R. Roberts. Langmuir probe measurements in an inductively coupled plasma source. *Phys. Rev. E*, 55:3450, 1997.
- [60] M. B. Hopkins. Langmuir probe measurements in the gaseous electronics conference rf reference cell. *Journal of research of the National Institute of Standards and Technology*, 100(4):415, 1995. 29151751[pmid].
- [61] V. Kaepelin, M. Carrère, and J.-M. Layet. Langmuir probe study in the post-discharge of a pulsed helicon discharge. *Plasma Sources Science and Technology*, 11(1):53, 2002.

- [62] R. L. Merlino. Understanding langmuir probe current-voltage characteristics. *American Journal of Physics*, 75(12):1078, 2007.
- [63] H. M. Mott-Smith and I. Langmuir. The theory of collectors in gaseous discharges. *Phys. Rev.*, 28:727, 1926.
- [64] J. E. Allen. Probe theory - the orbital motion approach. *Physica Scripta*, 45(5):497, 1992.
- [65] I. B. Bernstein and I. N. Rabinowitz. Theory of electrostatic probes in a low-density plasma. *The Physics of Fluids*, 2(2):112, 1959.
- [66] J. Laframboise. Theory of spherical and cylindrical langmuir probes in a collisionless, maxwellian plasma at rest. *U.T.I.A.S*, *(*):* , 1966.
- [67] M. Bacal. Photodetachment diagnostic techniques for measuring negative ion densities and temperatures in plasmas. *Review of Scientific Instruments*, 71(11):3981, 2000.
- [68] M. Nishiura, M. Sasao, and M. Bacal. H laser photodetachment at 1064, 532, and 355 nm in plasma. *Journal of Applied Physics*, 83(6):2944, 1998.
- [69] R. A. Stern, P. Devynck, M. Bacal, P. Berlemont, and F. Hillion. Nonresonant optical tagging and “monopolar” transport in negative-ion plasmas. *Phys. Rev. A*, 41:3307, 1990.
- [70] P. J. Eenshuistra, M. Gochitashvilli, R. Becker, A. W. Kleyn, and H. J. Hopman. Negative hydrogen ion densities and drift velocities in a multicusp ion source. *Journal of Applied Physics*, 67(1):85, 1990.
- [71] J. Santoso, R. Manoharan, S. O’Byrne, and C. S. Corr. Negative hydrogen ion production in a helicon plasma source. *Physics of Plasmas*, 22(9):093513, 2015.
- [72] C. M. Samuelli and C. S. Corr. Low-pressure hydrogen plasmas explored using a global model. *Plasma Sources Science and Technology*, 25(1):015014, 2015.
- [73] T. Gans, C. C. Lin, V. Schulz-von der Gathen, and H. F. Döbele. Phase-resolved emission spectroscopy of a hydrogen rf discharge for the determination of quenching coefficients. *Phys. Rev. A*, 67:012707, 2003.

- [74] T. Gans, V. Schulz-von der Gathen, and H. F. Döbele. Prospects of phase resolved optical emission spectroscopy as a powerful diagnostic tool for rf-discharges. *Contributions to Plasma Physics*, 44(5-6):523, 2004.
- [75] H.-M. Katsch, E. Quandt, and T. Schneider. The influence of metastables on the plasma-induced emission in a helium rf discharge. *Plasma Physics and Controlled Fusion*, 38(2):183, 1996.
- [76] V. Kaepelin, M. Carrère, and J. B. Faure. Different operational regimes in a helicon plasma source. *Review of Scientific Instruments*, 72(12):4377, 2001.
- [77] K. Achkasov. *Study of negative ion surface production in cesium-free H_2 and D_2 plasmas: application to neutral beam injectors for ITER and DEMO*. Ph.D. thesis, Université D'Aix-Marseille, PIIM, ED 352 Physique et Sciences de la Matière, 2015.
- [78] A. Ahmad, C. Pardanaud, M. Carrère, J.-M. Layet, A. Gicquel, P. Kumar, D. Eon, C. Jaoul, R. Engeln, and G. Cartry. Negative-ion production on carbon materials in hydrogen plasma: influence of the carbon hybridization state and the hydrogen content on H^- yield. *Journal of Physics D: Applied Physics*, 47(8):085201, 2014.
- [79] A. Ahmad, et al. Negative-ion surface production in hydrogen plasmas: modeling of negative-ion energy distribution functions and comparison with experiments. *Plasma Sources Science and Technology*, 22(2):025006, 2013.
- [80] J. L. Kinsey. Laser-induced fluorescence. *Annual Review of Physical Chemistry*, 28(1):349, 1977.
- [81] T. Mosbach, H.-M. Katsch, and H. F. Döbele. In situ diagnostics in plasmas of electronic-ground-state hydrogen molecules in high vibrational and rotational states by laser-induced fluorescence with vacuum-ultraviolet radiation. *Phys. Rev. Lett.*, 85:3420, 2000.
- [82] J. Booth, G. Hancock, N. Perry, and M. Toogood. Spatially and temporally resolved laser-induced fluorescence measurements of CF_2 and CF radicals in a CF_4 rf plasma. *Journal of Applied Physics*, 66(11):5251, 1989.

- [83] A. Kono, N. Koike, K. Okuda, and T. Goto. Laser-induced-fluorescence detection of SiH_2 radicals in a radio-frequency silane plasma. *Japanese journal of applied physics*, 32(4A):L543, 1993.
- [84] R. Ono and T. Oda. Measurement of hydroxyl radicals in an atmospheric pressure discharge plasma by using laser-induced fluorescence. *IEEE Transactions on industry applications*, 36(1):82, 2000.
- [85] J. Amorim, G. Baravian, and J. Jolly. Laser-induced resonance fluorescence as a diagnostic technique in non-thermal equilibrium plasmas. *Journal of Physics D: Applied Physics*, 33(9):R51, 2000.
- [86] F. Fresnet, G. Baravian, S. Pasquiers, C. Postel, V. Puech, A. Rousseau, and M. Rozoy. Time-resolved laser-induced fluorescence study of no removal plasma technology in N_2/NO mixtures. *Journal of Physics D: Applied Physics*, 33(11):1315, 2000.
- [87] B. Eliasson and U. Kogelschatz. UV excimer radiation from dielectric-barrier discharges. *Applied Physics B*, 46(4):299, 1988.
- [88] K. Niemi, V. Schulz-Von Der Gathen, and H. Döbele. Absolute atomic oxygen density measurements by two-photon absorption laser-induced fluorescence spectroscopy in an rf-excited atmospheric pressure plasma jet. *Plasma Sources Science and Technology*, 14(2):375, 2005.
- [89] S. Reuter, J. Winter, A. Schmidt-Bleker, D. Schroeder, H. Lange, N. Knake, V. Schulz-Von Der Gathen, and K. Weltmann. Atomic oxygen in a cold argon plasma jet: TALIF spectroscopy in ambient air with modelling and measurements of ambient species diffusion. *Plasma Sources Science and Technology*, 21(2):024005, 2012.
- [90] J. Waskoenig, K. Niemi, N. Knake, L. Graham, S. Reuter, V. Schulz-Von Der Gathen, and T. Gans. Atomic oxygen formation in a radio-frequency driven micro-atmospheric pressure plasma jet. *Plasma Sources Science and Technology*, 19(4):045018, 2010.
- [91] B. Preppernau, K. Pearce, A. Tserepi, E. Wurzburg, and T. A. Miller. Angular momentum state mixing and quenching of $n=3$ atomic hydrogen fluorescence. *Chemical physics*, 196(1-2):371, 1995.

- [92] K. Niemi, V. Schulz-Von Der Gathen, and H. Döbele. Absolute calibration of atomic density measurements by laser-induced fluorescence spectroscopy with two-photon excitation. *Journal of Physics D: Applied Physics*, 34(15):2330, 2001.
- [93] J. B. Schmidt, S. Roy, W. D. Kulatilaka, I. Shkurenkov, I. V. Adamovich, W. R. Lempert, and J. R. Gord. Femtosecond, two-photon-absorption, laser-induced-fluorescence (fs-TALIF) imaging of atomic hydrogen and oxygen in non-equilibrium plasmas. *Journal of Physics D: Applied Physics*, 50(1):015204, 2016.
- [94] C. Lukas, M. Spaan, V. Schulz-von der Gathen, M. Thomson, R. Wegst, H. Döbele, and M. Neiger. Dielectric barrier discharges with steep voltage rise: mapping of atomic nitrogen in single filaments measured by laser-induced fluorescence spectroscopy. *Plasma Sources Science and Technology*, 10(3):445, 2001.
- [95] E. Wagenaars, T. Gans, D. O'connell, and K. Niemi. Two-photon absorption laser-induced fluorescence measurements of atomic nitrogen in a radio-frequency atmospheric-pressure plasma jet. *Plasma Sources Science and Technology*, 21(4):042002, 2012.
- [96] A. Goehlich, T. Kawetzki, and H. Döbele. On absolute calibration with xenon of laser diagnostic methods based on two-photon absorption. *The Journal of chemical physics*, 108(22):9362, 1998.
- [97] A. D. Tserepi, J. R. Dunlop, B. L. Preppernau, and T. A. Miller. Absolute H-atom concentration profiles in continuous and pulsed rf discharges. *Journal of applied physics*, 72(7):2638, 1992.
- [98] K. Niemi, T. Mosbach, and H. Döbele. Is the flow tube reactor with NO₂ titration a reliable absolute source for atomic hydrogen? *Chemical physics letters*, 367(5-6):549, 2003.
- [99] B. V. Tata and B. Raj. Confocal laser scanning microscopy: Applications in material science and technology. *Bulletin of Materials Science*, 21(4):263, 1998.
- [100] E. Gu, H. W. Choi, C. Liu, C. Griffin, J. M. Girkin, I. M. Watson, M. D. Dawson, G. McConnell, and A. M. Gurney. Reflection/transmission confocal microscopy

- characterization of single-crystal diamond microlens arrays. *Applied Physics Letters*, 84(15):2754, 2004.
- [101] S. J. Doyle, A. R. Gibson, J. Flatt, T. S. Ho, R. W. Boswell, C. Charles, P. Tian, M. J. Kushner, and J. Dedrick. Spatio-temporal plasma heating mechanisms in a radio frequency electrothermal microthruster. *Plasma Sources Science and Technology*, 27(8):085011, 2018.
- [102] R. G. Wilson. Vacuum thermionic work functions of polycrystalline Be, Ti, Cr, Fe, Ni, Cu, Pt, and type 304 stainless steel. *Journal of Applied Physics*, 37(6):2261, 1966.
- [103] S. Markelj and I. Čadež. Production of vibrationally excited hydrogen molecules by atom recombination on Cu and W materials. *The Journal of Chemical Physics*, 134(12):124707, 2011.
- [104] P. W. Tamm and L. D. Schmidt. Binding states of hydrogen on tungsten. *The Journal of Chemical Physics*, 54(11):4775, 1971.
- [105] P. Devynck, J. Auvray, M. Bacal, P. Berlemont, J. Bruneteau, R. Leroy, and R. A. Stern. Photodetachment technique for measuring H velocities in a hydrogen plasma. *Review of Scientific Instruments*, 60(9):2873, 1989.
- [106] T. Mosbach, H.-M. Katsch, and H. F. Döbele. Temporal behaviour of the H^- density in a pulsed multipole discharge investigated by the photodetachment technique. *Plasma Sources Science and Technology*, 7(1):75, 1998.
- [107] M. Péalat, J. E. Taran, M. Bacal, and F. Hillion. Rovibrational molecular populations, atoms, and negative ions in H_2 and D_2 magnetic multicusp discharges. *The Journal of Chemical Physics*, 82(11):4943, 1985.
- [108] K. N. Leung, K. W. Ehlers, and R. V. Pyle. Effect of wall material on H production in a multicusp source. *Applied Physics Letters*, 47(3):227, 1985.
- [109] O. Fukumasa and S. Saeki. Effect of wall material on negative ion production in a hydrogen plasma. *Journal of Physics D: Applied Physics*, 20(2):237, 1987.
- [110] M. Bacal, A. A. Ivanov, M. Glass-Maujean, Y. Matsumoto, M. Nishiura, M. Sasao, and M. Wada. Contribution of wall material to the vibrational excitation and negative ion

- formation in hydrogen negative ion sources (invited). *Review of Scientific Instruments*, 75(5):1699, 2004.
- [111] M. Sode, T. Schwarz-Selinger, W. Jacob, and H. Kersten. Surface loss probability of atomic hydrogen for different electrode cover materials investigated in H₂-Ar low-pressure plasmas. *Journal of Applied Physics*, 116(1):013302, 2014.
- [112] H. Hosono. Exploring electro-active functionality of transparent oxide materials. *Japanese Journal of Applied Physics*, 52(9R):090001, 2013.
- [113] L. Schiesko, M. Carrère, J.-M. Layet, and G. Cartry. Negative ion surface production through sputtering in hydrogen plasma. *Applied Physics Letters*, 95(19):191502, 2009.
- [114] L. Schiesko, M. Carrère, G. Cartry, and J. M. Layet. H⁻ production on a graphite surface in a hydrogen plasma. *Plasma Sources Science and Technology*, 17(3):035023, 2008.
- [115] M. Gleeson and A. Kleyn. Effects of Cs-adsorption on the scattering of low energy hydrogen ions from HOPG. *Nuclear Instruments and Methods in Physics Research Section B: Beam Interactions with Materials and Atoms*, 157(1):48 , 1999.
- [116] J. Lienemann, D. Blauth, S. Wethekam, M. Busch, H. Winter, P. Wurz, S. Fuselier, and E. Hertzberg. Negative ion formation during scattering of fast ions from diamond-like carbon surfaces. *Nuclear Instruments and Methods in Physics Research Section B: Beam Interactions with Materials and Atoms*, 269(9):915 , 2011. Atomic Collisions in Solids.
- [117] P. Kumar, A. Ahmad, C. Pardanaud, M. Carrère, J. M. Layet, G. Cartry, F. Silva, A. Gicquel, and R. Engeln. Enhanced negative ion yields on diamond surfaces at elevated temperatures. *Journal of Physics D: Applied Physics*, 44(37):372002, 2011.
- [118] D. Kogut, R. Moussaoui, N. Ning, J. B. Faure, J. M. Layet, T. Farley, J. Achard, A. Gicquel, and G. Cartry. Impact of positive ion energy on carbon-surface production of negative ions in deuterium plasmas. *Journal of Physics D: Applied Physics*, 52(43):435201, 2019.
- [119] V. Baranauskas, B. B. Li, A. Peterlevitz, M. C. Tosin, and S. F. Durrant. Nitrogen-doped diamond films. *Journal of Applied Physics*, 85(10):7455, 1999.

- [120] L. Diederich, O. Küttel, P. Aebi, and L. Schlapbach. Electron emission and NEA from differently terminated, doped and oriented diamond surfaces. *Diamond and Related Materials*, 8(2):743 , 1999.
- [121] G. Cartry, L. Schiesko, C. Hopf, A. Ahmad, M. Carrère, J. M. Layet, P. Kumar, and R. Engeln. Production of negative ions on graphite surface in H₂/D₂ plasmas: Experiments and srim calculations. *Physics of Plasmas*, 19(6):063503, 2012.
- [122] H. de Esch and L. Svensson. Negative ion beam halo mitigation at the 1 MV testbed at IRFM. *Fusion Engineering and Design*, 86(4):363 , 2011.
- [123] U. Kurutz, R. Friedl, and U. Fantz. Investigations on Cs-free alternatives for negative ion formation in a low pressure hydrogen discharge at ion source relevant parameters. *Plasma Physics and Controlled Fusion*, 59(7):075008, 2017.
- [124] P. V. Sushko, A. L. Shluger, K. Hayashi, M. Hirano, and H. Hosono. Electron localization and a confined electron gas in nanoporous inorganic electrides. *Phys. Rev. Lett.*, 91:126401, 2003.
- [125] S. Matsuishi, Y. Toda, M. Miyakawa, K. Hayashi, T. Kamiya, M. Hirano, I. Tanaka, and H. Hosono. High-density electron anions in a nanoporous single crystal: [Ca₂₄Al₂₈O₆₄]⁴⁺(e⁻)₄. *Science*, 301(5633):626, 2003.
- [126] S. Mann. The chemistry of form. *Angewandte Chemie International Edition*, 39(19):3392, 2000.
- [127] L. Schiesko, M. Carrère, J.-M. Layet, and G. Cartry. A comparative study of H⁻ and D⁻ production on graphite surfaces in H₂ and D₂ plasmas. *Plasma Sources Science and Technology*, 19(4):045016, 2010.
- [128] A. Tallaire, A. Collins, D. Charles, J. Achard, R. Sussmann, A. Gicquel, M. Newton, A. Edmonds, and R. Cruddace. Characterisation of high-quality thick single-crystal diamond grown by CVD with a low nitrogen addition. *Diamond and Related Materials*, 15(10):1700 , 2006.
- [129] J. Birrell, J. E. Gerbi, O. Auciello, J. M. Gibson, D. M. Gruen, and J. A. Carlisle. Bonding structure in nitrogen doped ultrananocrystalline diamond. *Journal of Applied Physics*, 93(9):5606, 2003.

- [130] S. Bhattacharyya, et al. Synthesis and characterization of highly-conducting nitrogen-doped ultrananocrystalline diamond films. *Applied Physics Letters*, 79(10):1441, 2001.
- [131] P. Zapol, M. Sternberg, L. A. Curtiss, T. Frauenheim, and D. M. Gruen. Tight-binding molecular-dynamics simulation of impurities in ultrananocrystalline diamond grain boundaries. *Phys. Rev. B*, 65:045403, 2001.
- [132] S. Al-Riyami, S. Ohmagari, and T. Yoshitake. Nitrogen-doped ultrananocrystalline diamond/hydrogenated amorphous carbon composite films prepared by pulsed laser deposition. *Applied Physics Express*, 3(11):115102, 2010.
- [133] L. M. Pham, N. Bar-Gill, D. Le Sage, C. Belthangady, A. Stacey, M. Markham, D. J. Twitchen, M. D. Lukin, and R. L. Walsworth. Enhanced metrology using preferential orientation of nitrogen-vacancy centers in diamond. *Phys. Rev. B*, 86:121202, 2012.
- [134] M. Lesik, et al. Preferential orientation of nv defects in CVD diamond films grown on (113)-oriented substrates. *Diamond and Related Materials*, 56:47 , 2015.
- [135] M. Kitano, Y. Inoue, Y. Yamazaki, F. Hayashi, S. Kanbara, S. Matsuishi, T. Yokoyama, S.-W. Kim, M. Hara, and H. Hosono. Ammonia synthesis using a stable electride as an electron donor and reversible hydrogen store. *Nature Chemistry*, 4(11):934, 2012.
- [136] D. Rafalskyi, S. Dudin, and A. Aanesland. Magnetized retarding field energy analyzer measuring the particle flux and ion energy distribution of both positive and negative ions. *Review of Scientific Instruments*, 86(5):053302, 2015.
- [137] M. Abdel-Rahman, T. Gans, V. S. von der Gathen, and H. F. Döbele. Space and time resolved rotational state populations and gas temperatures in an inductively coupled hydrogen RF discharge. *Plasma Sources Science and Technology*, 14(1):51, 2005.
- [138] J.-S. Yoon, M.-Y. Song, J.-M. Han, S. Hwang, W.-S. Chang, B. Lee, and Y. Itikawa. Cross sections for electron collisions with hydrogen molecules. *Journal of Physical and Chemical Reference Data - J PHYS CHEM REF DATA*, 37:913, 2008.
- [139] S. Gomez, P. G. Steen, and W. G. Graham. Atomic oxygen surface loss coefficient measurements in a capacitive/inductive radio-frequency plasma. *Applied Physics Letters*, 81(1):19, 2002.

- [140] M. Abdel-Rahman, V. S. von der Gathen, T. Gans, K. Niemi, and H. F. Döbele. Determination of the degree of dissociation in an inductively coupled hydrogen plasma using optical emission spectroscopy and laser diagnostics. *Plasma Sources Science and Technology*, 15(4):620, 2006.
- [141] J.-K. Lee, H.-C. Lee, and C.-W. Chung. E–H mode transition in inductively coupled plasma using Ar, O₂, N₂, and mixture gas. *Current Applied Physics*, 11(5, Supplement):S149, 2011. The proceeding of the 10th Asia-Pacific Conference on Plasma Science and Technology (APCPST) and the 23rd Symposium on Plasma Science for Materials (SPSM) Korea from July 4–8, 2010.